Performance Enhancement of Cantilever Beam Piezoelectric Energy Harvesters

Peyman Hajheidari

A Thesis

In the Department

of

Mechanical, Industrial, and Aerospace Engineering

Presented in Partial Fulfillment of the Requirements

For the Degree of

Doctor of Philosophy (Mechanical Engineering) at

Concordia University

Montreal, Quebec, Canada

January 2020

CONCORDIA UNIVERSITY

SCHOOL OF GRADUATE STUDIES

This is to certify that the thesis prepared

By: Peyman Hajheidari

Entitled: Performance Enhancement of Cantilever Beam Piezoelectric Energy Harvesters

and submitted in partial fulfillment of the requirements for the degree of

Doctor Of Philosophy (Mechanical Engineering)

complies with the regulations of the University and meets the accepted standards with respect to originality and quality.

Signed by the final examining committee:

Dr. Anjali Awasthi	Chair
Dr. Dan Sorin Necsulescu	External Examiner
Dr. Khaled Galal	External to Program
Dr. Ramin Sedaghati	Examiner
Dr. Ayhan Ince	Examiner
Dr. Rama Bhat	Thesis Co-Supervisor
Dr. Ion Stiharu	Thesis Co-Supervisor

Approved by _____

Dr. Ivan Contreras, Graduate Program Director

March 13, 2020 _____

Dr. Amir Asif, Dean

Gina Cody School of Engineering and Computer Science

Abstract

Performance Enhancement of Cantilever Beam Piezoelectric Energy Harvesters

Peyman Hajheidari, Ph.D.

Concordia University, 2020

During the last decade, driven by the need, energy harvesting has drawn considerable attention due to the cost-effectiveness and simplicity of the structure. The most important feature or advantage of energy harvesters is their energy sources which are coming from the energy that would be wasted otherwise to the ambient surroundings. Among the three types of energy conversion methodologies, piezoelectric energy harvesters (PEHs) have been highlighted as a self-power source of energy for small wireless sensors with low required power input due to their simple converting structure.

While conventional piezoelectric materials possess ideal sensing properties, the microfabrication of these structures typically requires access to the sophisticated equipment and cleanroom facilities. Moreover, the fabrication process is time-consuming and expensive, researchers found it interesting to resort to micro-electromechanical system (MEMS) designs with inexpensive, simple and green-based materials and simple fabrication techniques such as paper.

Generally, the paper-based devices have offered significant benefits but their recorded performance is significantly below that of the ones of the commercial smart structures. Their development is still in the early stage of growth and they need to be properly designed to satisfy the general requirements of the commercial products. Geometry optimization, sizing and functionalizing are among the strategies which can be adopted to boost the performance of all types of piezoelectric energy harvesters including the paper-based piezoelectric energy harvesters (PPEH).

Therefore, the major contributions of this work are improvement of the performance of piezoelectric energy harvesters using the geometry modification, sizing analysis and functionalizing. In this work, the governing equations of piezoelectric cantilevers based on both Euler-Bernoulli and Timoshenko beam theories are developed and solved using one type of element with a great rate of convergence called superconvergent element (SCE). The theoretical analysis was validated against results published in the open literature and the results indicate that the proposed method yields higher accurate results. Further, the effect of non-uniformity on the electrical output and efficiency of Piezoelectric Energy Harvesters (PEH) are studied. Then, the influence of sizing and application of a series of piezoelectric cantilever energy harvesters on the performance of structure are studied. The effect of the shape of the piezoelectric elements is also

investigated below. Eventually, development of functionally graded piezoelectric materials (FGPMs) for non-uniform beams are presented to evaluate the effect of functionalizing.

Acknowledgment

I’m indebted to my co-supervisors Dr. Stiharu and Dr. Bhat for providing the opportunity to work under their supervision. All of their encouragement, support, suggestions, and comments have helped me to conduct this research. I would like to express my sincere gratitude to Dr. Stiharu from whom I always found an open door to discuss this research. Thank you Dr. Stiharu and Dr. Bhat for your extremely valuable suggestions in pursuing this research.

I would like to thank my family; I couldn’t have completed this research without them. My special thanks to my lovely wife, Maryam, for all her love and support. She is the force that helps me to make real all my dreams. Thanks to my parents especially my mother for all her prayers and moral support, she has always been an inspiration to me. I also would like to acknowledge my brothers for all their endless support.

List of Contents

List of Abbreviations

CFEM	Conventional finite element method
DOF	Degree-of–freedom
DPM	Distributed parameter model
EAPap	Electro-active paper
FD	Frequency difference
FEM	Finite element method
FGP	Functionally graded piezoelectric
FGPMs	Functionally graded piezoelectric materials
FGPEHs	Functionally graded piezoelectric energy harvesters
FRFs	Frequency response functions
MEMS	Micro-electromechanical system
MPGs	micro-power generators
PEHs	Piezoelectric energy harvesters
PPEH	Paper-based piezoelectric energy harvesters
RD	Relative difference
SCE	Superconvergent element
SDOF	Single-degree-of–freedom
SFEM	Spectral finite element method

List of Symbols

$a(t)$	Generalized coordinates vector
A_p	The electrode area
$\mathbf{A}$	The amplitude vector of generalized coordinates
$b(x)$	Width
b_0	Initial width
$\boldsymbol{C}$	Damping matrix
C_p	Capacitance of the one piezoelectric layer
$\overline{C}_p$	Effective (equivalent) capacitance of the piezoelectric layers
d_{31}	Piezoelectric strain coefficient
D_3	The electric displacement
E	Young's modulus
E_3	The electrical field along the thickness direction
f_n	Natural frequency of n^{th} mode
$\mathbf{F}$	Dynamic force vector
$g(t)$	The translation part of base motion
G	Shear modulus
h_p	Piezoelectric layers' thickness
h_0	Initial thickness of substrate layer
i	Imaginary number
$I(t)$	Current output
k_s	Shear correction factor
$\boldsymbol{K}$	Global stiffness matrix
L	Length of the beam
l_e	The length of one element
$\boldsymbol{M}$	Global mass matrix
n	Degree of the polynomial
$\boldsymbol{N_w}, \boldsymbol{N_\phi}$	Matrices of shape functions (1×4 for one element)
P_{in}	The input mechanical power

P_{out}	The output electrical power
$Q(t)$	Electric charge output
$\boldsymbol{R}$	Displacement vectors of the generic point S (3×1)
R_l	External load resistance
$\dot{\boldsymbol{R}}$	Velocity vector of the generic point S (3×1)
S	Generic point of the beam
S_r	Slenderness ratio
t	Time
T	Kinetic energy
u	Axial displacement
U	Potential energy
$v\,, w$	Transversal displacements
V	Volume
$v(t)$	The generated piezoelectric voltage
u_0, v_0, w_0	Displacements on the middle-plane
x, y, z	Positions of the point S in the relative coordinates system
X	The amplitude of the effective displacement, w_b
$\bar{Y}$	Location of the neutral axis
ε_{33}^{T}	The dielectric permittivity of piezoelectric layer at constant stress
ε_{33}^{S}	The dielectric permittivity of piezoelectric layer at constant strain
$\boldsymbol{\theta}$	The electromechanical coupling vector (3×1 for one element)
ϕ_x	The binding rotation of the cross section
$\gamma_{xz}\,, \gamma_p$	Transverse shear strains
ε	Axial strain
σ	Axial stress
τ	Transverse shear stress
ψ_j^e, φ_j^e	Shape functions of 4-DOF element, $j = 1, \dots, 4$
f_j	Shape functions of 8-DOF element, $j = 1, \dots, 4$
$W_i^e, \phi_i^e, W_{\mathrm{i}}^{\prime e},\ \phi_{\mathrm{i}}^{\prime e}(t)$	Generalized coordinate elements, $i = 1, 2$
ρ	Mass density

Γ	The efficiency of harvesting
ω	Excitation frequency
μ	Constant of mass proportionality
γ	Constant of stiffness proportionality
ζ	Damping ratio
α_b	Width taper ratio
α_h	Height taper ratio
δ	The symbol of virtual work
W_{IE}	The internal electrical energy
W_{nc}	The non-conservative mechanical force
$(\,)_p$	Piezoelectric layer properties
$(\,)_s$	Substrate layer properties
$(\acute{})$	Partial differentiation with respect to *x*
$(\dot{})$	Partial differentiation with respect to *t*

List of Figures

List of Tables

Chapter 1 Introduction

This chapter provides an introductory overview of piezoelectric energy harvesters. The existing conversion methodologies, vibrational energy harvesters which include different sources of vibration, cantilever energy harvesters and modeling of vibration conversion are studied. Then introduction of cantilever beam-based piezoelectric energy harvesters and their developments are overviewed. Moreover, a literature review regarding these areas is presented in order to define the particular objectives of the research based on the existing gaps. It is important to point out that the main contribution of this research is to improve the performance of cantilever-based piezoelectric actuators and extend their capability to paper based beams so as to provide the same level of energy as the conventional piezoelectric structures. Finally, the contents of the following six chapters are outlined in the last section of this chapter.

The results of this study have been presented in four journal articles which two of them have published in Journal of Intelligent Material Systems and Structures and other two articles are under the second review, one by the above mentioned journal and the other by the International Journal of Smart and Nano Materials.

1.1 Introduction of energy harvesters

For a long period of time, humans have used energy from natural sources (renewable energy) such as from windmill, watermill, and solar energy. Compared to the limited fossil fuel there is not any limitation to scavenge energy from natural sources. This type of energy has proved itself as a source of energy for many types of applications. The harvesting plants are divided into two categories called macro and micro energy technologies. For the former, the level of generated power is kW or MW while there is the power in the level mW or μW for the latter. As already mentioned earlier, the existence of large amounts of mechanical vibrations in the surrounding environments are among the most plentiful sources. In order to scavenge the energy from these undying sources it is necessary to conceive, fabricate and implement energy harvesters [1].

Energy harvesting, also known as power harvesting or power scavenging, is a technology wherein the energy is captured from one or more external energy sources to be stored and eventually used for later applications. The subject has drawn considerable attention during the last decade due to the cost-effectiveness and simplicity of the structures employed to carry this out and eventually, their portability. It is evident that the most important feature or advantage of energy harvesters is their energy sources which are coming from the wasted free energy to the ambient surroundings. In comparison to the other common kinds of energy providers such as fuels, these types of power scavenging devices deal with wasted energy and are more environmentally-friendly. This rich source of energy is available in most of the industrial plants, machinery, aerial and ground vehicles, and construction structures. Generally, there are three common sources of energy harvesting. They are based on the mechanical energy collected from sources such as vibration, mechanical stress and strain, the thermal energy coming from waste energy of furnaces, heaters, and friction sources and the light energy which is captured from sunlight or room light via photo sensors, photo diodes, or solar panels. The focus of this study is on the mechanical (or vibrational) energy harvesting. Invariably, the mechanical vibrations of the sources must be converted into electrical energy.

Nowadays, owing to the noticeable advances in wireless technology the energy harvested from the harvesters have been known as an alternative source of energy like batteries for a wide variety of devices. It should be noted that since the amount of energy harvested is very small the technology is applicable for low power small electronic devices such as wireless sensors and

portable and wearable electronics. In addition to the weight and high maintenance cost , the short life of batteries represents the most important obstacle compared to the long working life of power scavengers. Although there is an opportunity to replace or recharge the batteries, this type of solution is inefficient and sometimes not feasible due to the poor access to their locations. As a result, power harvesters have been taken into consideration by many researchers as a self-power source of portable or wireless devices in different areas [1].

1.2 Vibrational energy harvesters

Generally, there are two main modalities of energy harvesting which have been used to extract energy from a mechanical source called “inertial energy harvesting” and “kinematic energy harvesting”. The former relies on the resistance of a mass to the acceleration and the latter couples directly the energy harvester to the relative motion of different parts of a source such as energy harvested from the bending of a tire wall to monitor tire pressure or the flexing and extension of limbs to power mobile communication. In the inertial energy harvesters, excitations induce inertial force in the systems without directly deforming the active materials. Inertial energy harvesting systems are usually fixed on a vibration base such as human bodies, animals, machines, vehicles or buildings at a single point to harvest energy from the mechanical motions (vibrations) [2]. In contrast to the inertial state, the kinematic energy harvesting is not dependent on the inertia or resonance. In some cases, a tip mass (proof mass) is attached at the free end of the cantilever beam in order - not only to tune its fundamental natural frequency in accordance with the excitation frequency but also to improve the dynamic flexibility. By considering the proof mass there will be larger deflections of the tip and larger strains at the root which would result in power extraction enhancement [3]. It is worth mentioning that the tip of the cantilever is only under a small strain, so the main concentration needs to be taken near the root of the beam to have the most effective use of energy harvesters [4].

1.2.1 Sources of vibration

Prior to design and fabrication of the energy harvesters, it is essential to study various sources of vibrations. This is a critical issue since the natural frequency of resonators should be matching

the excitation frequency to be able to extract the maximum amount of energy. Generally, the vibrations measured from commonly occurring sources can be classified into two categories called "low-level" vibrations resulting from large industrial machinery and "low-level" vibrations resulting from air movement and human body motion such as walking, chest and heartbeat motion. Both low-level vibrations are focused mainly on very small scale power generation to power small electronic devices such as wireless sensor nodes or wearable devices. There are two important factors that characterize all sources which are the natural frequency and the acceleration magnitude of the fundamental vibration mode. They are the crucial characteristics which determine the potential estimation of the power generation [5]. Information about the potential of different low-level sources has been provided in Table 1.1.

Table 1.1 Acceleration magnitude and fundamental natural frequency of different low-level sources [5].

Vibration Source	Acceleration (m/s^2)	1^{St} Frequency
Car engine compartment	12	200
The base of 3-axis machine tool	10	70
Blender casing	6.4	121
Clothes dryer	3.5	121
Person nervously tapping heel	3	1
Car instrument panel	3	13
Door frame just after the door closes	3	125
Small microwave oven	2.5	121
HVAC vents in an office building	0.2-1.5	60
Windows next to a busy road	0.7	100
CD on notebook computer	0.6	75
Second story floor of a busy office	0.2	100

1.2.2 Energy conversion

In the literature, three basic mechanisms have been considered to convert mechanical vibrations to electrical energy, namely, electro-magnetic, electrostatic and piezoelectric. As has been already stated, the primary focus of this study is on the piezoelectric conversion mechanism. Piezoelectric materials are the type of smart materials exhibiting electromechanical coupling which possess the property to convert kinetic energy to electrical energy and vice versa [6]. They generate electric charge under the application of mechanical stress (direct piezoelectric effect) and creation of mechanical strain in response to an electric field (converse piezoelectric effect). Thermomechanical coupling is another feature of piezoelectric materials called the pyroelectric effect. Direct effect and converse effect could be used as an actuator and a sensor or energy

transducer, respectively. Due to their simple converting structure, piezoelectric energy harvesters have been highlighted as a self-power sources of energy for small wireless sensors with low required power input [7]. In order to fabricate the piezo MEMS, the piezoelectric materials prepared in thin-film must be integrated into MEMS using photolithography.

Polyvinylidene fluoride (PVDF) and Pb(Zr,Ti)O3 (PZT) are the most popular piezoelectric materials which have been extensively considered for many applications. PVDF is a type of piezoelectric polymer which has been most frequently used. It is a semi-crystalline polymer with a flexible structure which is easy to be deformed. The noticeable flexibility feature of PVDF makes it resilient to mechanical motions which allows it to be easily mounted on flexible structures undergoing bending motions. The small densities of piezoelectric polymers compared to PZT ceramics (less than ¼ of that) make them desirable for lightweight piezoelectric elements. The piezoelectric strain constant coefficient (d_{31}) of PVDF is in a lower range (12–23 pC/N) compared to PZT. Note that the value of piezoelectric constants strongly depend upon their fabrication and poling processes. The high amount of flexibility persuades researchers to investigate the application of PVDF for piezoelectric energy harvesting from wearable items, such as shoes and backpacks [8]. In this regard, Kendall [9] was the first to study PVDF as an energy harvesting material in the energy harvester shoes. They could harvest the mechanical energy from humans during walking.

The amount of generated power from piezo MEMS is strongly dependent on the different factors including the applied load, the frequency of vibration, the geometric features, and the boundary conditions [10]. This technology opened plenty of application possibilities in a wide variety of areas such as actuators, sensors, acoustic resonators, quartz crystal microbalance, surface acoustic wave (SAW)-based chemical and biochemical sensors, accelerometer, ultrasonic transducers. While they are beneficial, the microfabrication of these structures typically requires the access to the sophisticated equipment and cleanroom labs. Moreover, the fabrication process is time-consuming and expensive. The environment protection imposes researchers to look for the new portable, low-cost and eco-friendly candidates to generate energy. Therefore, they found it interesting to resort to MEMS designs with inexpensive, simple and green-based materials and simple fabrication techniques. Paper or cellulose is a kind of green-based material which has a strong potential to fulfill the needs as a potent alternative.

1.2.3 Cantilever energy harvesters

Micromachined cantilevers have been utilized as the mechanical energy harvester [11]. In other words, cantilever-based piezoelectric configuration represents a useful structure which can be exploited for direct energy harvesting from ambient vibrations to generate electrical energy for small devices such as autonomous wireless sensors [1]. A cantilever type vibration energy harvester is a simple structure which could generate maximum deflection (maximum strain) under vibration (deflection of the free end of the beam) which is why the cantilever beam has been used in most of the vibration energy harvesters. The ambient vibrational energy is saved from the resonant motion of the cantilever beams in different modes. It is obvious that the maximum tip deflection occurs in the first mode of vibration resulting in the highest amount of scavenged power [12]. In their structure, the piezoceramic layers are placed on the substrate layer as acting or sensing elements. They can be realized in different states including one layer of piezoceramic (unimorph), two layers of piezoceramic (bimorph) and even multilayers (multimorph) in which the kind of the exploited structure depends on the application under consideration. The energy harvester beam is connected to a vibrating host structure such as a shaker to excite the system with different excitation frequencies. By exciting the structure the dynamic strain induced in the piezoceramic layer(s) leads to an alternating electric charge across their electrodes [13, 14].

According to Table 1.1, the frequency range of household appliances and everyday objects is lower than 200 Hz. Hence, to harvest the maximum power from the piezoelectric cantilevers they should be designed to exhibit a resonant frequency less than this frequency. Material specifications and geometrical dimensions are two essential parameters that can help one to reach the goal. Since 200 Hz is rather a low natural frequency for a cantilever beam, small thickness and low modulus of elasticity play an important role to obtain lower natural frequencies. The soft piezoelectric polymer is a type of material that could be used for the fabrication of cantilever beams with a low resonance frequency and large strains because of low flexural rigidity. The advantage of polymeric resonators is that they can be fabricated inexpensively in a wide range of dimensions which is a desirable choice for low-cost vibrational energy harvesters. In this case, the use of cellulose would represent a great choice which has the potential to satisfy most of the above listed needs.

1.2.4 Modeling of cantilever energy harvesters

There are two different configurations called lumped-parameter and distributed-parameter modelling which could be taken into consideration in order to characterize the vibration of cantilevered energy harvesters. The former which is also known as single-degree-of-freedom modelling, has been the most well-known procedure followed to model the base excitation in cantilevered beam energy harvesters. To model the system based on this approach the point of interest (usually the free end of the beam) must be firstly specified. Then, a description of the dynamics of the point in terms of certain lumped parameters including the equivalent mass, stiffness, and the damping of the beam is required. Compared to the former, the latter is another model which has been used to model the vibration of energy harvesters providing more precise solutions [3]. These methodologies have been widely employed by different researchers for not only modeling but also studying optimization and generation of the maximum power output from the system. The application of each approach depends on the assumptions, limitations and the required accuracy. In this study, for better accuracy the lumped-parameter modelling with the assumptions of both Timoshenko and Euler-Bernoulli beam theories have been separately presented to extract the coupled equations. To discretize the equations finite element method with the application of the superconvergent element (SCE) having eight- degree-of-freedom (DOF) model is presented. The excitation of the harvester is assumed to be due to the base motion in the form of vertical translation at the fixed end of the cantilever beam. Although during the discretization it is not assumed that the base motion must be restricted to the harmonic in time, the resulting expressions for the coupled mechanical response and the electrical outputs are reduced for the case of harmonic excitation in time.

1.3 Cellulose (Paper)

The objective of this section is to introduce paper as a structural material with suitable properties for cantilever beam energy harvesters. Cellulose is one of the most abundant organic polymers with a noticeable structure and exclusive features. It is environmentally friendly and biocompatible and is extracted from green plants. Cellulose has been used to produce different products particularly paperboard and paper derivatives [15]. The use of cellulose in the fabrication

of piezoelectric materials is one of the main recent advances. Paper is known as a potent biological material. The particular feature comprising biocompatibility for the immobilization of proteins and antibodies have introduced cellulose as a material for biosensors, as well as actuators [16]. Recently, electro-active paper (EAPap), covering the electro-mechanical coupling effects, has been introduced as a smart material. The reported smart material has exclusive merits in comparison to the commercial smart structures. It is lightweight, cost-effective, biodegradable, biocompatible, foldable, environmentally friendly, disposable, easy to fabricate, portable and flexible. Furthermore, compared to other flexible materials cellulose has a much lower coefficient of thermal expansion leading to high thermal stability of the final devices [17, 18].

In comparison to PZT and PVDF, cellulose EAPap materials have low price, large displacement output because of low rigidity, low actuation voltage, low power consumption, biodegradable characteristics and also sensitive to humidity that would be practical to tune their natural frequencies based on our desired values. In other words, when paper imbibes water from different sources such as air humidity two natural phenomena occur. Firstly, as a result of an increased moisture content, the fibers of paper swell, leading to a strain called hygroexpansive strain. Secondly, while the content of moisture is growing up in the cellulose fiber structure, the bending stiffness of paper approaches a relaxation state resulting in changing the mechanical properties of the paper which could be used to tune the natural frequency of the EAPap energy harvester. Because of the above mentioned exclusive features of paper, it is an interesting to develop the application of paper in the fabrication of cantilevered piezoelectric energy harvesters with the tunability of the resonance frequency using the humidity modification. However, this feature of tuning properties based on the humidity modification can decrease the performance of system for the conditions with uncontrolled environmental humidity. Moreover, paper is a good candidate for functionalizing the structural properties, given the porous structure and the porous fibers [19].

Paper is the type of useful alternative which has proven its great potential in the production of electronic devices. Over the past two decades, there have been notable promising reports on electronic devices fabricated using different types of papers as the substrate layer [20]. These advances include transistors [21], transducers [22], energy storage devices [23], microfluidic devices [24, 25], strain sensors [16, 25, 26], gas sensors [27, 28], and actuators [29-33], energy harvesters [17, 22], lightweight speakers [34, 35] and so forth. Electro-active paper (EAPap) is

also attractive for artificial muscle applications in view of its piezoelectric effects causing extension and contraction (in-plane strains) during walking, running or other types of daily activities [16]. The activation mechanism of smart paper results from the ion migration effect of cellulose and piezoelectric effects of additives [36-38]. Although discovery of piezoelectricity of cellulose goes back to five decades [39], consideration of paper as a smart material goes back to the last decade. A number of researchers made efforts to align cellulose molecules with an electric field, magnetic field and also mechanically stretching but they could not clearly investigate the piezoelectric effect of naturally existing cellulose [40-43]. Alignment plays a key role in the fabrication process of EAPap since it can improve the mechanical and electrochemical properties [44].

According to the studies carried out, one of the main issues with cellulose EAPap materials is their small piezoelectric constants in comparison to the conventional piezoelectric materials. This significant difference has caused the degradation of their performance and efficiency. In order to be represented as a streamlined alternative some improvements are necessary. As a matter of fact, there are various strategies which can be adopted to improve the performance and efficiency of piezoelectric energy harvesters. Different design variables such as shape, size, material properties, electromechanical parameters and damping can be considered to achieve higher performance. Among these parameters, geometry modification and material functionalizing represent effective approaches which are the focus of this study. In order to look into this, it is firstly necessary to represent a valid mathematical modeling. Although the mathematical model is necessary to be simple it should be sophisticated enough to predict the dynamics of the physical system accurately in different applications [3]. The various modeling approaches considered by researchers are summarized in the following.

1.4 Development of existing mathematical modeling of PEH

So far, different models have been represented and developed to model PEH. In the first study, lumped-parameter model with a single mechanical degree of freedom was employed. The system was applied to predict the dynamic behavior of piezoelectric energy harvesters [10, 45]. Although this is a convenient modeling approach which can provide the initial insight into the problem, it has different significant drawbacks affecting the responses. Firstly, the achieved approximation is

limited to only one mode analysis. More importantly, owing to the considered simplifications the importance of noticeable aspects including the dynamic mode shapes and accurate strain distribution are overlooked [3].

As the second model, an improved approach using the Rayleigh-Ritz method was presented by Hagood et al. [46] which was used by other researchers to model the behavior of cantilevered piezoelectric energy harvesters [10, 47, 48]. They developed the model based on the Euler-Bernoulli beam theory. In comparison to the former approach with a single mechanical degree of freedom it is a more accurate model which gives a spatially discretized model of the distributed-parameter system. The discretized model provides an approximation of the distributed parameter system by reducing its infinite mechanical degrees of freedom to a finite dimension [49].

Although this can result in a more precise model, its accuracy strongly depends on the applied theory to model the beam. There are various theories regarding the description of beams, where the Euler-Bernoulli or classic beam theory is the oldest and most widely applied theory. Euler-Bernoulli theory is utilized commonly because it provides reasonable solutions for many engineering problems. However, the Euler-Bernoulli model tends to slightly overestimate the natural frequencies and it is not an appropriate approach for describing the behavior of short beams owing to the existence of shear deformation in the cross section of the beam. Thus, it is necessary to apply higher order theories such as the Timoshenko beam theory to reach reasonable approximation. The Timoshenko or first order beam theory is the extended form of the Euler-Bernoulli model wherein two additional effects including shearing force and rotary motion effects are considered. Since in this theory the shear stress distribution is assumed to be constant along the thickness, a Timoshenko shear coefficient is considered to reduce the error [50].

Another well-known approximate numerical model employs finite element method (FEM). The procedure in this method is based on variational principles wherein the differential equation is satisfied over an element or region. Fortunately, owing to availability of many standard software, it is possible to solve all types of problems by using FEM. In comparison to the Rayleigh Ritz method which uses global functions formulated over the entire domain of the structure the FEM uses the concept of dividing the structural domain into many small elements. As a result, Rayleigh Ritz method can sometimes be challenging because of the difficulty in obtaining appropriate admissible functions while FEM has narrow range of choices making it much easier. In other words, someone may not be able to guess the basic function or several piece-wise functions for

any given problem using the Rayleigh Ritz method while FEM enables users to come up with such functions called shape functions systematically. The accuracy of solutions in the FEM strictly depends on both the type of applied elements and the number of them, which would be proportional to the cost of data processing [51]. Owing to more simplicity and broader usage of the FEM, this mathematical model is employed here to discretize the equations and analyze the structure. For discretization purposes, various types of elements can be used changing the accuracy of results. In the present research, two different types of elements including the super-convergent element (four-degree-of-freedom) and the eight-degree-of-freedom element are developed and applied. For the former, the shape functions are obtained from the exact values of the nodal displacement for Timoshenko beam theory increasing the accuracy of the responses [52]. This kind of element is developed in this study for the first time to study the dynamic analysis of piezoelectric energy harvesters. Apart from the kind of element employed, the beam approach considered plays an important role as well as the accuracy of approximation is of great concern. In order to choose the most appropriate beam theory both Euler-Bernoulli and Timoshenko approaches are investigated in this study under different conditions including various beam sizes and non-uniform configurations.

1.5 Objectives and thesis outline

As it was already mentioned, although the paper-based devices have offered significant benefits and exclusive features, their performance is below the commercial smart structures. They are still in the early stage of development and need to be improved to satisfy the general requirements. In order to improve the performance of the system, it is first necessary to investigate the effects of different important parameters playing a key role in changing the operation of the system leading to enhancement of its efficiency. To study different aspects a theoretical/mathematical model should be available such that it could accurately model the system for different conditions. Therefore, representation of a satisfactory model and performance enhancement analysis of the piezoelectric structures using the shape optimization, sizing and changing the material configuration are the major contributions of this work. Through carrying out configuration modifications there is possibility to investigate the capability of shape alteration in the performance and efficiency of the conversion. This is the initial necessary step before paying

attention to the experimental part and the fabrication procedure of paper-based piezoelectric structures. Hence, the present work will focus on the fundamental aspects related to the effectiveness of cantilever type energy harvesters. Future work will focus on realization of paper-based cantilever shape energy harvesters.

As a matter of fact, there are different strategies which can be adopted to improve the performance and efficiency of piezoelectric energy harvesters. In fact, different design variables such as shape, size, material properties, electromechanical parameters and damping can be considered. Among these parameters, geometry modification and material functionalizing represent effective approaches which are the focus of this study. As a result of this, it is intended to design an optimized configuration with the maximum electrical output. Thus, the particular objectives of this research are:

1) To develop a general model based on Timoshenko and Euler-Bernoulli beam theories for unimorph and bimorph configurations to investigate the effects of electromechanical parameters on the performance of the PEH.
2) Modeling and studying the effects of non-uniformity on the performance and efficiency of PEH. In order to model the non-uniformity, the polynomial function with five different degrees changing from 1 to 5 is considered.
3) Studying the effects of sizing and application of a series of PEHs instead of one single piezoelectric energy harvester.
4) Investigation of non-uniform functionally graded piezoelectric energy harvesters (FGPEHs) and effects on non-uniformity and material characterization on the performance of structure.

The accomplishment of these particular objectives as well as the conclusions of the present research are described in six chapters organized and summarized as follows:

1.5.1. Chapter 1

This chapter provides firstly the introductory overview of the energy harvesting technology. Secondly, different types of energy harvesters particularly the vibrational energy harvester and their conversion to the electrical output using different types of methodologies are described. Then,

the cellulose and evolution of paper-based piezoelectric energy harvesters are taken into consideration. In the following, a literature review regarding the application and development of PPEHs is presented in order to discover the existing gaps and define the particular objectives of the research subsequently.

1.5.2 Chapter 2

In this chapter, the cantilever-based piezoelectric energy harvesters are modelled based on both Timoshenko and Euler-Bernoulli beam theories. The electromechanical coupling equations for bimorph configuration are derived. In order to discretize the equation, finite element method with the application of a presented high convergent element is used. This model can be used for both beam theories without performing extra calculations. To validate the accuracy of the model, the results are firstly validated by the experimental results in the literature. Additionally, the electrical output frequency response functions (FRFs) for various circuit conditions changing from the short-circuit ($R_l \to 0$) to the open-circuit ($R_l \to \infty$) conditions are determined. This enables us to evaluate the effects of load resistance on the resonance frequency, tip velocity and electrical outputs. Finally, the effects of slenderness ratio is investigated to figure out for which range of slenderness ratio it is necessary to switch between theories for higher accuracy.

1.5.3 Chapter 3

In this chapter, the non-uniform piezoelectric energy harvesters are modelled and the effects of tapering ratio and degree of non-uniformity on the performance and efficiency of the system are studied. The electromechanical coupling equations for three general states including unimorph, bimorph in series connection and bimorph in parallel connection are derived. Both Euler-Bernoulli and Timoshenko beam theories are chosen for the modeling. Also, it is assumed that the width and height of cantilever beam are changing based on polynomial function with different degrees changing from one to five. To solve the equations, finite element method with the application of two different elements including four-degree-of-freedom (DOF) model, and eight-DOF model are adopted.

1.5.4 Chapter 4

In this chapter, the effects of sizing is investigated to reach a system rendering higher output power. To meet the power enhancement, the effects of non-uniformity on the performance of one single rectangular cantilever beam are initially studied. It is proved that converging beams with larger degree of non-uniformity can provide more power output. As a result, the new system proposed consists of a series of smaller trapezoidal beams (converging beams) connected in series. It should be pointed out that the natural frequency and the structure's weight are kept constant in the designed system for more accurate comparison, although the system is delivering higher output power. Thus, performance enhancement is met with the same amount of piezoelectric material consumed.

1.5.5 Chapter 5

In this chapter, the behavior of non-uniform functionally graded piezoelectric energy harvester is investigated. The cantilever beams are modelled based on both beam theories. As the parametric study, the effects of tapering ratios, the degree of non-uniformity, load resistance, and the volume fraction parameter on the electrical outputs and the fundamental resonance frequency are studied. Volume fraction parameter is another important parameter with its influence on the output power and the natural frequency is examined.

1.5.6 Chapter 6

In this chapter, the conclusion of this research and the suggested future work are presented. The general conclusions are stated in the first section. The second section is devoted to the suggested future work.

Chapter 2 Analysis of bimorph piezoelectric beam energy harvesters using superconvergent element

Cantilever-based piezoelectric energy harvesters (PEHs) have been utilized as structures to extract mechanical energy from the ambient mechanical vibrations and transfer it into the electrical output. In this chapter, the performance of bimorph piezoelectric beam energy harvesters is investigated. The cantilever beam is modelled by using both Timoshenko and Euler-Bernoulli beam theories. The equations are discretized using the conventional finite element method (CFEM) and superconvergent element (SCE). Besides the high-rate of convergence, easy switching between the above beam theories is enabled by such element. The current model is presented for a Timoshenko beam model, but it could as well be used for a Euler–Bernoulli beam model. Additionally, voltage, current, and power frequency response functions (FRFs) for different ranges of load resistance varying from the short-circuit to the open-circuit conditions are determined to reach the maximum values. Effects of the slenderness ratio and the required beam model based on the geometric properties of the PEHs are discussed in the final part of this study. The results show that only for smaller values of the slenderness ratio (below 5) it is necessary to model the beam using the Timoshenko assumptions; otherwise both beam theories provide approximately the same responses.

2.1 Introduction

Among different types of existing energy harvesters, piezoelectric energy harvester is one of the most common structures which has been used to scavenge ambient vibrational energy from the surrounding environments. Piezoelectric materials are among the various non-conventional energy storage devices converting mechanical energy into electrical energy (direct piezoelectric effect) and mechanical strain in response to an electric field (converse piezoelectric effect) [53]. Amount of the collected energy using piezoelectric energy harvesters represents a large enough source for low power small electronic and MEMS devices such as wireless sensor and portable and wearable electronics [5]. Wireless sensors have become popular devices in different areas such as structural health monitoring and medical equipment [54]. In comparison to the conventional battery usage, self-powered wireless sensors are more advantageous because they do not have the common limited lifetime restriction. Although there is the opportunity to replace or recharge the batteries, this type of solution is expensive and sometimes not feasible because of the poor access to their locations [1]. Hence, piezoelectric energy harvesters represent a desirable alternative to meet the needs.

The cantilever beam is the most common structure utilized in mechanical energy harvesters. This is because of the maximum amount of electric output which could be extracted using the cantilever structure as a result of its maximum deflection at the free end. Piezoelectric cantilever energy harvesters work based on the resonance in order to scavenge the maximum power. There have been numerous studies reported about the application of cantilever structure as the vibrating configuration in the piezoelectric energy harvesting systems. These PEHs are ranging from micro to macro size depending on their applications [7, 10, 47, 55-59]. A comprehensive mathematical and experimental discussion has been presented for vibration-based PEHs by Erturk and Inman [3]. Typically, they considered two types of approaches including lumped-parameter model and distributed parameter model which can be adopted to mathematically model the system. The former formulates the harvester using a single-degree-of–freedom (SDOF) system. Subsequently, this provides a rough estimate of the maximum power extraction and it is limited to the single vibration mode. As a result, the latter has been proposed in which the structure is considered as a continuous system providing sufficient physical insight. For the latter, there are different well-known beam theories such as Euler-Bernoulli, Rayleigh, and Timoshenko, which could be

exploited to derive the eletromechanical coupling equations. Regardless of the exact solution, the discretized electromechanical equations could be derived using Rayleigh–Ritz method and finite element method (FEM) wherein improved predictions of modal frequencies are presented [3, 54].

Modelling the piezoelectric energy harvesters is an important step which needs to be comprehensively scrutinized given their complex fabrication process. Apart from that, by having a valid model one can evaluate the effects of different mechanical, geometric, and even electrical parameters on the performance of the system to achieve the optimized operation to yield maximum electrical output. Generally, a typical PEH consists of a cantilever beam as a substrate layer with one (unimorph), two (bimorph), or multi piezoceramic layers attached on its surfaces as the sensing or acting layers. The fixed end of the beam is attached to a base motion and there is a tip mass (proof mass) at the free end of the beam. The function of proof mass is to tune the fundamental natural frequency in accordance with the excitation frequency and improve the dynamic flexibility, as well. Up to now, several studies have been carried out to analyze the PEHs analytically and experimentally. Erturk and Inman [60] modelled a unimorph PEH as a continuous structure with Euler-Bernoulli beam assumptions and presented the exact analytical solution. They also compared their exact analytical solutions with the simple SDOF approach [61]. It was proved that the SDOF model may result in highly inaccurate solutions in comparison to the distributed parameter model (DPM). In addition, they explained that the inaccuracy of the obtained results using SDOF approach can be corrected by the addition of a large proof mass or by adding the correction factor [62]. In these studies, proportional damping was presented to model the effects of both the strain rate damping and the external air damping. Erturk and Inman [62] studied the performance of piezoelectric energy harvesters for the bimorph state based on Euler-Bernoulli assumptions. To achieve the electrical power output prediction, they analyzed the system for both parallel and series connections of piezoceramic layers on the top and bottom surfaces of the substrate layer. The validation was carried out through comparing the analytical results with the existing experimental data. They also investigated the effects of added tip mass which results in higher harvested electrical output. The experimental study was carried out by Fakhzan and Muthalif [63] to investigate the effect of tip mass on both voltage output and tip deflection. The experimental results were compared with the analytical ones using both Euler-Bernoulli and Timoshenko beam approaches. Dietl et al. [64] provided an exact formulation to calculate the amount of harvested voltage and tip deflection for a beam modeled based on Timoshenko beam

approach. By comparing the yield outputs with the results for the Euler-Bernoulli model, they figured out that considering both the rotary inertia and shear effects yield more accurate response. In fact, the simplified Euler-Bernoulli beam severely overpredicts the results and it can provide the same responses as by using Timoshenko beam theory when the length of the beam is quite significant (higher slenderness ratios). This result was obtained by Wang as well in [54]. Although the utilized distributed parameter model provides good predictions for both beam theories it cannot accurately predict the responses. The limitation is due to the considered shape functions which are derived for the uniform cantilever beam only under mechanical loading and not a coupled electromechanical system. From that point of view, it is necessary to come up with new methods to bridge the gap. Wang [54] presented spectral finite element method (SFEM) to predict the performance of bimorph piezoelectric energy harvesters using both beam theories and validated the numerical simulations using the available experimental data from the literature. Applying conventional finite element method is another solution. The most important problem associated with CFEM is their limited convergence rate. Application of superconvergent element represents one potential solution which has the required potential to tackle the above mentioned obstacle. Although both theories yield good convergence performance it is shown here that the percentage of relative errors of SCE is less than half of the one yielded by SFEM. Overall, SCE has three noticeable advantages mentioned as follows: (a) exact interpolation functions resulting from static equilibrium of the Timoshenko beam [52] (b) high rate of convergence rate so that only a small number of elements is required to reach the responses with high accuracy (c) it is easy to switch the beam model between Timoshenko and Euler-Bernoulli.

To the best of our knowledge, the application of SCE for the analysis of PEHs has not been reported in the open literature. As a result, the potential of this type of element is investigated here. In this study, a SCE for bimorph PEHs is developed and the results are validated by using the experimental and analytical solutions from the literature. The electromechanical coupling equations are derived under the assumptions of linear piezoelectric constitutive and linear stress/strain relations and applying Timoshenko beam theory which can be easily transferred to the Euler-Bernoulli case by changing the value of a constant to zero in the shape functions of the element (Appendix C). The main purpose of this investigation is to assess the SCE capacity for the application to predict the output of PEHs. It is assumed that for the bimorph case, the top and bottom piezoelectric layers have identical geometry, mechanical and electrical properties. The only

difference consists of their poling directions which are opposite for the series case although they should have the same directions for the parallel configuration. Firstly, the total kinetic and potential energies are derived. Then, corresponding external virtual work performed with base excitation and voltage drop on a load resistance are calculated. By applying Hamilton's principle and employing finite element method, the discretized governing equations for the coupled electromechanical system are defined. In the following, proportional damping is employed to account for both internal and external damping. After deriving the discretized equations for one element of the beam, the assembling procedure is carried out and subsequently the fixed boundary conditions are applied in MATLAB programming. By assuming harmonic excitation, voltage, current, and power response functions are determined for various ranges of load resistance changing from the short-circuit to open-circuit cases in order to extract the maximum values for each electrical output. Furthermore, the results of both beam theories are compared to identify which type of configuration provides more accurate predictions for different geometric conditions. In other words, the importance of the slenderness ratio of the beam on the applied beam theory is comprehensively investigated.

2.2 Theoretical modelling

A sketch of a cantilever bimorph piezoelectric beam which is subjected to flapping vibration is shown in Fig.2.1. As can be seen, h_p is the thickness of the piezoelectric layer, h_s is the thickness of the substrate layer, L is the length of the cantilever beam and b is the width. For the sake of simplicity, two identical piezoceramic layers are assumed to be installed along the opposite poling directions because the series connection is investigated here. Moreover, the following assumptions are considered during modelling of the system: (a) Linear piezoelectric constitutive and linear strain/strain relations, (b) same transverse displacements for the three layers across the thickness of the beam, (c) no slide between the piezoceramic layers and the substrate layer (perfect bonding), (d) the beam is perfectly clamped at one end and the deflections are small compared with the thickness of the cantilever beam.

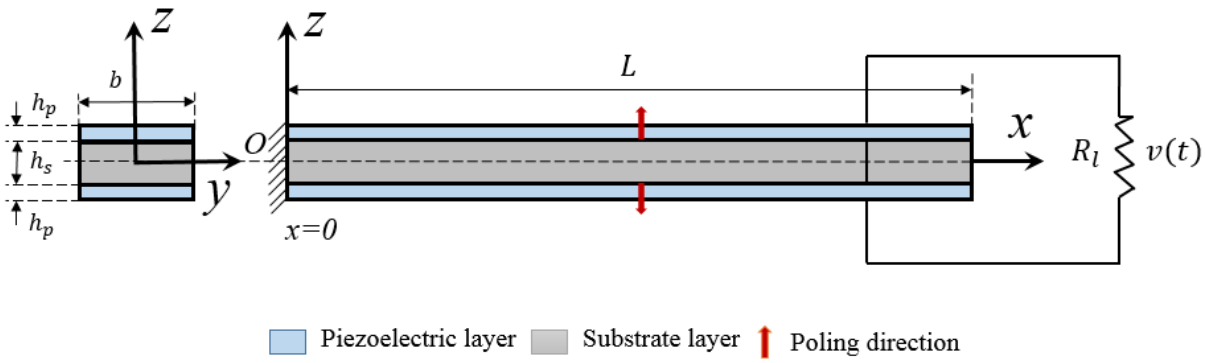

Figure 2.1 A cantilever bimorph piezoelectric energy harvester.

Considering all the aforementioned assumptions, for a cantilever beam fixed at point O (Fig. 2.1), the position vectors of a generic point *S* in flapping motion is represented by Eq. 2.1.

$$\boldsymbol{R} = R_x\hat{I} + R_z\hat{K} = u\hat{I} + w\hat{K} \tag{2.1}$$

where x is the position of the point S in the coordinate system XYZ and u and w are the displacements of a generic point of the deformed configuration measured with respect to the inertial frame. Consequently, the flexible displacement of a generic point of the cantilever beam based on the Timoshenko beam theory is defined by:

$$u(x,y,z,t) = u_0(x,t) + z\phi_x(x,t) \tag{2.2}$$

$$v(x,y,z,t) = v_0(x,y,t) = 0 \tag{2.3}$$

$$w(x,y,z,t) = w_0(x,t) + g(t) \tag{2.4}$$

where u_0, v_0, and w_0 are the displacements projected on the mid-plane, ϕ_x is the rotation of corresponding cross section at point x and time t relative to the moving base and $g(t)$ is the translation in the transverse direction resulting from the base motion.

Taking into account the definition of the Lagrange strain tensor and Eqs. 2.2 and 2.4, the non-zero components of the normal and shear strains in each layer are concluded.

$$\begin{cases} \epsilon_p = \dfrac{\partial u}{\partial x} = \acute{u}_0 + z\acute{\phi}_x & \dfrac{h_s}{2} \le z \le \dfrac{h_s}{2} + h_p \\ \epsilon_{xx} = \dfrac{\partial u}{\partial x} = \acute{u}_0 + z\acute{\phi}_x & -\dfrac{h_s}{2} \le z \le \dfrac{h_s}{2} \\ \epsilon_p = \dfrac{\partial u}{\partial x} = \acute{u}_0 + z\acute{\phi}_x & -\dfrac{h_s}{2} - h_p \le z \le -\dfrac{h_s}{2} \end{cases} \tag{2.5}$$

$$\begin{cases} \gamma_p = \dfrac{\partial u}{\partial z} + \dfrac{\partial w}{\partial x} = \phi_x + \acute{w}_0 & \dfrac{h_s}{2} \le z \le \dfrac{h_s}{2} + h_p \\ \gamma_{xz} = \dfrac{\partial u}{\partial z} + \dfrac{\partial w}{\partial x} = \phi_x + \acute{w}_0 & -\dfrac{h_s}{2} \le z \le \dfrac{h_s}{2} \\ \gamma_p = \dfrac{\partial u}{\partial z} + \dfrac{\partial w}{\partial x} = \phi_x + \acute{w}_0 & -\dfrac{h_s}{2} - h_p \le z \le -\dfrac{h_s}{2} \end{cases} \tag{2.6}$$

With respect to the linear piezoelectric constitutive equations [53] and considering the only d_{31} effect, the reduced piezoelectric constitutive equations of a thick beam based on the Timoshenko beam assumptions could be expressed using the following linear constitutive equations [3]:

$$\begin{Bmatrix} \epsilon_p \\ \gamma_p \\ D_3 \end{Bmatrix} = \begin{bmatrix} \dfrac{1}{E_p} & 0 & d_{31} \\ 0 & \dfrac{1}{K_s G_p} & 0 \\ d_{31} & 0 & \varepsilon_{33}^T \end{bmatrix} \begin{Bmatrix} \sigma_p \\ \tau_p \\ E_3 \end{Bmatrix} \tag{2.7}$$

where σ_p is the normal stress, τ_p is the shear stress, ϵ_p is the normal strain, γ_p is the shear strain, G_p is the shear modulus, E_p is the elastic modulus, D_3 is the electric displacement, d_{31} is the piezoelectric strain coefficient, ε_{33}^T is the dielectric permittivity of piezoelectric layer at constant stress, K_s is the shear correction factor which is 5/6 for a beam with a rectangular cross section and finally E_3 is the electrical field which can be written in terms of voltage v(t) across the electrodes as follows

$$E_3(t) = -\frac{v(t)}{h_p} \tag{2.8}$$

Based on the non-zero strains in Eqs. 2.5 and 2.6, structural relations for elastic isotropic substrate layer (Hooke's Law) are as follow

$$\tau_{xz} = K_s G_s \gamma_{xz} = K_s G_s (\phi_x + \acute{w}_0) \tag{2.9}$$

$$\sigma_{xx} = E_s \epsilon_{xx} = E_s \left(\acute{u}_0 + z\acute{\phi}_x\right) \tag{2.10}$$

where E_s and G_s are Young's modulus and shear modulus, respectively.

2.2.1 Kinetic and strain energy

Considering the stress and strains calculated, the strain and the kinetic energies of a piezoelectric energy harvester in the flapping mode can be defined as:

$$U = \frac{1}{2}\int [\sigma_{xx}\epsilon_{xx} + \tau_{xz}\gamma_{xz}]dV_s + \frac{1}{2}\int \left[\sigma_p \epsilon_p + \tau_p \gamma_p\right] dV_p \tag{2.11}$$

$$T = \frac{1}{2}\int \rho\left(\dot{\boldsymbol{R}}.\dot{\boldsymbol{R}}\right) dV \tag{2.12}$$

The subscripts s and p stand for substrate and piezo material, respectively, and the integrations are performed over the volume (V) of the respective material. In the above equations, dots and prime symbols identify derivatives with respect to time and space (i.e., x), respectively. By substituting the strains, stresses, and velocity into the previous equations the total energies are summarized as follows (more detailed calculations are provided in the Appendix B).

$$\begin{aligned} U = \frac{1}{2}\int_0^L & \left[\left(I_0^E \acute{u}_0{}^2 + I_2^E \acute{\phi}_x{}^2 + 2I_1^E \acute{u}_0 \acute{\phi}_x\right) + I_0^G\left(\acute{w}_0{}^2 + \phi_x{}^2 + 2\phi_x \acute{w}_0\right)\right] dx \\ & + \frac{1}{2}\int_0^L \left[\left(J_0^E \acute{u}_0{}^2 + J_2^E \acute{\phi}_x{}^2 + 2J_1^E \acute{u}_0 \acute{\phi}_x\right) + J_0^G\left(\acute{w}_0{}^2 + \phi_x{}^2 + 2\phi_x \acute{w}_0\right)\right. \\ & \left. + \frac{d_{31}}{h_p} J_0^E v(t)\acute{u}_0 + \frac{d_{31}}{h_p} J_1^E v(t)\acute{\phi}_x\right] dx \end{aligned} \tag{2.13}$$

$$T = \frac{1}{2}\int_0^L \left[I_0^\rho \dot{u}_0{}^2 + I_0^\rho \dot{w}_0{}^2 + 2I_0^\rho \dot{w}_0\dot{g} + I_0^\rho \dot{g}^2 + 2I_1^\rho \dot{u}_0\dot{\phi}_x + I_2^\rho \dot{\phi}_x{}^2\right] dx + \frac{1}{2}\int_0^L \left[J_0^\rho \dot{u}_0{}^2 + J_0^\rho \dot{w}_0{}^2 + 2J_0^\rho \dot{w}_0\dot{g} + J_0^\rho \dot{g}^2 + 2J_1^\rho \dot{u}_0\dot{\phi}_x + J_2^\rho \dot{\phi}_x{}^2\right] dx \tag{2.14}$$

where

$$I_i^E \triangleq \iint z^i E_s dydz\,,\quad I_0^G \triangleq \iint K_s z^i G_s dydz\,,\quad I_i^\rho \triangleq \iint z^i \rho_s dydz\,, i = 0{,}1{,}2 \tag{2.15}$$

$$J_i^E \triangleq \iint z^i E_p dydz\,,\quad J_0^G \triangleq \iint K_s z^i G_p dydz\,,\quad J_i^\rho \triangleq \iint z^i \rho_p dydz\,, i = 0{,}1{,}2 \tag{2.16}$$

The terms J_0^E and J_1^E are the piezoelectric coupling terms so that the former couples the voltage and the extension components and the latter couples the voltage and the curvature components. For the bimorph configuration (symmetric structure), the parameters $J_1^E, J_1^\rho, I_1^E\ I_1^\rho$ give zero values due to the existing symmetry in the configuration of the structure, and hence, there is no coupling between the axial and the transverse displacements (i.e., u_0 and w_0). This means that in a symmetric structure the axial displacement cannot be excited under the displacement of the base excitation.

The internal electrical energy in the piezoelectric layer is calculated according to Eq. 2.17.

$$\mathrm{W}_{IE} = \frac{1}{2}\int E_3 D_3\, dV_p = -\frac{1}{2}\frac{v(t)}{h_p}\int \left[E_p d_{31}\left(\acute{u}_0 + z\acute{\phi}_x\right) - \frac{v(t)}{h_p}\varepsilon_{33}^S\right] dV_p = -\frac{1}{2}\frac{v(t)}{h_p} d_{31}\int_0^L \left(J_0^E \acute{u}_0 + J_1^E \acute{\phi}_x\right) dx + \frac{1}{2} C_p v(t)^2 \tag{2.17}$$

where C_p is the internal capacitance of the piezoceramic given by:

$$C_p = \varepsilon_{33}^S \frac{A_p}{h_p} \tag{2.18}$$

where ε_{33}^{S} and A_p are the dielectric permittivity at constant strain and the electrode area, respectively.

The relationship between the permittivity at constant strain and constant stress is provided by the following [53]

$$\varepsilon_{33}^{S} = \varepsilon_{33}^{T} - {d_{31}}^{2} E_p \tag{2.19}$$

As is depicted in Fig. 2.1, the top and the bottom piezoelectric layers have the opposite poling directions. According to this configuration, the following equations represent the relationship between the characteristics of the piezoceramic layers including voltages, charges and piezoelectric strain coefficients in the serial connection.

$$v^T = v^B = \frac{v}{2} \quad and \quad d_{31}^T = -d_{31}^B \quad and \quad Q^T = Q^B = Q \tag{2.20}$$

where superscripts T and B denote the top and the bottom piezoceramic layers, respectively.

Damping is an important parameter which plays a key role in the performance of the dynamic systems. A combination of internal (strain-rate) and external (air) damping mechanisms exist for the undamped cantilever piezoelectric beam. They exhibit unavoidable effects on the frequencies of the system and subsequently the maximum power output. They should be accordingly considered carefully in order to have a more accurate model. To apply analytical modal analysis techniques, one of the ways to account for the effect of mechanical damping is usually restricted by the stiffness and mass proportional damping mechanisms. This type of model is referred to as Rayleigh damping which is especially employed in dynamic analysis of discrete systems [65]. Rayleigh damping is a damping matrix proportional to the resulting mass and stiffness matrices which is also employed here. At this point, without the existence of the mechanical dissipative effects, the extended Hamilton's principle is expanded as follows:

$$\int_{t_1}^{t_2} (\delta T - \delta U + \delta W_{IE} + \delta W_{nc}) dt = 0 \tag{2.21}$$

where δT, δU, δW_{IE} and δW_{nc} are the virtual works of the total kinetic energy, the strain energy, the internal electrical energy and the non-conservative mechanical force, respectively. The effect of base excitation is already considered in the total kinetic energy, so, the only remaining non-conservative virtual work is the one due to the electric charge output $Q(t)$. Therefore, for the non-conservative virtual work of the bimorph piezoelectric beam one can write that:

$$\delta W_{nc} = Q(t)\delta v(t) \tag{2.22}$$

2.2.2 Spatial discretization using finite element method

In this section the FEM is employed to discretize the coupled model. Various types of elements could be utilized for the discretization and in this chapter to increase the accuracy of results, superconvergent element comprising six-DOF is proposed (Fig. 2.2).

To employ the FEM, the cross-section of the beam structure is assumed uniform in the planar beam elements. If a beam has a varying cross-section, the beam should be divided into shorter beam elements with a more uniform cross-section.

2.2.3 Superconvergent element (SCE)

To solve the equations using FEM, it is necessary to consider one element along with its associated shape functions defining the nodal displacements. The accuracy of solutions strictly depends on both the type of applied elements and the number of them, which would be proportional to the cost of data processing. To increase the accuracy, one element with a high convergence rate named superconvergent element is applied here in this study. In the SCE, the Hermite cubic interpolation of w_0 and a related quadratic approximation of ϕ_x are considered. The approximate shape functions are derived using the solution of the equations of motion for the Timoshenko beam theory in the static case. Thus, the 4*4 system of equations obtained yield exact values of the nodal displacements. Because of the above-mentioned feature, the convergence rate of this element is much higher in comparison to the conventional finite element. In fact, for the conventional finite element, the admissible shape functions are only an approximate solution while the superconvergent element are the exact solution of the equations. Regarding the differences in matrices of conventional and superconvergent elements, they result in the same 4*4 matrices with

different shape functions (Appendix C). This type of element has two nodes and six degrees-of-freedom (DOF), including two DOF in the transverse direction, two DOF in the rotational direction and two in the axial direction (Fig. 2.2). In this model, the shape functions are derived by using static equilibrium. By solving the equations corresponding to the static balance, Lagrange linear shape functions, cubic shape functions and quadratic shape functions are derived for the axial, transverse, and the bending rotation, respectively. One of the noticeable benefits of this sort of element is its simple transferring method from the Timoshenko to Euler-Bernoulli beam. In other words, the element model includes a coefficient showing the effect of shear at the cross-section of the beam. By setting this coefficient to zero (i.e., infinite shear modulus or $G \to \infty$), one can have the results for the Euler-Bernoulli beam theory without performing extra calculations [52]. Therefore, using the derived shape functions, the three mentioned parameters in terms of the nodal displacements are represented in Eq. 2.23.

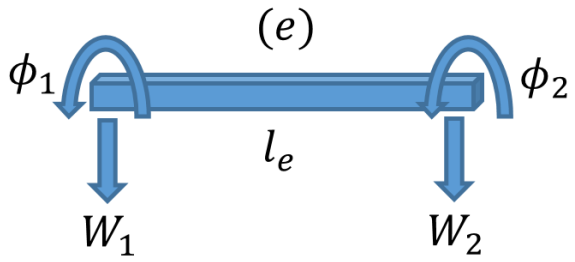

Figure 2.2 Two-node finite element with four DOF.

$$\begin{bmatrix} u_0(x,t) \\ w_0(x,t) \\ \phi_x(x,t) \end{bmatrix} = \begin{bmatrix} N_u(x) \\ N_w(x) \\ N_\phi(x) \end{bmatrix} a(t) \tag{2.23}$$

Also in the matrix form

$$\begin{bmatrix} u_0(x,t) \\ w_0(x,t) \\ \phi_x(x,t) \end{bmatrix} = \begin{bmatrix} \chi_1^e(x) & 0 & 0 & \chi_2^e(x) & 0 & 0 \\ 0 & \psi_1^e(x) & \psi_2^e(x) & 0 & \psi_3^e(x) & \psi_4^e(x) \\ 0 & \varphi_1^e(x) & \varphi_2^e(x) & 0 & \varphi_3^e(x) & \varphi_4^e(x) \end{bmatrix} \begin{bmatrix} U_1^e(t) \\ W_1^e(t) \\ \phi_1^e(t) \\ U_2^e(t) \\ W_2^e(t) \\ \phi_2^e(t) \end{bmatrix} \tag{2.24}$$

where $N_u(x)$, $N_w(x)$ and $N_\phi(x)$ are the shape functions (Appendix C), $a(t)$ is the unknown generalized coordinates. Substituting Eq. 2.24 into Eq. 2.21 and applying the integration by parts, the electromechanical coupling equations for a typical finite element in flapping mode is summarized in the following form:

$$\boldsymbol{M^e\ddot{a}(t) + C^e\dot{a}(t) + K^e a(t) - \theta^e} v(t) = \boldsymbol{f^e} \tag{2.25}$$

$$\boldsymbol{\theta^{eT} a(t)} + \overline{C_p} v(t) + Q = 0 \tag{2.26}$$

Taking the time derivative of Eq. 2.26 and using $I = \dot{Q} = v/R_l$ (the current generated by the cellulose electro-active paper) gives it as the new form Eq. 2.27. At this stage, Rayleigh damping (proportional damping) is added to the equations to account for the mechanical dissipative effects by preserving the normal-mode system as shown in Eq. 2.28.

$$\overline{C_p}\dot{v}(t) + \frac{v(t)}{R_l} + \boldsymbol{\theta^{eT}\dot{a}(t)} = 0 \tag{2.27}$$

$$\boldsymbol{C^e} = \mu \boldsymbol{M^e} + \gamma \boldsymbol{K^e} \tag{2.28}$$

where μ and γ are the constants of mass and stiffness proportionality. Term $\boldsymbol{M^e}$ is the mass matrix; $\boldsymbol{C^e}$ is the damping matrix; $\boldsymbol{K^e}$ is the elastic stiffness; $\boldsymbol{\theta^e}$ is the electromechanical coupling matrix and $\boldsymbol{f^e}$ is the vector of dynamical forces corresponding to one element of the piezoelectric cantilever beam, and $\overline{C_p}$ is the equivalent capacitance (presented in the Appendix E).

2.2.4 Solution of the electromechanical coupling equation

As the first step the type of base excitation input needs to be determined. By considering the input in the harmonic form $g(t) = Xe^{i\omega t}$ and assembling the elements of the beam, the components of the forcing vector become:

$$\boldsymbol{f}^e = \left[\omega^2 X \int_0^{l_e} \left(I_0^\rho + J_0^\rho\right) {N_w}^T dx\right] e^{i\omega t} \tag{2.29}$$

The steady-state response in generalized coordinates and the voltage output are defined as $\boldsymbol{a}(\boldsymbol{t}) = \boldsymbol{A}e^{i\omega t}$ and $v = Ve^{i\omega t}$ in which elements A and V are complex values. Finally, the assembled steady-state forms of electromechanical coupling equations are expressed as follows:

$$(-\boldsymbol{M}\omega^2 + i\omega\boldsymbol{C} + \boldsymbol{K})\boldsymbol{A} - \boldsymbol{\theta}V = \boldsymbol{F} \tag{2.30}$$

$$i\omega\boldsymbol{\theta^T A} + \left(i\omega\overline{C_p} + \frac{1}{R_l}\right)V = 0 \tag{2.31}$$

From Eq. 2.31

$$V = -i\omega\left(i\omega\overline{C_p} + \frac{1}{R_l}\right)^{-1}\boldsymbol{\theta^T A} \tag{2.32}$$

Substituting Eq. 2.32 into Eq. 2.30 the amplitude vector of generalized coordinates (A) is given as

$$\boldsymbol{A} = \left[-\boldsymbol{M}\omega^2 + i\omega\boldsymbol{C} + \boldsymbol{K} + i\omega\left(i\omega\overline{C_p} + \frac{1}{R_l}\right)^{-1}\boldsymbol{\theta\theta^T}\right]^{-1}\boldsymbol{F} \tag{2.33}$$

Also, substituting Eq. 2.33 into Eq. 2.31 yields the complex voltage as:

$$\begin{aligned} v(t) = -i\omega\left(i\omega\overline{C_p} + \frac{1}{R_l}\right)^{-1}\boldsymbol{\theta^T}\Bigg[&-\boldsymbol{M}\omega^2 + i\omega\boldsymbol{C} + \boldsymbol{K} \\ &+ i\omega\left(i\omega\overline{C_p} + \frac{1}{R_l}\right)^{-1}\boldsymbol{\theta\theta^T}\Bigg]^{-1}\boldsymbol{F}e^{i\omega t} \end{aligned} \tag{2.34}$$

Eventually, by having the vector of generalized coordinates $\boldsymbol{a}(\boldsymbol{t}) = \boldsymbol{A}e^{i\omega t}$ and substituting into Eq. 2.24 the axial displacement, the transverse displacement and the cross-section rotation are obtained as:

$$\begin{bmatrix} u_0(x,t) \\ w_0(x,t) \\ \phi_x(x,t) \end{bmatrix} = \begin{bmatrix} N_u(x) \\ N_w(x) \\ N_\phi(x) \end{bmatrix} \boldsymbol{A}e^{i\omega t} \tag{2.35}$$

The last point consists of the evaluation of the short-circuit and open-circuit natural frequencies of the PEH. In general, the short-circuit and open-circuit natural frequencies can be obtained by setting the mechanical damping $\boldsymbol{C}$ and applied force $\boldsymbol{F}$ to zero and considering the $R_l \to 0$ and $R_l \to \infty$ cases, respectively.

2.3. Numerical solutions and validation

In this section, a number of examples are studied to assess not only the predictions yielded by the model of a bimorph piezoelectric beam using the SCE, but also carry out the validation of the results by the experimental and analytical data existing in the literature to prove its potential and rate of convergence. The experimental and the analytical results presented by Erturk and Inman [3] have been validated by Wang using a spectral finite element method [54] and used in our work for validation of our results.

In the first example, the convergence of the superconvergent element is verified by considering a bimorph cantilever beam investigated by Erturk and Inman [3]. The properties of the investigated bimorph piezoelectric beam are presented in Table 2.1. This is a brass-reinforced bimorph manufactured by Piezo Systems Inc. The substrate layer is made of brass material and its top and bottom surfaces are covered with lead zirconate titanate (PZT-5H). It is worth noting that the piezoelectric layers are connected in series. Based on Table 2.2, the piezoelectric energy harvester has a slenderness ratio over 36.

Table 2.1 Properties of the bimorph piezoelectric cantilever beam.

Property	Piezoelectric layer	Substrate layer
Material	PZT-5H	Brass
Density ρ (kg/mm3)	7500	9000
Length (mm)	24.53	24.53
Thickness (mm)	0.265	0.14
Width (mm)	6.4	6.4
Young's modulus E (GPa)	60.6	105
Piezoelectric strain coefficient d31(pC/N)	-274	–
Dielectric permittivity at constant strain ε_{33}^{S} (nF/mm)	25.55	–
Shear modulus G (GPa)	23	40

In this example, only one SCE is used to extract the mechanical and electrical results. To include the effect of mechanical damping, proportional damping (modal damping) is considered with $\zeta = 0.00874$ as assumed by Erturk and Inman [3] for the first mode. Generally, for each and every mode of vibration the damping ratio must be firstly determined to be able to count the effect of dissipative damping. Half power bandwidth method has been used to estimate the modal damping ratio of the system for each natural mode from the frequency response function curve. For each resonance frequency, there is a peak in FRF amplitude so that 3 dB down from the peak there are two points corresponding to half power points. The distance between these points determines the amount of damping. In other words, the more the distance, the more the damping amount. Another common way to derive the damping ratio for the first natural mode of the systems is the logarithmic decrement method which can be applied here because in all of the calculations just the fundamental natural frequency with the maximum power output has been of interest [12].

To validate, the fundamental resonance frequency of the PEH based on the Timoshenko beam theory under the short-circuit ($R_l = 470\ \Omega$) and open-circuit ($R_l = 995\ k\Omega$) conditions is derived and compared with those in the literature, as summarized in Table 2.2. The exclusive convergence rate of this element is discernible from the results summarized in Table 2.2 in which using only one superconvergent element the difference between the experimental and theoretical values of 1st natural frequency is ignorable. The results prove that the relative errors between the predictions and the measured resonance frequency is less than 0.5% while this value was reported with

accuracy of 0.7-1.1% in another analytical study. Hence, the represented SCE has a very good rate of convergence in comparison to the spectral finite element method derived in the frequency domain [54]. It should be mentioned that in both the studies only one element is used to capture the dynamics of this electromechanically coupled system.

Table 2.2 Fundamental resonance frequency of piezoelectric energy harvester.

1st natural frequency	Experimental (Hz) [3]	SCE (Hz)	Error (%)	Ref [54] (Hz)	Error(%) [54]
Short circuit, ($R_l = 470\ \Omega$)	502.5	504.7	0.44	507.8	1.1
Open circuit, ($R_l = 995\ k\Omega$)	524.7	526.9	0.42	528.3	0.7

SCE: superconvergent element

As the second part of validation, the tip velocity and the voltage FRF results are compared with the experimental data under different resistance loading conditions varying from the short-circuit state to the open-circuit state. As it is cited in the literature [3], $R_l = 470\ \Omega$ and $R_l = 995\ k\Omega$ are considered as the short-circuit and open-circuit conditions, respectively. It should be pointed out that the tip velocity measurement taken by Erturk and Inman [3] is the velocity response of the point located approximately 1.5 mm away from the free end of the cantilever beam. Depicted graphs prove that the predicted outputs using the superconvergent element is in very good agreement with the experimental results although only one element was used in the SCE simulations in comparison to another analytical work [3] in which at least five mode shape functions were applied. The excellent correlation demonstrates the potential of the SCE to capture both mechanical and electrical responses. Figs. 2.3 to 2.6 show the experimental versus the solution achieved above for the beam tip velocity and voltage FRFs under different resistance loading conditions including $R_l = 470\ \Omega$ (short-circuit), $R_l = 1200\ \Omega$, $R_l = 44.9\ k\Omega$, and $R_l = 995\ k\Omega$ (open-circuit).

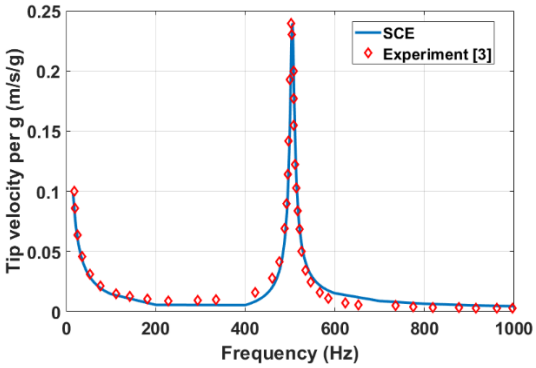

(a)

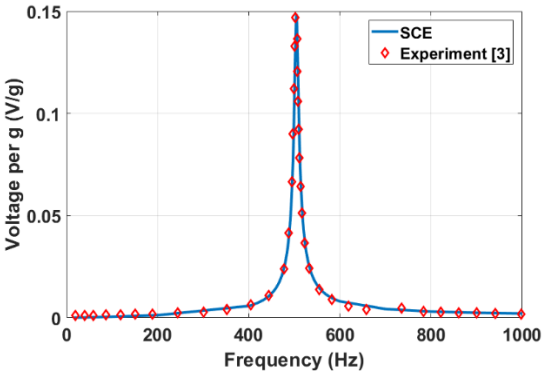

(b)

Figure 2.3 Tip velocity and voltage output FRF of the piezoelectric energy harvester, $R_l = 470\ \Omega$.

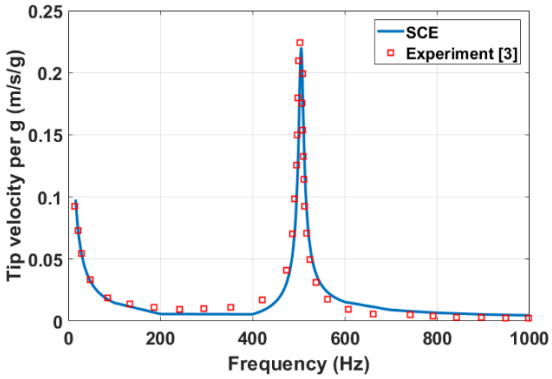

(a)

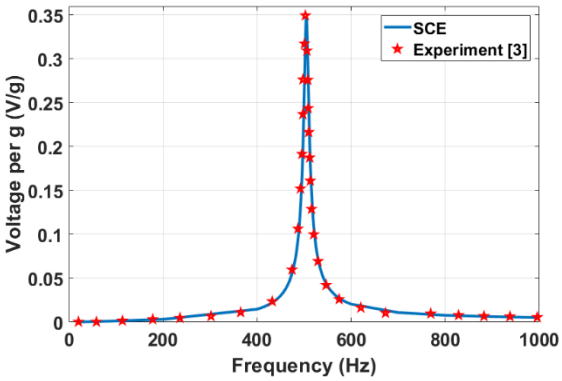

(b)

Figure 2.4 Tip velocity and voltage output FRF of the piezoelectric energy harvester, $R_l = 1200\ \Omega$.

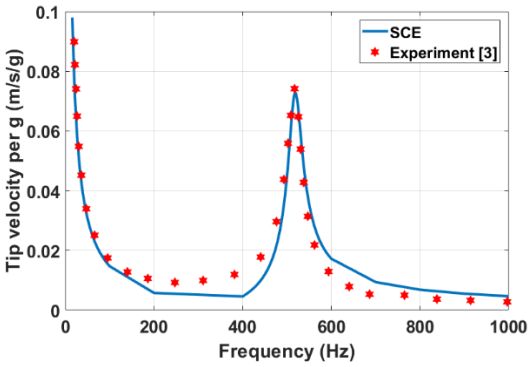

(a)

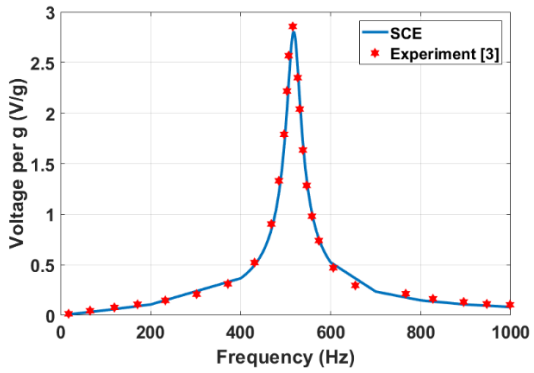

(b)

Figure 2.5 Tip velocity and voltage output FRF of the piezoelectric energy harvester, $R_l = 44.9\ k\Omega$.

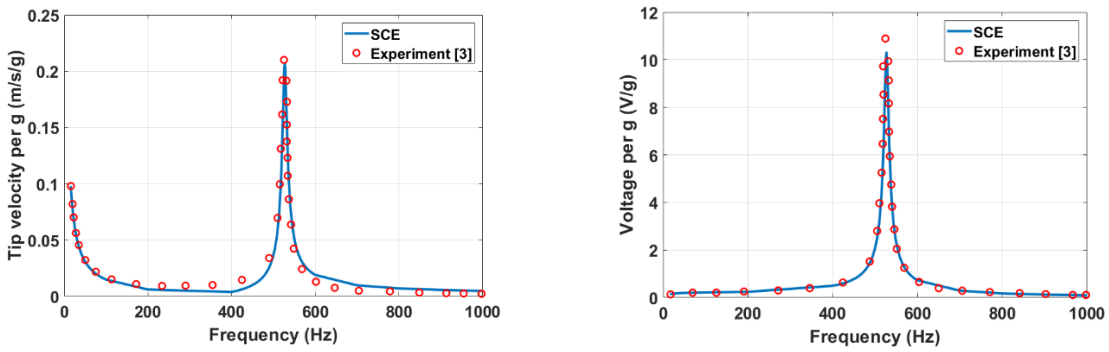

(a) (b)

Figure 2.6 Tip velocity and voltage output FRF of the piezoelectric energy harvester, $R_l = 995\ k\Omega$.

From the above graphs, it is obvious that both results are in a good agreement and the only significant difference (approximately 5%) between the predicted voltage and the experimental is corresponding to the open-circuit condition. In conclusion, the performance of the represented element is acceptable with the low percentage of error between the models and the experiments for the bimorph piezoelectric energy harvesters. Based on the obtained results by increasing the load resistance the frequency at which the peak of the graph (maximum values of both output voltage and tip velocity) is occurring is shifting little by little from 500 Hz to 600 Hz. Additionally, it can be seen that regardless of the value of the excitation frequency, increasing the load resistance could lead to increasing the output voltage. Therefore, the minimum and the maximum output voltages are achieved in the short-circuit and open-circuit cases, respectively. Last but not least, the open-circuit condition is providing the highest amount of output voltage while the maximum value of the tip velocity is associated with the short-circuit case although it yields a small difference with the open-circuit case (approximately 0.3 m/s/g).

In the second example similar to the first one, a bimorph piezoelectric cantilever is assumed with the same electromechanical properties for the top and the bottom piezoceramic layers as listed in Table 2.3. The total length and width of the PEH are 100 mm and 20 mm, respectively. The substrate is made of aluminum with Young's modulus of 70 GPa, shear modulus of 27 GPa and density of 2700 kg/m3. The thickness of the substrate is varying from 1.5 to 19.5 mm to cover a large range of values of the slenderness ratio. The predicted fundamental resonance frequency of the energy harvester using the proposed SCE is calculated analytically and provided in Table 2.4. It is noteworthy that Wang [54] examined the application of the both beam theories using the spectral finite element method.

In Table 2.4, the estimation of the first resonance frequency is obtained for both the short-circuit and open-circuit conditions. Beam with a number of different slenderness ratios based on both the Timoshenko and Euler-Bernoulli beam assumptions is taken in this example. By comparing the results, it can be concluded that the higher slenderness ratio has a decreasing effect on the fundamental natural frequency of the PEH.

As already expected in the literature the natural frequencies predicted using the Timoshenko assumptions give smaller values in comparison to the Euler-Bernoulli configuration because in the latter theory the shear modulus is considered infinite ($G_s \to \infty$) resulting in smaller stiffness values and subsequently smaller natural frequencies. Moreover, it can be observed that the resonance frequency in the open-circuit condition is slightly larger than of the short-circuit mode while the slenderness ratio is increasing. By comparting the results, the effect of the employed beam theory on the first resonance frequency is recognizable for the smaller slenderness ratio so that the maximum error is approximately 4% for $S_r = 5$. In other words, for thicker or shorter beams the Timoshenko approach should be employed while for longer or narrower beams application of the Timoshenko assumptions is not necessary and the acceptable outputs could be expected by use of the Euler-Bernoulli approach.

Table 2.3 Properties of bimorph piezoelectric cantilever beam.

Property	Piezoelectric layer	Substrate layer
Material	PZT-5H	Aluminum
Density ρ (kg/m3)	7500	2700
Length (mm)	100	100
Thickness (mm)	0.25	Variable
Width (mm)	20	20
Young's modulus E (GPa)	60.6	70
Piezoelectric strain coefficient d31(pC/N)	-274	–
Dielectric permittivity at constant strain ε_{33}^{S} (nF/m)	25.55	–
Shear modulus G (GPa)	23	27

Table 2.4 The fundamental resonance frequency of harvester in different conditions using both beam theories

$S_r = {}^{L}/_{h}$	f_1 (Hz)	Short-circuit ($R_l = 10^{-3}\ \Omega$)		Open-circuit ($R_l = 10\ M\Omega$)	
		Timoshenko	Euler-Bernoulli	Timoshenko	Euler-Bernoulli
5	Present	1574.4	1595.6	1579.8	1601.2
	Ref [54]	1552	1602	1557	1608
	Error (%)	1.4	0.4	1.5	0.4
10	Present	779.9	782.6	785.2	787.9
	Ref [54]	774	781	780	786
	Error (%)	0.8	0.2	0.7	0.2
20	Present	373.2	373.5	378.1	378.4
	Ref [54]	371	372	376	377
	Error (%)	0.6	0.4	0.6	0.4
50	Present	132	132	135.8	135.8
	Ref [54]	131.5	131.5	135	135
	Error (%)	0.4	0.4	0.6	0.6

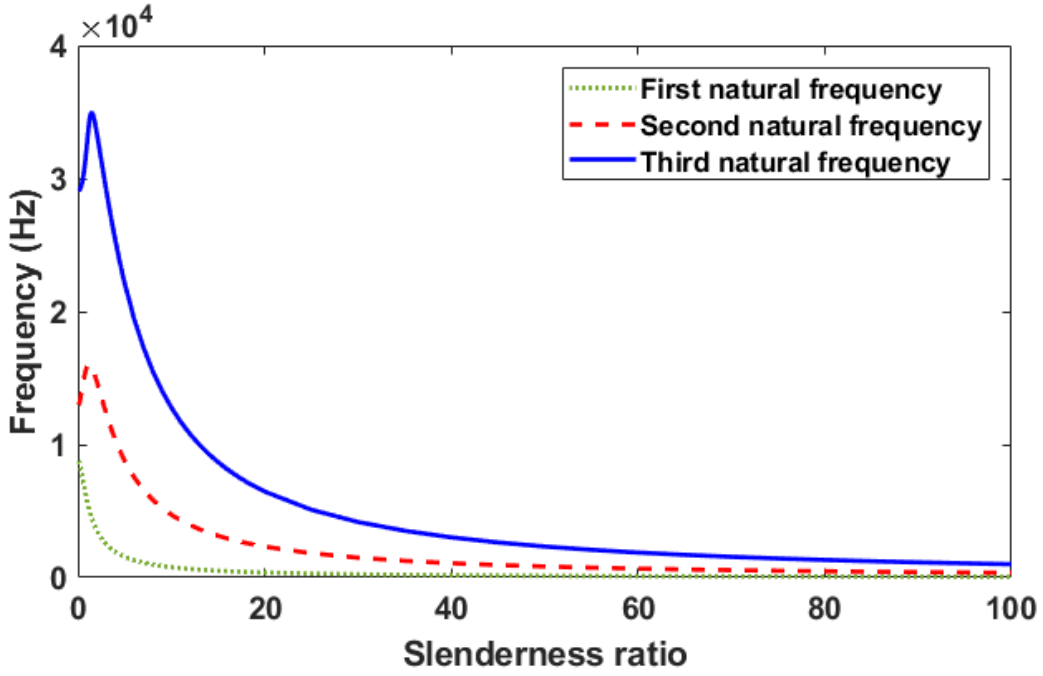

Figure 2.7 The effects of the slenderness ratio on the first three resonance frequencies in the open-circuit condition, $R_l = 10\ M\Omega$.

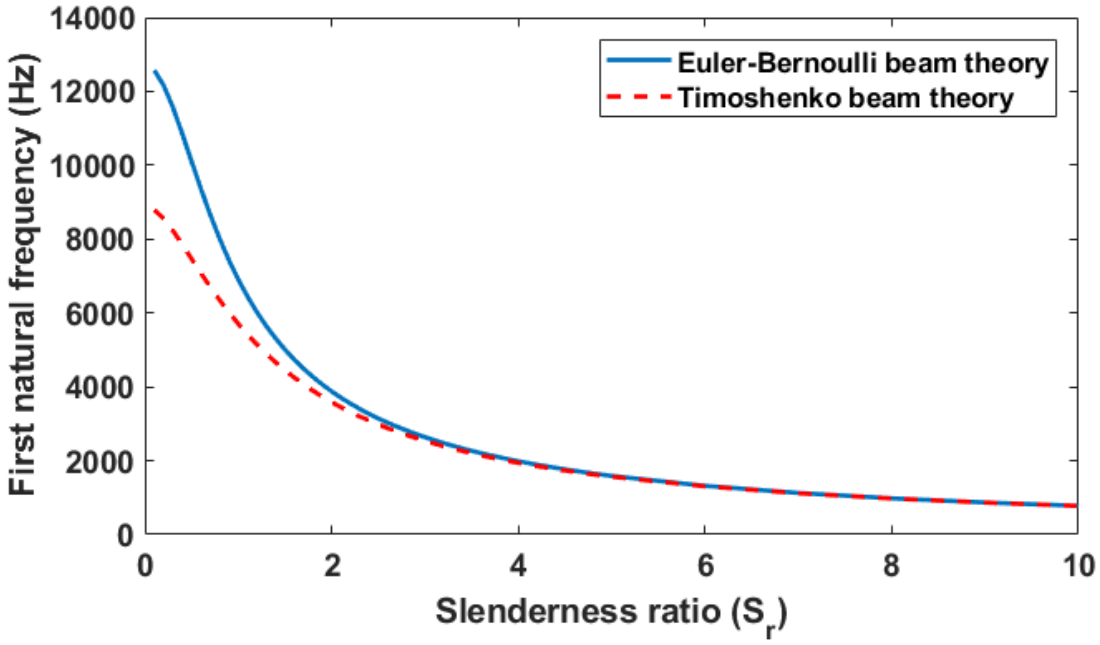

Figure 2.8 The effects of the slenderness ratio on the difference between the calculated 1st natural frequency using both beam theories in the short-circuit condition, $R_l = 1e-3\ \Omega$.

Fig. 2.7 shows the effects of the slenderness ratio on the first three resonance frequencies of the energy harvester in the open-circuit condition. Three superconvergent elements are applied during the assembly for the prediction of resonance frequencies. Obviously, as the slenderness ratio is increasing the natural frequencies are decreasing. Meanwhile, the effects of the employed beam theory on the fundamental natural frequency of the beam can be seen in Fig. 2.8. It could be concluded that the increasing slenderness ratio has a decreasing effect on the difference between the obtained results using both beam theories. Based on Fig. 2.8, the variation between the predicted frequencies is negligible for slenderness ratio $S_r \geq 5$. Regarding the capacity of the piezoelectric energy harvesters, investigation of the resulting electromechanical FRFs including the voltage output, the current output, and the power output are important aspects. Since the value of the load resistance R_l has an important role in the determination of the output of the harvester, the FRFs for five different values of the load resistance ranging from $10^6\ \Omega$ (close to the short-circuit case) to $10^2\ \Omega$ (close to the open-circuit case) are plotted in Figs. 2.9-2.11. Based on the derived formula for the output voltage, it has a direct relationship with the load resistance R_l while it is inverted for the current output because it is determined by dividing the voltage FRF by the load resistance. Hence, the current output is decreasing as the load resistance R_l is increased.

Finally, since power output is the product of the two FRFs which exhibit the opposite behaviors, the behavior of the power output FRF could not be easily predicted. For every excitation frequency the maximum voltage and current outputs are obtained when the system is within the open-circuit and close-circuit cases, respectively. With regard to the power output, it is obvious from Fig. 2.11 that the power output FRF does not exhibit a monotonic behavior with increasing (or decreasing) the load resistance similar to the other two FRFs. In summary, Fig. 2.11 represents that among the five considered load resistances $R_l = 10^4\ \Omega$ could provide the highest amount of power extraction for the designed energy harvester. It should be pointed out that in order to extract the values, three superconvergent elements are used with the Timoshenko beam assumptions and the geometric property $S_r = 50$. Finally, in Fig. 2.12 a 3D image of the output power for different values of the excitation frequency and load resistance is shown. As can be seen, the maximum state is occurring for $R_l = 10^3 - 10^4\ \Omega$ as was depicted in Fig. 2.11, as well. The excitation frequency associated with the highest resistance value is $131.83\ Hz$ which results in the peak of the power output, 0.0159. Hence, the optimized condition is more near to the short-circuit condition although one cannot surely reach to the highest voltage and current outputs in this case. In conclusion, based on our objective function the optimized values of the variables need to be changed. In other words, there is no possibility to optimize the three mentioned objective functions simultaneously.

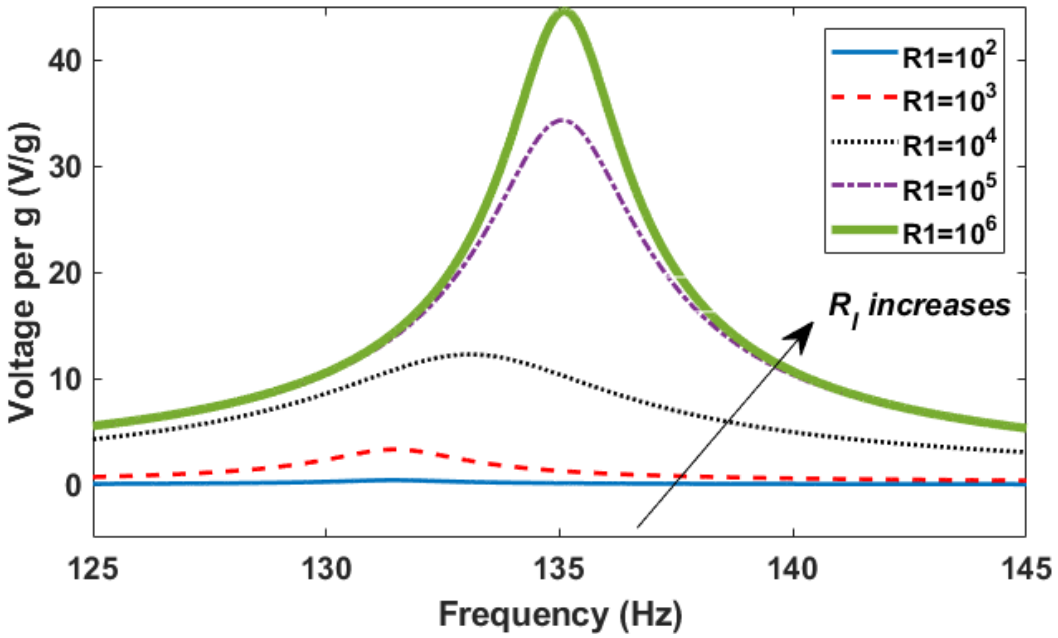

Figure 2.9 Voltage FRF for five different values of the load resistance.

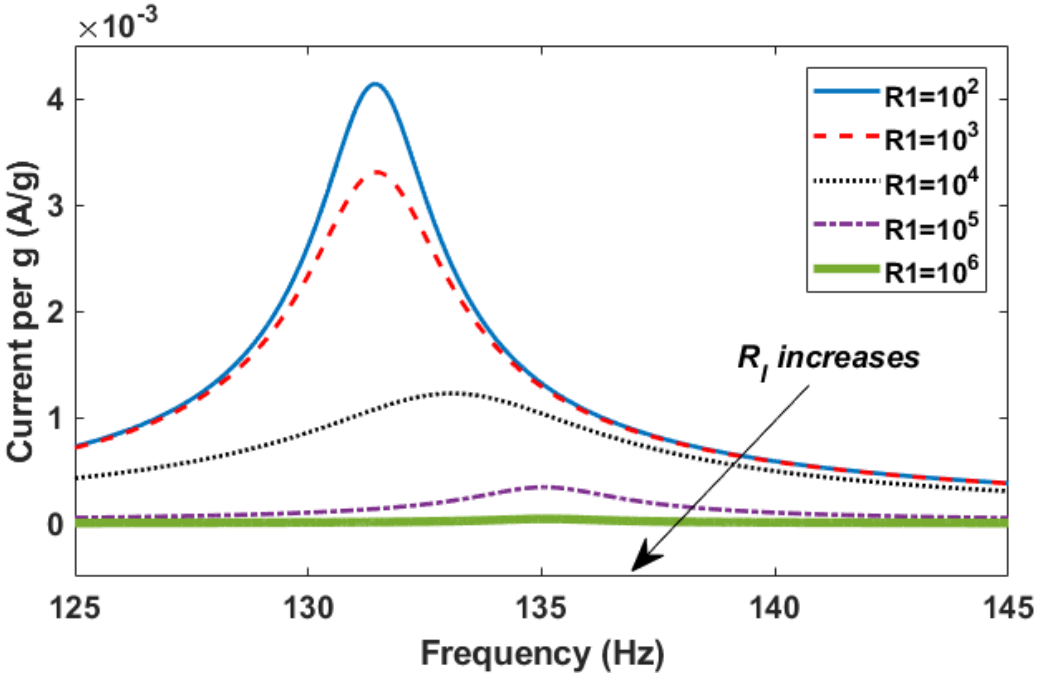

Figure 2.10 Current FRF for five different values of the load resistance.

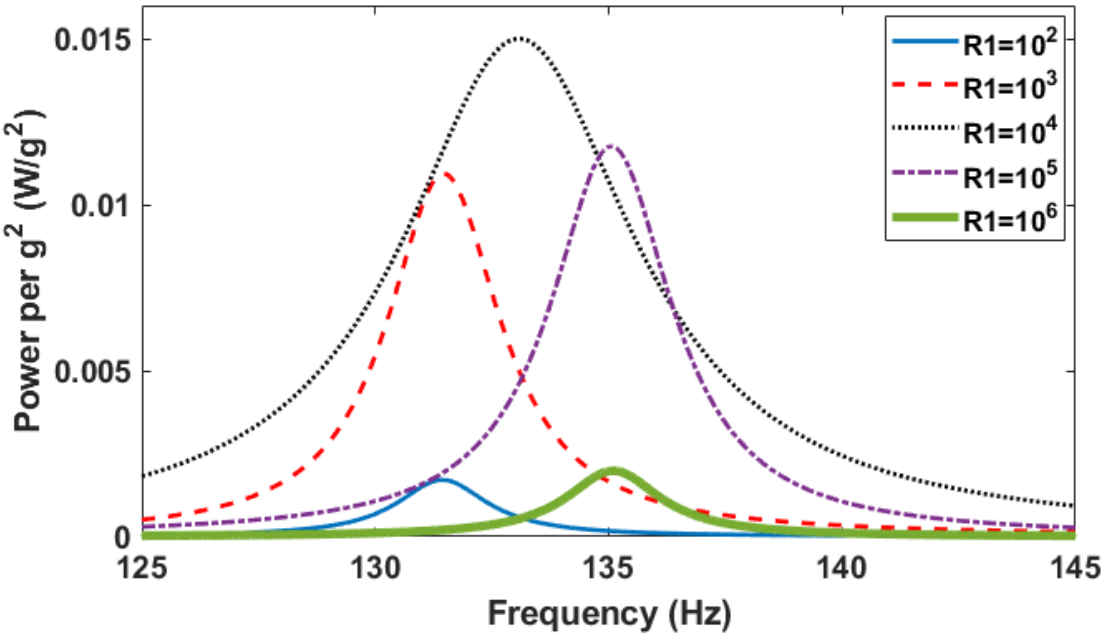

Figure 2.11 Power FRF for five different values of the load resistance.

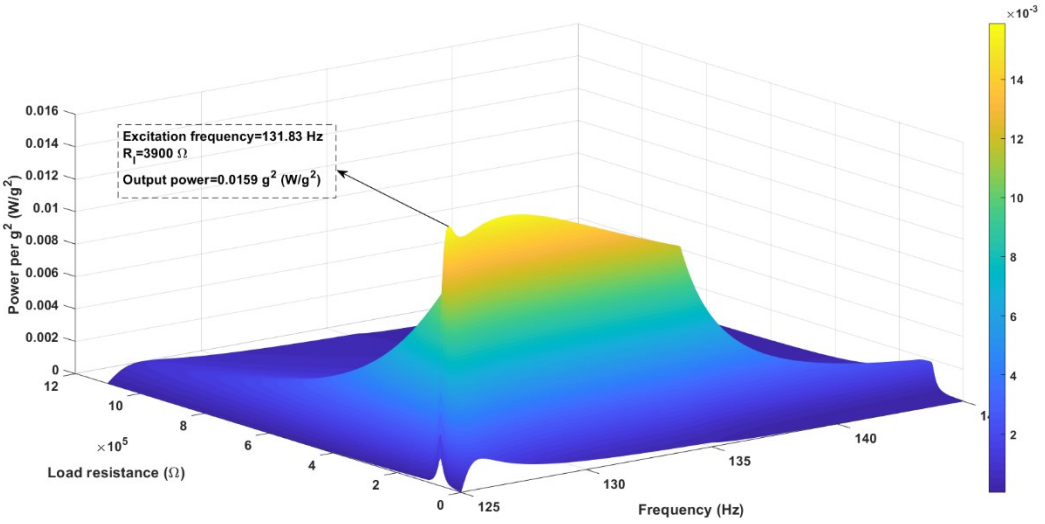

Figure 2.12 A 3D FRF for a wide range of the load resistance and excitation frequency.

2.4 Conclusions

In this chapter, finite element method with the application of the superconvergent element is employed to study the characteristics of the bimorph piezoelectric energy harvesters based on both the Timoshenko and Euler-Bernoulli beam theories. The current model is presented for a Timoshenko beam, but could be extended for the Euler–Bernoulli beam, as well. During the derivation, both linear piezoelectric and linear strain/stress relations are assumed. The harvester beam is assumed to be excited due to the vertical motion of its base at the root of the cantilever beam. The bending motion of the harvester at different excitation frequencies corresponds to the flapping vibration mode. In the mechanical modeling, the effects of both strain rate damping and external air damping are accurately treated in the final discretized equations by defining the proportional damping. The mechanical damping ratio could be identified from the experimental measurements including the half power bandwidth method or the logarithmic method which is working only for the first vibration mode.

The eletromechanical coupling equations are firstly derived for the general state of base excitations but after that they are extended only for the case of harmonic base motions. The derived analytical equations are then used to analyze the effects of different parameters on the output and the capacity of the harvester. The electrical outputs of the system are strictly dependent on the excitation frequency and the load resistance. To observe the frequency response behavior of the

electrical outputs, the FRFs for voltage, current and power outputs are identified and depicted. These three FRFs are plotted for five different orders of magnitude of the load resistance. Regardless of the electrical parameters, mechanical properties including natural frequencies and tip velocity of the energy harvester are obtained and the results are compared with the literature. For the purpose of validation, several examples are discussed. Validation of the results proves that SCE is an excellent element with very good rate of convergence. The shape functions adopted in finite element method are the exact solutions resulting from static equilibrium of the Timoshenko beam approach. This is why the SCE can more accurately follow the experimental results in comparison to the other methods. In other words, if one does not have the capability to formulate the characteristic functions as exact solutions, it is expected that those results be less accurate. In SCE only very few elements are required to capture the outputs, which significantly reduces the time and the cost of computation. Although this element is derived from static equilibrium, it has shown its capability for the analysis of dynamic problems.

Calculation of the relative errors in the different assessed examples represent that in the worst case the maximum percentage of error between the predicted values and the experimental ones is less than approximately 5%. Also, the effect of slenderness ratio is investigated showing that only for the smaller values of slenderness ratio (less than 5) it is more suitable to model the beam using the Timoshenko assumptions. Thus, the kind of applied beam theory strongly depends on the geometric parameters of the energy harvester so that the inclusion of the shear deformation and the rotary inertia in modelling is negligible for large beams.

Chapter 3 Performance of tapered cantilever piezoelectric energy harvester based on Euler-Bernoulli and Timoshenko beam theories

The cantilever beam configuration plays an important role on the power extracted from the vibration based piezoelectric energy harvesters (PEHs). Although it has already been proven that triangular and trapezoidal shapes optimize and improve the electrical output of the PEHs, the impact of other shapes have not been considered. It is necessary to figure out which shape can provide the maximum amount of power and efficiency, as well. In this chapter, a complete study regarding the influence of non-uniform theories using both Timoshenko and Euler-Bernoulli beams for both unimorph and bimorph states is carried out. The width and height of the cantilever beams are changed based on the degree of polynomial functions. To solve the equations, finite element method (FEM) with the application of two different elements including four-degree-of-freedom (DOF) model, and eight-DOF model is adopted. Based on the analysis, it can be concluded that by increasing the degree of non-uniformity and slenderness ratio the amount of harvested electrical output rises. Moreover, the difference between two beam theories is significant for thick beams with small slenderness ratios. Additionally, the effects of non-uniformity including the tapering ratio described by polynomial functions on the efficiency of PEHs are studied.

3.1 Introduction

There are three basic mechanisms which have been used to convert mechanical vibrations to electrical energy, namely, electro-magnetic, electrostatic and piezoelectric [6]. Among these three methods, piezoelectric PEHs have received consideration owing to its simple structure, high electrical output, and efficiency. Although there are different boundary conditions for the system, the cantilever configuration is the most effective option due to its maximum deflection in comparison to other beam boundary conditions. To model the PEHs there are two basic options namely unimorph (one layer of piezoelectric), and bimorph (two layers of piezoelectric) with parallel and series circuits. Many studies have been carried out to analyze the power scavenged from the rectangular energy harvesters using the above configurations [3, 54, 60, 62, 66, 67].

The need for improvements in power generation has pushed researchers forward to find ways to reach higher efficiency. Optimization methods have been adopted to improve the efficiency of systems. To optimize PEHs, different design variables such as shape, size, material properties and damping can be considered. Shape optimization or geometry modification represents an effective approach because it is possible to enhance the deflection of the free end of cantilever beam using diverging beams which result in uniform strain distribution along the beam's length and higher power extraction [68]. In this regard, Goldschmidtboeing and Woias [69] studied different triangular-shaped and rectangular-shaped beams, showing that using triangular state the excitation amplitude and maximum output power increases dramatically. Two optimized trapezoidal configurations were identified and validated experimentally by Benasciutti et al. [70]. In another study the effects of varying cross-sectional area of bimorph configuration on the electromechanical behavior of PEHs was discussed analytically and experimentally [71]. To calculate the power generated for non-uniform beams, Salmani et al. [72] presented an exact analytical solution for the exponentially tapered piezoelectric beam with tip mass in both unimorph and bimorph with parallel and series connections. They also verified the results both numerically and experimentally. Siddiqui et al. [73] carried out an extensive experimental characterization of tapered bimorphs with varying sizes and also with and without the presence of a tip mass. In addition to the tapered width, varying thickness is another practical method which was adopted to improve the power output of PEHs [74, 75]. It is noteworthy that a taper in thickness of a cantilever has a more significant contribution on the beam's stiffness than that from the taper in width owing to the more significant

impact of thickness on the second moment of area. In a recent work, Sahoo and Pandey [76] investigated the performance of non-uniform cantilever beams with linearly and quartic varying widths in a unimorph condition. They proved that the diverging beam with tapering parameter can produce an enhanced power output in comparison to that of uniform beam. However, if increasing the frequency of the structure is the goal the converging beam should be taken into consideration.

Analysis of non-uniform beams for the various degrees of polynomial function describing the non-uniformity has not been reported so far. More importantly, all the studies have been carried out assuming Euler-Bernoulli beam theory, although for short beams consideration of higher theory, namely Timoshenko, is essential due to the noticeable effect of shear stress. To conduct the analysis, the mathematical modeling of system with non-uniform width and height is expanded following the Rayleigh–Ritz method based on distributed parameter model developed for uniform structures [3]. The eletromechanical equations are derived for both unimorph and bimorph PEHs subjected to base excitation. Although the damping ratio of non-uniform and uniform beams are different, they are assumed to be the same for the analysis since the focus of study is on the assessment of frequency and the electrical output. However, in order to improve the results, the actual variation of damping ratios should be included. To solve the governing equations of the system different methods have been followed. Earlier studies have evaluated the system's performance numerically [3, 70-80], analytically [3, 60, 69, 71, 72, 81], and experimentally [3, 67, 70-73]. Since there are no analytical solutions for the beam with the varying width and thickness, finite element method is applied to calculate the natural frequency and FRFs for electrical outputs. In fact, after derivation of the total energy of the system, Hamilton's principle and finite element method are applied to obtain the discretized governing equations of the coupled electromechanical system. The frequency response functions (FRF) of the voltage is defined by assuming harmonic excitation. Furthermore, the results of both beam theories are compared to conclude which type of configuration provides more accurate predictions for different geometric parameters. In this study, in order to reach more accurate results two different elements including four-degree-of-freedom (DOF) model [52], and eight-DOF model [82] for the Euler and Timoshenko beams have been applied, respectively. Both elements have high convergence rates such that using the small number of elements provide responses with high accuracy. Since the convergence rate of eight-DOF is high for Timoshenko beam this is used [83]. To validate the results, the numerical solutions are verified using the experimental, analytical, and also numerical results of other studies reported in

the literature. Finally, to better evaluate the effect of non-uniformity on the performance of structure, the variation of efficiency for a wide range of tapering ratios and polynomial degrees is investigated.

3.2 Electro-mechanical modelling

In this section, the theoretical modelling of the cantilever beam with non-uniform width, *b(x)*, and height, *h(x)*, is presented in Fig. 3.1. It is assumed that there is no slip between the piezoceramic layers and the substrate layer (perfect bonding). Since two different models, namely unimorph and bimorph, are studied here, this section is divided into two subsections to derive the equations separately.

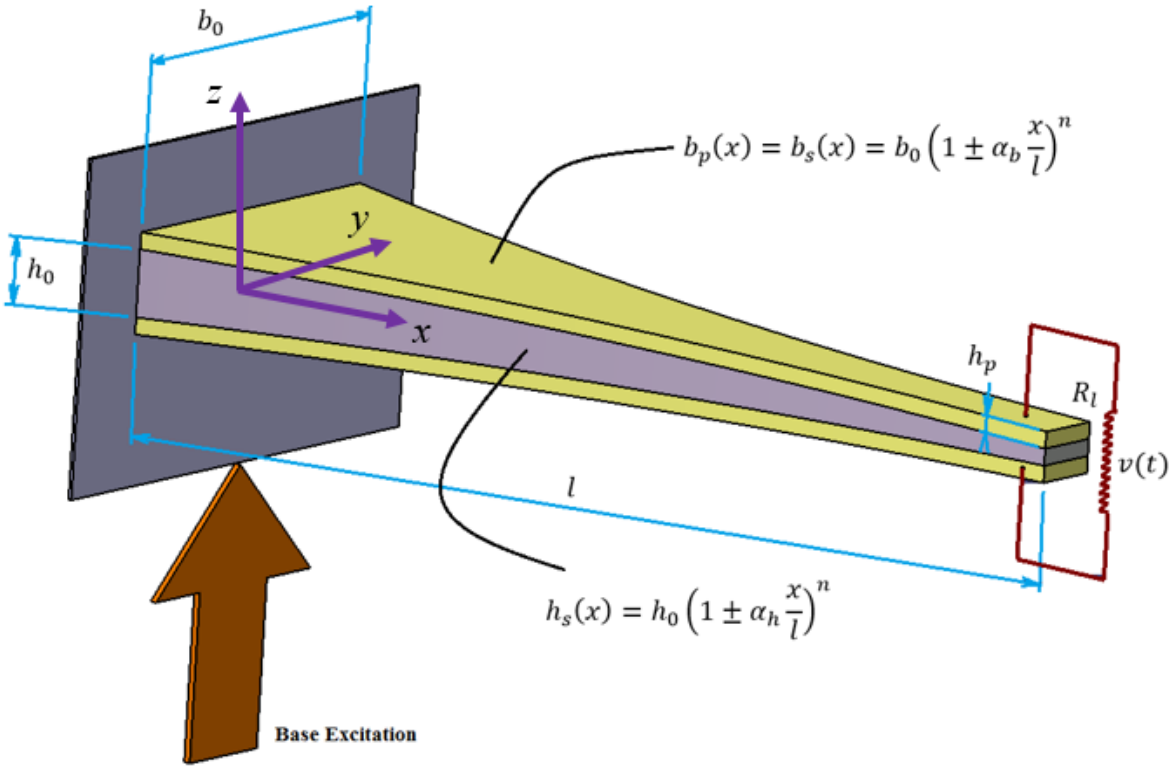

Figure 3.1 A schematic of piezoelectric based cantilever energy harvester with non-uniform width and height.

3.2.1 Equations of non-uniform unimorph PEHs

To derive the governing equations of piezoelectric cantilever beam with the varying thickness and width, the same procedure as Erturk and Inman [3] is followed. The only difference is the

cross section which is changing along the beam's length. The unimorph piezoelectric beam is shown in Fig.3.2. In the figure, h_p is the thickness of the piezoelectric layer, $h_s(x)$ is the thickness of the substrate, $b_p(x)$ is the width of piezoelectric layer, $b_s(x)$ is the width of substrate layer and L is the length of the cantilever beam. For the flapping mode, the position vectors of a generic point on the cantilever beam is represented by Eq. 2.1. Eqs. 2.1 -2.4 are repeated below for convenience.

$$\boldsymbol{R} = R_x\hat{I} + R_z\hat{K} = u\hat{I} + w\hat{K} \tag{2.1}$$

Considering a Timoshenko beam, the displacement of a generic point can be defined by:

$$u(x,y,z,t) = u_0(x,t) + z\phi_x(x,t) \tag{2.2}$$
$$v(x,y,z,t) = v_0(x,y,t) = 0 \tag{2.3}$$
$$w(x,y,z,t) = w_0(x,t) + g(t) \tag{2.4}$$

where u_0, v_0, and w_0 are the displacements projected on the mid-plane, ϕ_x is the rotation of corresponding cross section at point x and time t relative to the moving base and $g(t)$ is the translation in the transverse direction resulting from the base motion.

Using the definition of Lagrange strain tensor and using the non-zero components of the flexible displacement, the normal and shear strains are obtained as

$$\begin{cases} \epsilon_p = \dfrac{\partial u}{\partial x} = \acute{u}_0 + z\acute{\phi}_x & h_s - \overline{Y} \le z \le h_s + h_p - \overline{Y} \\ \epsilon_{xx} = \dfrac{\partial u}{\partial x} = \acute{u}_0 + z\acute{\phi}_x & -\overline{Y} \le z \le h_s - \overline{Y} \end{cases} \tag{3.1}$$

$$\begin{cases} \gamma_p = \dfrac{\partial u}{\partial z} + \dfrac{\partial w}{\partial x} = \phi_x + \acute{w}_0 & h_s - \overline{Y} \le z \le h_s + h_p - \overline{Y} \\ \gamma_{xz} = \dfrac{\partial u}{\partial z} + \dfrac{\partial w}{\partial x} = \phi_x + \acute{w}_0 & -\overline{Y} \le z \le h_s - \overline{Y} \end{cases} \tag{3.2}$$

where $\overline{Y}$ is the location of neutral axis. The calculations associated with the position of the neutral axis of the asymmetric unimorph structure are provided in Appendix A. equations separately.

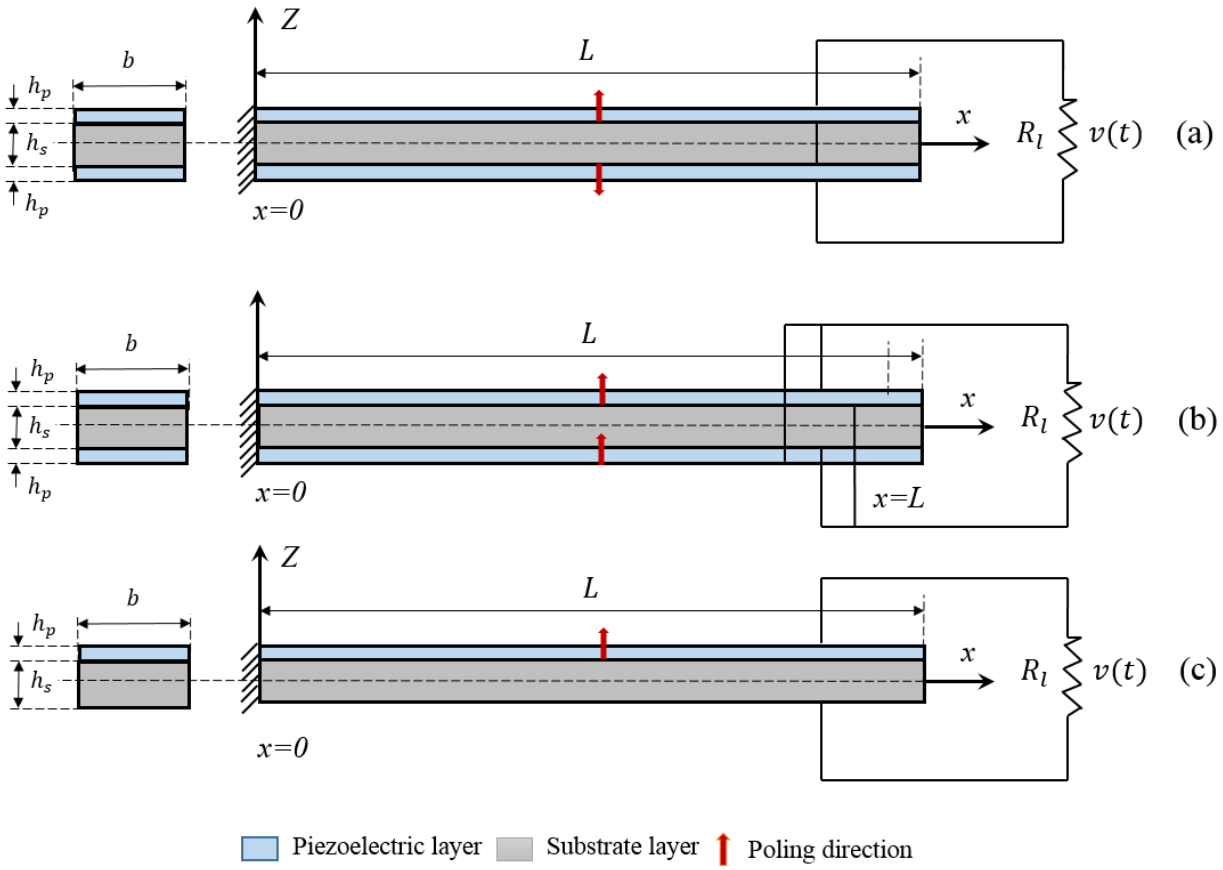

Figure 3.2 (a) Cantilevered bimorph beam under series connection (b) cantilevered bimorph beam under parallel connection(c) cantilevered unimorph beam.

With the assumption of linear piezoelectric constitutive equations [53], the reduced piezoelectric constitutive equations of a Timoshenko beam could be expressed using the following constitutive equations [3, 84] (Equations 2.7 – 2.22 are repeated as such for convenience)

$$\begin{Bmatrix} \epsilon_p \\ \gamma_p \\ D_3 \end{Bmatrix} = \begin{bmatrix} \frac{1}{E_p} & 0 & d_{31} \\ 0 & \frac{1}{K_s G_p} & 0 \\ d_{31} & 0 & \varepsilon_{33}^T \end{bmatrix} \begin{Bmatrix} \sigma_p \\ \tau_p \\ E_3 \end{Bmatrix} \tag{2.7}$$

where σ_p is the normal stress, τ_p is the shear stress, ϵ_p is the normal strain, γ_p is the shear strain, G_p is the shear modulus, E_p is the elastic modulus, D_3 is the electric displacement, d_{31} is the piezoelectric strain coefficient, ε_{33}^T is the dielectric permittivity of piezoelectric layer at constant

stress. Additionally, K_s is the shear correction factor which is 5/6 for a beam with a rectangular cross section and $E_3$is the electric field across the piezoelectric layer which can be defined based on Eq. 2.8.

$$E_3(t) = -\frac{v(t)}{h_p} \tag{2.8}$$

Considering the non-zero strains in Eqs. 3.1 and 3.2 and application of Hooke's Law, structural relations for the substrate layer are as follows

$$\tau_{xz} = K_s G_s \gamma_{xz} = K_s G_s (\phi_x + \acute{w}_0) \tag{2.9}$$

$$\sigma_{xx} = E_s \epsilon_{xx} = E_s \left(\acute{u}_0 + z\acute{\phi}_x\right) \tag{2.10}$$

where E_s and G_s are Young's modulus and shear modulus, respectively.

3.2.2 Kinetic and strain energies

In order to arrive at the governing equations of the system, it is necessary to firstly calculate the kinetic and strain energies of the entire structure using the following equations.

$$\begin{aligned} U = \frac{1}{2}\int [\sigma_{xx}\epsilon_{xx} + \tau_{xz}\gamma_{xz}]dV_s + \frac{1}{2}\int \left[\sigma_p \epsilon_p + \tau_p \gamma_p\right] dV_p \\ = \frac{1}{2}\int_0^L \Big[\left(I_0^E \acute{u}_0{}^2 + I_2^E \acute{\phi}_x{}^2 + 2I_1^E \acute{u}_0 \acute{\phi}_x\right) \\ + I_0^G \left(\acute{w}_0{}^2 + \phi_x{}^2 + 2\phi_x \acute{w}_0\right)\Big] dx \\ + \frac{1}{2}\int_0^L \Big[\left(J_0^E \acute{u}_0{}^2 + J_2^E \acute{\phi}_x{}^2 + 2J_1^E \acute{u}_0 \acute{\phi}_x\right) + J_0^G \left(\acute{w}_0{}^2 + \phi_x{}^2 + 2\phi_x \acute{w}_0\right) \\ + \frac{d_{31}}{h_p} J_0^E v(t) \acute{u}_0 + \frac{d_{31}}{h_p} J_1^E v(t) \acute{\phi}_x \Big] dx \end{aligned} \tag{2.13}$$

$$T = \frac{1}{2}\int \rho(\dot{\boldsymbol{R}}.\dot{\boldsymbol{R}})dV$$

$$= \frac{1}{2}\int_0^L \left[I_0^\rho \dot{u}_0{}^2 + I_0^\rho \dot{w}_0{}^2 + 2I_0^\rho \dot{w}_0\dot{g} + I_0^\rho \dot{g}^2 + 2I_1^\rho \dot{u}_0\dot{\phi}_x + I_2^\rho \dot{\phi}_x{}^2\right] dx \tag{2.14}$$

$$+ \frac{1}{2}\int_0^L \left[J_0^\rho \dot{u}_0{}^2 + J_0^\rho \dot{w}_0{}^2 + 2J_0^\rho \dot{w}_0\dot{g} + J_0^\rho \dot{g}^2 + 2J_1^\rho \dot{u}_0\dot{\phi}_x + J_2^\rho \dot{\phi}_x{}^2\right] dx$$

where

$$I_i^E \triangleq \iint z^i E_s dydz\,,\quad I_0^G \triangleq \iint K_s z^i G_s dydz\,,\quad I_i^\rho \triangleq \iint z^i \rho_s dydz\,, i = 0,1,2 \tag{2.15}$$

$$J_i^E \triangleq \iint z^i E_p dydz\,,\quad J_0^G \triangleq \iint K_s z^i G_p dydz\,,\quad J_i^\rho \triangleq \iint z^i \rho_p dydz\,, i = 0,1,2 \tag{2.16}$$

The terms J_0^E and J_1^E are the piezoelectric coupling terms so that the former couples the voltage and the extension components and the latter couples the voltage and the curvature components. Eq. 2.17 represents the calculation of the internal electrical energy in the piezoelectric layer

$$\mathrm{W}_{IE} = \frac{1}{2}\int E_3 D_3\, dV_p = -\frac{1}{2}\frac{v(t)}{h_p}\int \left[E_p d_{31}(\acute{u}_0 + z\acute{\phi}_x) - \frac{v(t)}{h_p}\varepsilon_{33}^S\right] dV_p$$

$$= -\frac{1}{2}\frac{v(t)}{h_p} d_{31}\int_0^L (J_0^E \acute{u}_0 + J_1^E \acute{\phi}_x) dx + \frac{1}{2} C_p v(t)^2 \tag{2.17}$$

The parameter C_p is the internal capacitance of the piezoceramic calculated as follows:

$$C_p = \varepsilon_{33}^S \frac{A_p}{h_p} \tag{2.18}$$

where ε_{33}^{S} and A_p are the dielectric permittivity at constant strain and the electrode area, respectively.

The energy expressions are used in the extended Hamilton's principle as follows:

$$\int_{t_1}^{t_2} (\delta T - \delta U + \delta W_{IE} + \delta W_{nc}) dt = 0 \tag{2.21}$$

where δT, δU, δW_{IE} and δW_{nc} are the virtual works of the total kinetic energy, the strain energy, the internal electrical energy and the non-conservative mechanical force, respectively. The only non-conservative virtual work is resulted from the electric charge output $Q_u(t)$ which is defined as follows

$$\delta W_{nc} = Q_u(t)\delta v_u(t) \tag{2.22}$$

To have a precise model, it is necessary to add the effects of damping for the analysis of the performance of the dynamic systems. The present study uses stiffness and mass proportional damping, namely, Rayleigh damping [65].

3.2.3 Equations of non-uniform bimorph PEHs method

For a unimorph beam including two layers of piezoelectric and one layer of substrate, there are two different ways of connection, namely, parallel and series schemes between the top and the bottom layers [3]. The relationships between the characteristics of the piezoceramic layers including voltages, charges and piezoelectric strain coefficients in the serial and the parallel connections are as follows, respectively.

$$v^T = v^B = \frac{v}{2} \quad and \quad d_{31}^T = -d_{31}^B \quad and \quad Q^T = Q^B = Q \tag{3.3}$$

$$v^T = -v^B = v \quad and \quad d_{31}^T = d_{31}^B \quad and \quad Q^T = -Q^B = \frac{Q}{2} \tag{3.4}$$

where superscripts T and B denote the top and the bottom piezoceramic layers, respectively.

3.3 Discretization of equations

In order to discretize the coupled model, FEM with two different elements, including four-DOF and eight-DOF, are employed.

3.3.1 Four-degree-of-freedom (DOF) model

This type of element contains two nodes and four degrees-of-freedom (DOF), including two DOF in the transverse direction and two DOF in the rotational direction (Fig. 2.2). The shape functions are derived by using static equilibrium (Appendix C). As a significant benefit, this element has simple transferring method from the Timoshenko to the Euler-Bernoulli beam such that by changing the value of one coefficient one can analyze both beam theories without performing extra calculations [52].

Using these shape functions for the element, the displacement parameters in terms of the nodal displacements are represented in Eq. 2.24.

$$\begin{bmatrix} u_0(x,t) \\ w_0(x,t) \\ \phi_x(x,t) \end{bmatrix} = \begin{bmatrix} \chi_1^e(x) & 0 & 0 & \chi_2^e(x) & 0 & 0 \\ 0 & \psi_1^e(x) & \psi_2^e(x) & 0 & \psi_3^e(x) & \psi_4^e(x) \\ 0 & \varphi_1^e(x) & \varphi_2^e(x) & 0 & \varphi_3^e(x) & \varphi_4^e(x) \end{bmatrix} \begin{bmatrix} U_1^e(t) \\ W_1^e(t) \\ \phi_1^e(t) \\ U_2^e(t) \\ W_2^e(t) \\ \phi_2^e(t) \end{bmatrix} \tag{2.24}$$

3.3.2 Eight-degree-of-freedom (DOF) model

This element was proposed by Reddy [85] for a rectangular beam while it is used here for a non-uniform Timoshenko beam. The element has two nodes and every node has four DOF. In fact, the nodal displacement vector consists of transverse displacement node, bending rotation, and their derivatives, as well. In this element, Hermitian shape functions are employed for the estimations of transverse displacement and bending rotation (Appendix D).

Taking these shape functions into consideration, the displacement parameters in terms of the nodal displacements are represented in Eq. 3.5.

$$\begin{bmatrix} u_0(x,t) \\ w_0(x,t) \\ \phi_x(x,t) \end{bmatrix} = \begin{bmatrix} N_u(x) \\ N_w(x) \\ N_\phi(x) \end{bmatrix} a(t)$$

$$= \begin{bmatrix} \chi_1^e(x) & 0 & 0 & 0 & 0 & \chi_2^e(x) & 0 & 0 & 0 & 0 \\ 0 & f_1 & 0 & f_2 & 0 & 0 & f_3 & 0 & f_4 & 0 \\ 0 & 0 & f_1 & 0 & f_2 & 0 & 0 & f_3 & 0 & f_4 \end{bmatrix} \begin{bmatrix} U_1^e(t) \\ W_1^e(t) \\ \phi_1^e(t) \\ W_1'^e(t) \\ \phi_1'^e(t) \\ U_2^e(t) \\ W_2^e(t) \\ \phi_2^e(t) \\ W_2'^e(t) \\ \phi_2'^e(t) \end{bmatrix} \tag{3.5}$$

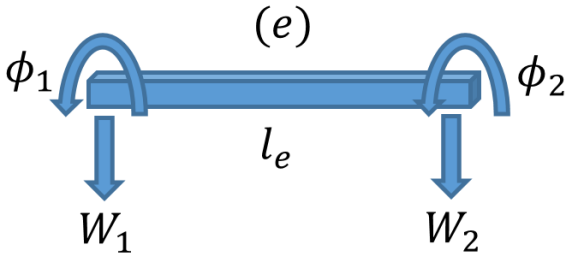

Figure 2.2 Two-node finite element with four DOF.

where $N_w(x)$ and $N_\phi(x)$ are the shape functions and $a(t)$ is the unknown generalized coordinates. By substitution of Eq. 3.5 or 2.24 into Eq. 2.21 and by performing integration by parts, the electromechanical coupling equations for a typical finite element is summarized in Eqs. 2.25 and 2.26. To complete the modelling, Rayleigh damping (proportional damping) is added to the equations at this stage to account for the mechanical dissipative effects (Eq. 2.28).

$$\boldsymbol{M^e \ddot{a}(t) + C^e \dot{a}(t) + K^e a(t) - \theta^e v(t) = f^e} \tag{2.25}$$

$$\overline{C_p} \dot{v}_u(t) + \frac{v(t)}{R_l} + \boldsymbol{\theta_u^{eT} \dot{a}(t)} = 0 \tag{2.27}$$

$$\boldsymbol{C^e} = \mu \boldsymbol{M^e} + \gamma \boldsymbol{K^e} \tag{2.28}$$

where μ and γ are the constants of mass and stiffness proportionality. Terms $\boldsymbol{M}^e$, $\boldsymbol{C}^e$, $\boldsymbol{K}^e$, $\boldsymbol{\theta}^e$, $\boldsymbol{f}^e$ are, respectively, the mass matrix; the damping matrix; the elastic stiffness matrix; the electromechanical coupling matrix and the vector of dynamical forces corresponding to one element of the piezoelectric cantilever beam, and $\overline{C}_p$ is the equivalent capacitance (Appendix E).

3.4 Solution of coupling equations

In this section, the solution of electromechanical coupling equations is presented. Assembling the elements of the beam and considering the input in the harmonic form $g(t) = Xe^{i\omega t}$ the components of the forcing vector become:

$$\boldsymbol{f}^e = \left[\omega^2 X \int_0^{l_e} \left(I_0^\rho + J_0^\rho\right) {N_w}^T dx\right] e^{i\omega t} \tag{2.29}$$

By definition of the steady-state response and the voltage output as $\boldsymbol{a}(\boldsymbol{t}) = \boldsymbol{A}e^{i\omega t}$ and $v = Ve^{i\omega t}$, the assembled steady-state forms of electromechanical coupling equations are expressed as follows:

$$(-\boldsymbol{M}\omega^2 + i\omega\boldsymbol{C} + \boldsymbol{K})\boldsymbol{A} - \boldsymbol{\theta}V = \boldsymbol{F} \tag{2.30}$$

$$i\omega\boldsymbol{\theta}^{\boldsymbol{T}}\boldsymbol{A} + \left(i\omega\overline{C_p} + \frac{1}{R_l}\right)V = 0 \tag{2.31}$$

By extracting the amplitude vector from Eq. 2.30 and substituting in Eq. 2.31, the complex voltage is obtained as

$$\begin{aligned} v(t) = -i\omega\left(i\omega\overline{C_p} + \frac{1}{R_l}\right)^{-1} \boldsymbol{\theta}^{\boldsymbol{T}} \Big[-\boldsymbol{M}\omega^2 + i\omega\boldsymbol{C} + \boldsymbol{K} \\ + i\omega\left(i\omega\overline{C_p} + \frac{1}{R_l}\right)^{-1} \boldsymbol{\theta}\boldsymbol{\theta}^{\boldsymbol{T}}\Big]^{-1} \boldsymbol{F}e^{i\omega t} \end{aligned} \tag{2.34}$$

3.5 Shape optimization

Different types of measurements have been used for the assessment of the performance piezoelectric energy harvesters. Output electrical power extracted from the piezoelectric structures is one of the important parameters which has been widely used. Although application of output power is a useful method to evaluate the performance of PEHs, its direct relevance as the comparing metric is not sufficient because the value strongly depends on different parameters including the size, vibration environment and circuit conditions. Hence, other parameters such as the power density and efficiency have drawn considerable attention among researchers. Efficiency is a strong indication of the amount of energy that a piezoelectric structure can convert from the input mechanical power (P_{in}) into the output electrical power (P_{out}). Here, the efficiency of harvesting structure is defined as:

$$\Gamma = \frac{P_{out}}{P_{in}} \tag{3.6}$$

where P_{in} comes from the base excitation (shaker). Based on the electromechanical coupling equations, the provided energy by the base excitation is thus [86]

$$P_{in} = \boldsymbol{f^e \dot{a}(t)} \tag{3.7}$$

By expressing the amount of extracted output power and the provided input energy, the efficiency of system is resulted as Eq. 3.8.

$$\begin{aligned} \Gamma &= \left| \frac{\boldsymbol{v(t) I(t)}}{\boldsymbol{f^e \dot{a}(t)}} \right| \\ &= \left| \frac{\left[-i\omega \left(i\omega \overline{C_p} + \frac{1}{R_l} \right)^{-1} \boldsymbol{\theta^T} \left[-\boldsymbol{M}\omega^2 + i\omega \boldsymbol{C} + \boldsymbol{K} + i\omega \left(i\omega \overline{C_p} + \frac{1}{R_l} \right)^{-1} \boldsymbol{\theta \theta^T} \right]^{-1} \right]^2 \boldsymbol{F^2}}{i \left[-\boldsymbol{M}\omega^2 + i\omega \boldsymbol{C} + \boldsymbol{K} + i\omega \left(i\omega \overline{C_p} + \frac{1}{R_l} \right)^{-1} \boldsymbol{\theta \theta^T} \right]^{-1} R_l \boldsymbol{F^2} \omega} \right| \end{aligned} \tag{3.8}$$

3.6 Results and discussion

The validation of the numerical solution is firstly carried out by comparing the calculated voltage and fundamental frequency for non-uniform beams with those available in the literature. Subsequently, the effects of Timoshenko beam theory for various geometries in the three configurations are investigated. Additionally, the influence of non-uniformity for different degrees of polynomial functions are studied to identify which function can provide the maximum desired electrical output. Eventually, the study is completed by investigation of the non-uniform geometry on the efficiency of structure for a wide range of external loads. It should be pointed out that all of the analytical results are obtained using Matlab.

In the first example, the convergence of 4-DOF element is verified by considering a non-uniform cantilever beam investigated by Salmani et al [72] wherein the width of the beam is varying exponentially through the length by $b(x) = b_0 e^{-cx}$. The properties of the studied piezoelectric beam are presented in Table 3.1. The substrate layer is made of steel which is covered with PZT-4 as the piezoelectric material. For this verification example, the output voltage generated for the three configurations are derived for five different tapering parameter, c, and listed in Table 3.2. In this example, the electrical resistance is taken to be 1000 Ω, and the damping ratio is assumed to be 1 percent. It is worth mentioning that to calculate the results only one 4-DOF element is used.

Table 3.1 Properties of the bimorph piezoelectric cantilever beam.

Property	Piezoelectric layer	Substrate layer
Material	PZT-4	Steel
Density ρ (kg/m^3)	7960	7800
Length (mm)	60	60
Thickness (mm)	0.6	0.7
Initial width b_0 (mm)	10	10
Young's modulus E (GPa)	81.3	200
Piezoelectric strain coefficient d31(pC/N)	-123	–
Dielectric permittivity at constant strain ε_{33}^{S} (nF/m)	13.059	–
Shear modulus G (GPa)	31.3	76.9

Table 3.2 Validation of piezoelectric energy harvester's voltage for different tapering values.

C	0	5	10	15	20
Unimorph					
Analytic (V/g) [72]	0.5711	0.499	0.438	0.3842	0.3377
4-DOF element (V/g)	0.5704	0.499	0.438	0.3856	0.3403
Difference (%)	0.12	0	0	0.36	0.77
Bimorph (series)					
Analytic (V/g) [72]	0.6252	0.5479	0.4802	0.4214	0.3704
4-DOF element (V/g)	0.6252	0.5470	0.4800	0.4225	0.3729
Difference (%)	0	0.16	0.042	0.26	0.67
Bimorph (parallel)					
Analytic (V/g) [72]	1.156	1.011	0.8847	0.7751	0.6805
4-DOF element (V/g)	1.154	1.009	0.8842	0.7772	0.6849
Difference (%)	0.17	0.20	0.057	0.27	0.65

It can be seen from Table 3.3 that, both analytical and numerical results are in good agreement such that in the worst case the maximum difference between these two methods is less than 1%. It means that 4-DOF element has the potential to predict the tapered piezoelectric energy harvester's behavior quite well. Additionally, the results show that by increasing tapering parameter the generated voltage per exciting acceleration decreases while leading to lighter structure. Therefore, based on the objective function one can optimize the mass or the desired electrical output.

In the second example, the validation of the presented 4-DOF element is performed for non-uniform beam with linearly and quartic varying width [76]. The first three frequencies of unimorph beam with varying width are calculated and are provided in Table 3.3. The width of the beam is changing according to $b(x) = b_0(1 \pm \alpha\frac{x}{l})^n$, where, n=1 for linearly varying beam, n=4 for quartic varying beams and eventually n=0 for uniform beams. The negative and positive signs represent the converging and diverging tapered beams, respectively.

Table 3.3 Validation of first three frequencies of uniform and non-uniform beams.

f	Uniform $\alpha = 0$	Linear $\alpha = -0.2$	Linear $\alpha = 0.2$	Quartic $\alpha = -0.2$	Quartic $\alpha = 0.2$
$f_1(Hz)$ [76]	47.82	50.97	45.16	62.40	38.07
f_1 (4-DOF)	48.80	52.29	46.09	63.98	38.69
Difference (%)	2.1	2.6	2.1	2.5	1.6
$f_2(Hz)$ [76]	299.67	306.31	294.78	325.86	279.68
f_2 (4-DOF)	302.53	308.69	297.60	327.97	283.26
Difference (%)	0.95	0.78	0.96	0.65	1.3
$f_3(Hz)$ [76]	839.25	845.65	834.46	865.24	820.48
f_3 (4-DOF)	851.07	856.45	847.09	874.71	836.63
Difference (%)	1.4	1.3	1.5	1.1	1.9

The computation shows that the presented 4-DOF can well predict the frequencies of tapered PEH with maximum 2.6% percentage error although only three 4-DOF elements are used. It is obvious for the converging beam that the frequencies increase while they decrease for the diverging beam with constant resistive load.

In the last part of validation, the accuracy of the present numerical solution is verified by analyzing a uniform bimorph cantilever beam experimentally investigated by [62]. The frequency response functions (FRFs) of output voltage using the experimental analysis and the present method are compared and depicted in Fig. 3.3. From the graphs it is visible that the results are in great agreement.

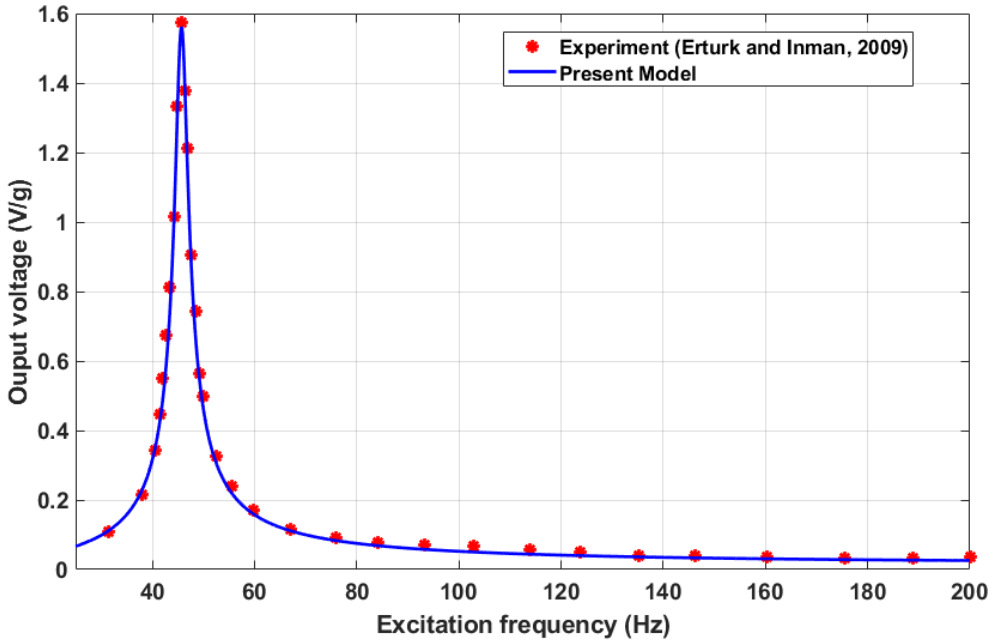

Figure 3.3 Validation of voltage FRF of a uniform bimorph piezoelectric energy harvester ($R_l = 1000,\ \xi = 0.027$).

To optimize the output of system, the effects of different tapering functions are investigated in the next example. The properties of the studied non-uniform bimorph beams in series state are the same as in example one, as listed in Table 3.1. The maximum output voltage for different types of non-uniform beams where the width and height are varying according to the polynomial functions with five different polynomial functions. The results are computed and summarized in Tables 3.4-3.8 for the electrical resistance 1000Ω and damping ratio 0.01.

Table 3.4 Piezoelectric energy harvester's voltage for linear tapered beam (n=1).

	α_ba	-0.6	-0.4	-0.2	0.2	0.4	0.6
α_hb							
-0.2		0.442	0.502	0.560	0.670	0.724	0.776
-0.4		0.435	0.494	0.551	0.659	0.711	0.762
-0.6		0.428	0.486	0.542	0.648	0.699	0.749
0.2		0.453	0.516	0.576	0.691	0.747	0.802
0.4		0.459	0.523	0.584	0.701	0.758	0.814
0.6		0.464	0.529	0.591	0.711	0.769	0.826

a: Tapering parameter of width, b: Tapering parameter of height

Table 3.5 Piezoelectric energy harvester's voltage for cubic tapered beam (n=2).

α_ba	-0.6	-0.4	-0.2	0.2	0.4	0.6
α_hb						
-0.2	0.321	0.408	0.503	0.720	0.841	0.969
-0.4	0.312	0.397	0.491	0.701	0.817	0.941
-0.6	0.302	0.386	0.478	0.684	0.797	0.918
0.2	0.339	0.430	0.532	0.768	0.901	1.043
0.4	0.348	0.442	0.549	0.797	0.937	1.088
0.6	0.357	0.455	0.567	0.827	0.976	1.136

a: Tapering parameter of width, b: Tapering parameter of height

Table 3.6 Piezoelectric energy harvester's voltage for quadratic tapered beam (n=3).

α_ba	-0.6	-0.4	-0.2	0.2	0.4	0.6
α_hb						
-0.2	0.238	0.333	0.454	0.776	0.981	1.220
-0.4	0.226	0.320	0.438	0.750	0.947	1.175
-0.6	0.215	0.308	0.424	0.730	0.922	1.144
0.2	0.260	0.361	0.493	0.858	1.098	1.382
0.4	0.271	0.378	0.519	0.919	1.184	1.500
0.6	0.282	0.396	0.549	0.983	1.274	1.620

a: Tapering parameter of width, b: Tapering parameter of height

Table 3.7 Piezoelectric energy harvester's voltage for quartic tapered beam (n=4).

α_ba	-0.6	-0.4	-0.2	0.2	0.4	0.6
α_hb						
-0.2	0.179	0.273	0.410	0.837	1.150	1.546
-0.4	0.165	0.258	0.392	0.806	1.106	1.483
-0.6	0.155	0.246	0.378	0.784	1.077	1.445
0.2	0.206	0.306	0.458	0.965	1.356	1.864
0.4	0.218	0.326	0.494	1.073	1.525	2.120
0.6	0.229	0.347	0.531	1.172	1.677	2.342

a: Tapering parameter of width, b: Tapering parameter of height

Table 3.8 Piezoelectric energy harvester's voltage for quintic tapered beam (n=5).

α_hb \ α_ba	-0.6	-0.4	-0.2	0.2	0.4	0.6
-0.2	0.136	0.225	0.371	0.906	1.354	1.975
-0.4	0.122	0.208	0.351	0.869	1.298	1.891
-0.6	0.113	0.197	0.338	0.846	1.267	1.848
0.2	0.167	0.262	0.426	1.093	1.695	2.562
0.4	0.179	0.284	0.471	1.259	1.985	3.041
0.6	0.188	0.302	0.506	1.373	2.177	3.353

a: Tapering parameter of width, b: Tapering parameter of height

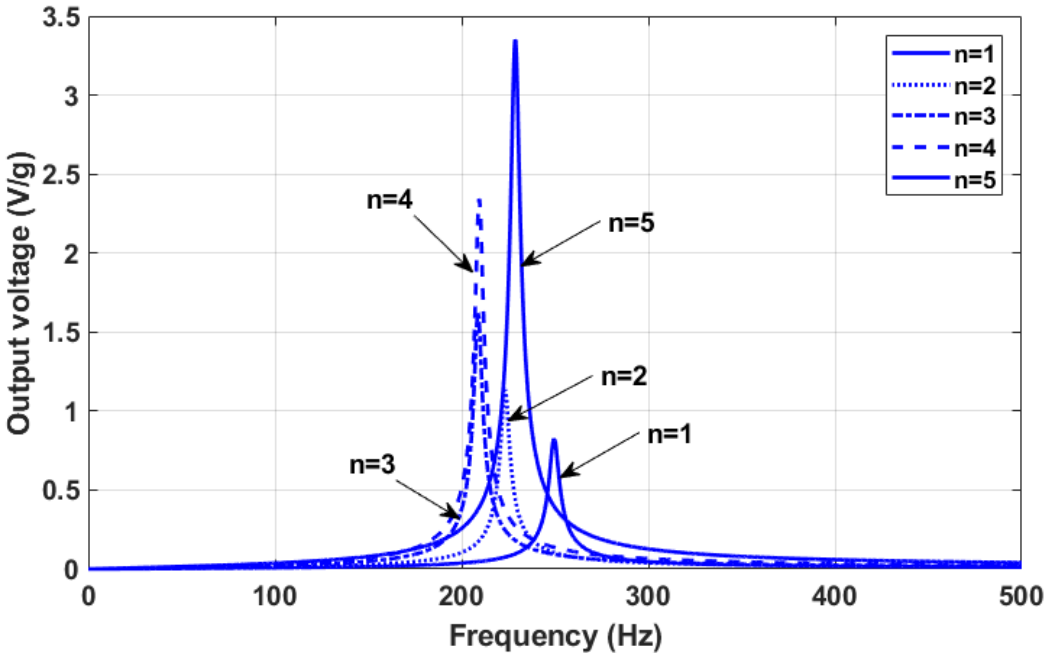

Figure 3.4 Voltage FRF curves for different degrees of polynomial ($\alpha = \alpha_b = \alpha_h = 0.6$).

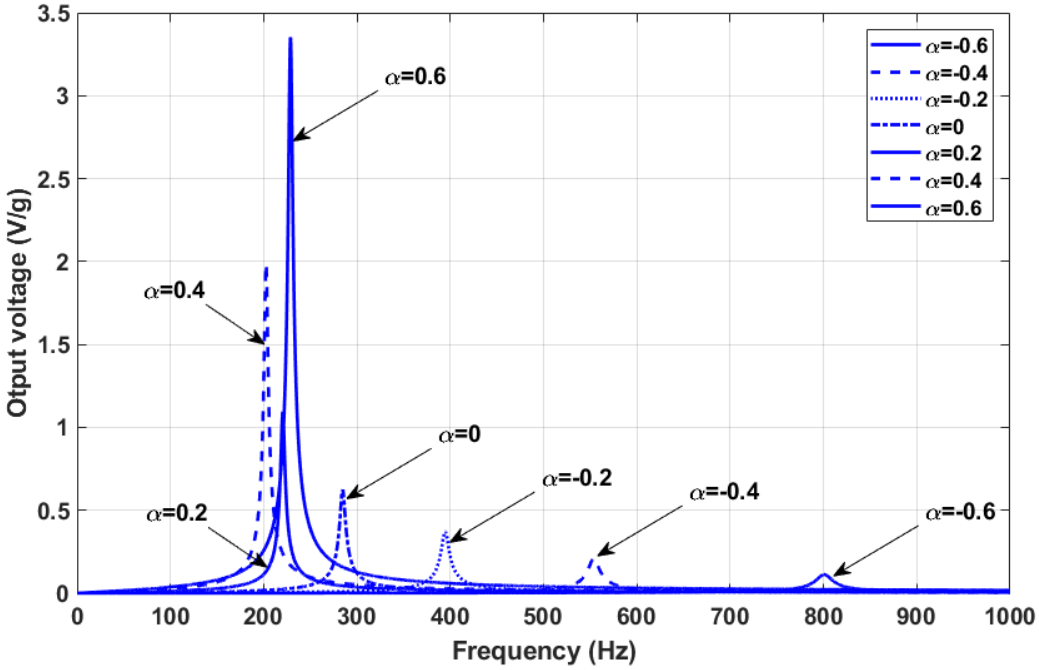

Figure 3.5 Voltage FRF curves for quintic tapered beam in both directions ($\alpha = \alpha_b = \alpha_h$).

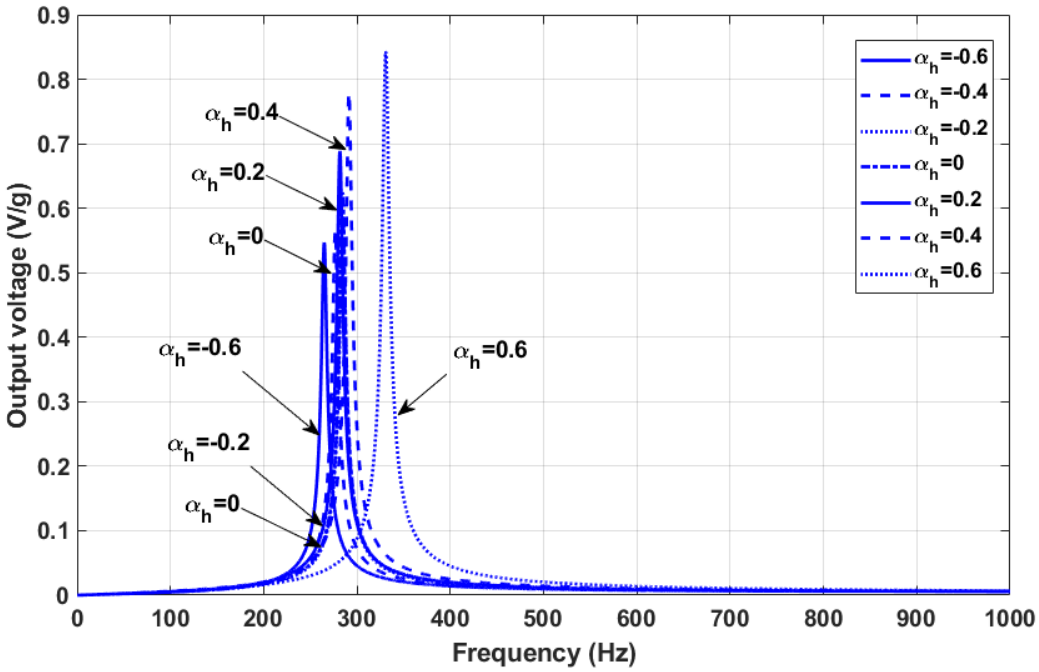

Figure 3.6 Voltage FRF curves for quintic tapered beam in width direction ($\alpha_h = \alpha, \alpha_b = 0$).

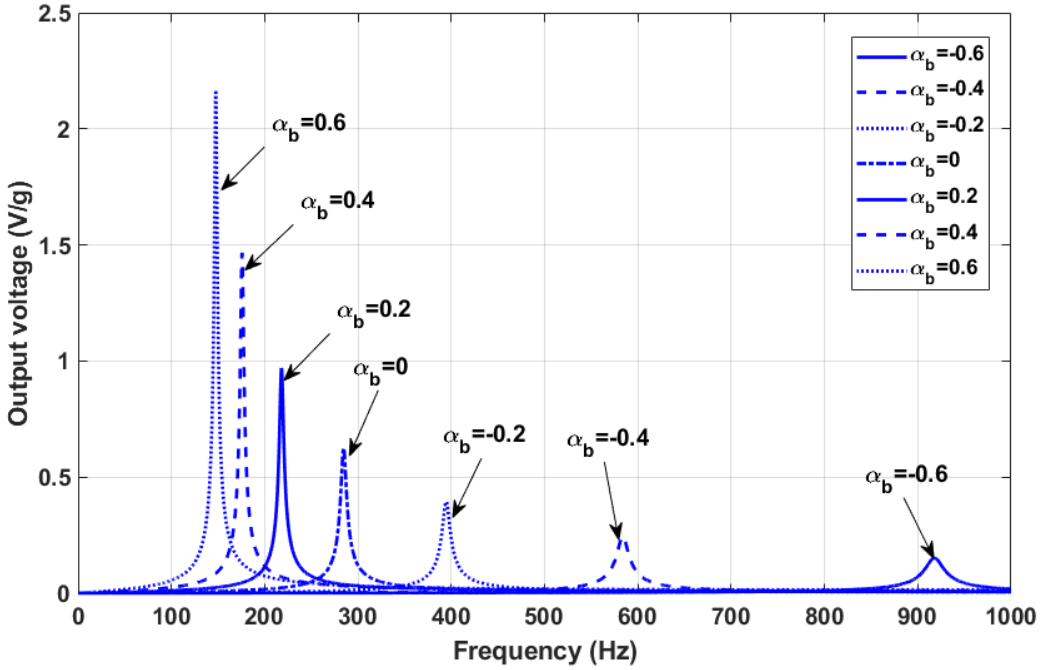

Figure 3.7 Voltage FRF curves for quintic tapered beam in width direction ($\alpha_b = \alpha, \alpha_h = 0$).

According to Tables 3.4-3.8 and Fig. 3.4, it can be concluded that the degree of polynomial has an increasing effect on the output voltage such that by changing the degree from one to five for both width and height, the maximum value of the voltage output rises by 306%. In fact, by changing the degree and tapering parameter it is possible to optimize the frequency and the desired electrical output. Additionally, from Fig. 3.5 and Table 3.8 it is obvious that changing the tapering parameter from the minimum value ($\alpha = -0.6$) to maximum value ($\alpha = 0.6$) results in increasing the maximum output voltage by 2867.3%. Last but not least, from Figs. 3.5-3.7 it is noted that by increasing the tapering parameter (converging to diverging) the first natural frequency of tapered beam in longitudinal and transversal directions decreases and increases, respectively, while the double-tapered beam (tapered in two directions) behaves differently (Fig. 3.5). Modelling PEHs using the appropriate beam theory plays an important role in achieving accurate results. Here the effects of two different beam theories are investigated to figure out the difference. The properties of the considered bimorph PEH in series state are the same as previous examples. The only difference is the length of the beam which is variable here.

Table 3.9 The electrical voltage of quintic tapered PEH for different slenderness ratios beam.

$S_r = \frac{L}{(2h_p + h_0)}$	Beam[a]	-0.6	-0.4	-0.2	0	0.2	0.4	0.6
2	P1	0.0045	0.0084	0.0154	0.0272	0.0475	0.0782	0.1091
	P2	0.0050	0.0089	0.0159	0.0280	0.0486	0.0822	0.1323
RD (%)		**11.11**	**5.95**	**3.25**	**2.94**	**2.32**	**5.12**	**21.26**
5	P1	0.0150	0.0277	0.0497	0.0858	0.1507	0.2649	0.4176
	P2	0.0151	0.0274	0.0493	0.0857	0.1472	0.2489	0.4121
RD (%)		**0.67**	**1.08**	**0.80**	**0.12**	**2.23**	**6.04**	**1.32**
10	P1	0.0333	0.0613	0.1095	0.1866	0.3272	0.5870	0.9677
	P2	0.0333	0.0610	0.1090	0.1864	0.3221	0.5522	0.8899
RD (%)		**0**	**0.49**	**0.46**	**0.11**	**1.56**	**5.93**	**8.04**
20	P1	0.0702	0.1293	0.2304	0.3897	0.6821	1.234	2.074
	P2	0.0702	0.1291	0.2300	0.3895	0.6781	1.198	1.921
RD (%)		**0**	**0.15**	**0.17**	**0.051**	**0.59**	**2.92**	**7.38**
50	P1	0.1813	0.3341	0.5938	0.9998	1.746	3.178	5.384
	P2	0.1812	0.3340	0.5938	1.0001	1.746	3.154	5.254
RD (%)		**0.055**	**0.03**	**0**	**0.03**	**0**	**0.76**	**2.41**

a P1=Euler-Bernoulli beam theory, P2=Timoshenko beam theory, b Relative difference

Table 3.9 indicates the effect of slenderness ratio on the electrical voltage of bimorph PEH in series connection. In this example, one 4-DOF element and one 8-DOF element are applied to compute the electrical output for Euler-Bernoulli and Timoshenko beam theories, respectively. It is obvious that for small slenderness ratios and larger values of tapering parameters the relative difference between two chosen beam theories is noticeable. From these results the difference is noticeable when the slenderness ratio is less than 10.

In the next part, the effects of degree of the polynomial and tapering parameters on the output voltage of tapered Euler-Bernoulli PEH for three different states including unimorph and bimorph with series and parallel connections are studied and depicted in Figs. 3.8-3.11. For three connections the maximum taper parameter ($\alpha = 0.6$) with the slender ratio $S_r = 30$ is considered. Since a large slenderness ratio is taken, the Euler-Bernoulli beam theory is applied to compute the

results. Analyzing the results expresses that higher degree leads to extracting higher voltage from the energy harvester. Although the difference between the output voltage of unimorph structure and bimorph in series connection is not significant, the values of bimorph in parallel connection are 150% larger.

The last part of this study is devoted to the evaluation of efficiency at various tapering parameters for the bimorph piezoelectric PEH in series connection. In the first step, the effects of load resistance is studied and depicted in Fig. 3.12. As it can be seen, the same trend is happening for all excitation frequencies so that the efficiency increases up from zero to certain locations and then decreases to reach a stabilization point when electrical resistance increases. With the consideration of the optimum load resistances, it also is obvious that the maximum efficiency is not exactly occurring at the open circuit or short circuit frequencies while these two important conditions were pointed to be the locations where maximum power is extracted [48, 62, 87, 88]. The maximum value takes places at the frequency ratio located between the resonant frequency (short circuit condition) and anti-resonant frequency (open circuit condition). Another noticeable aspect is that the efficiency peak for the open and short circuit conditions are approximately the same while there is a huge decrease when the input excitation frequency is out of this range. In fact, small deviations from the optimal frequency range will cause the device to perform with much diminished effectiveness. Here, the variation of efficiency is demonstrated for $\omega = 287.9\,Hz$ which is the average of open-circuit and short circuit frequencies. In the next step, the effect of non-uniformity is investigated and displayed in Figs. 3.13-3.15. By comparing the results, it can be concluded that by increasing the degree of polynomial function and application of converging beam the efficiency increases by 22%. Moreover, the results express that the effect of α_b is much stronger than α_h so that the maximum increase of 5% is achievable by changing α_h while the difference is 22% for α_b maintained under the same conditions. Thus, with the efficiency as the objective, only alteration of α_b could yield a feasible solution to noticeably improve the output and for this it is not necessary to converge beam in the height direction.

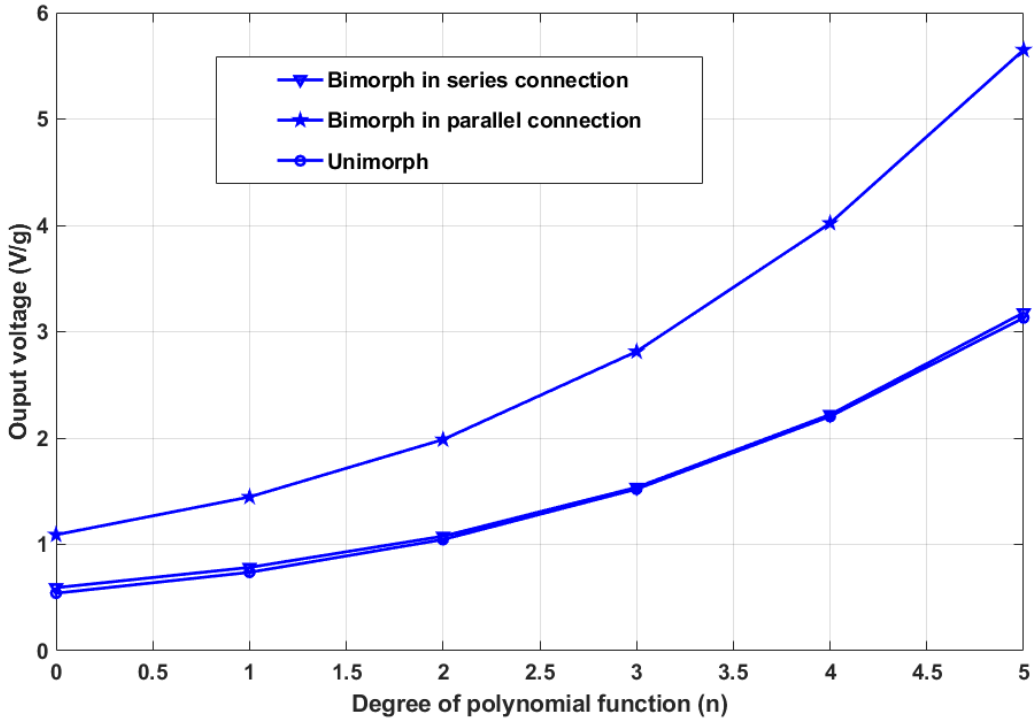

Figure 3.8 The variation of output voltage versus different degrees of polynomial function.

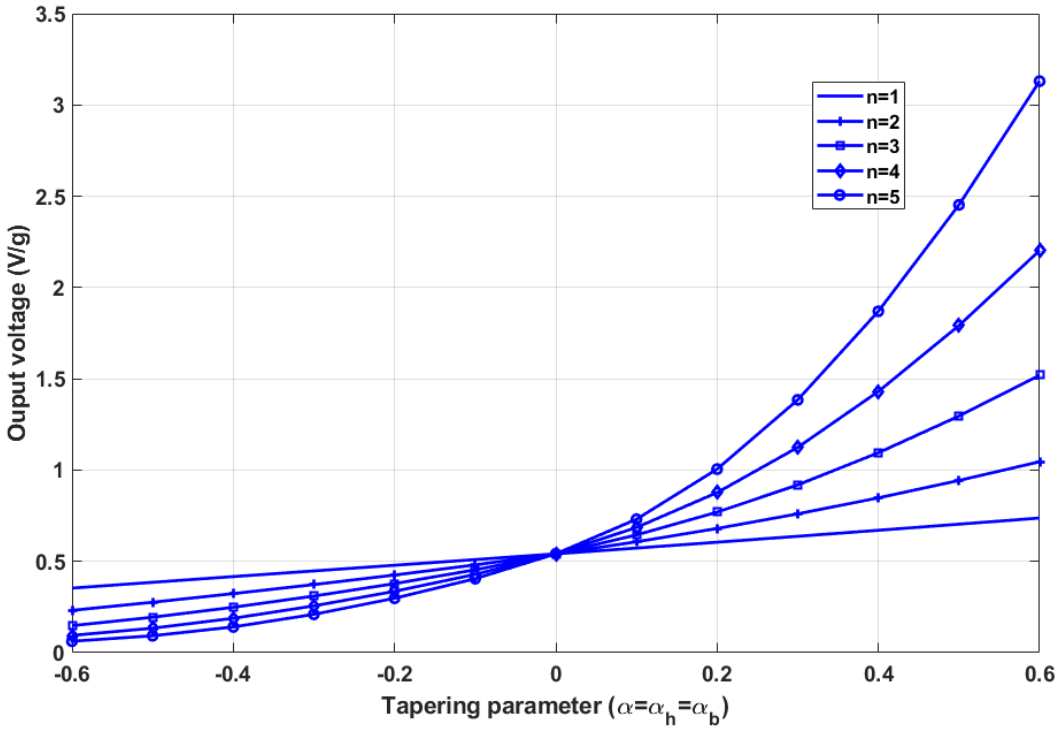

Figure 3.9 Tapering effects on unimorph PEH.

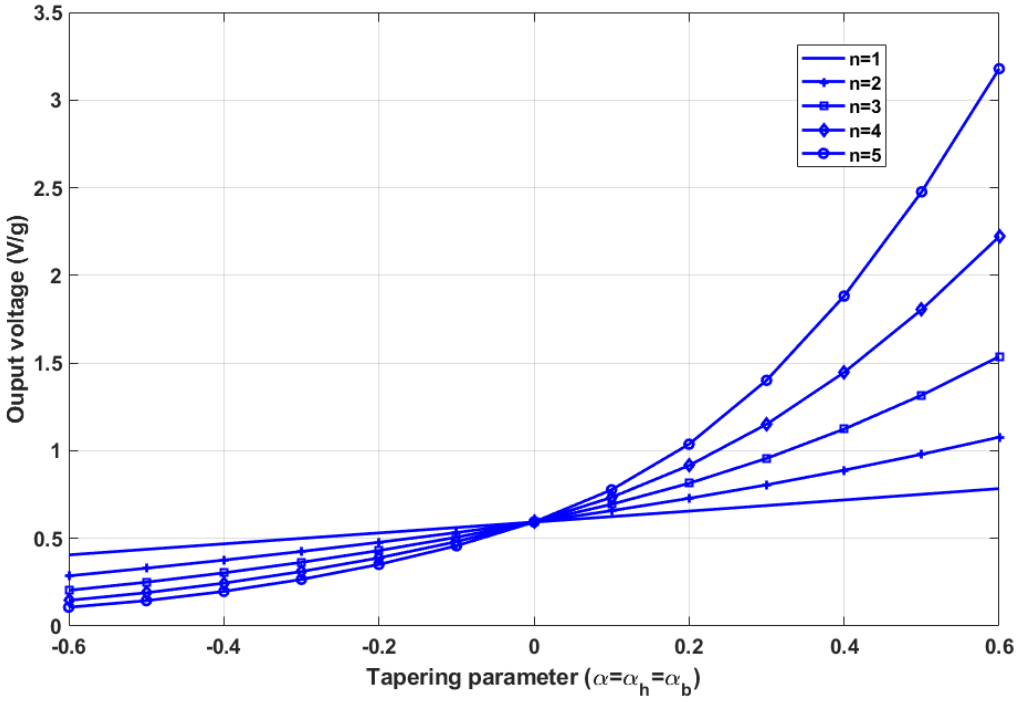

Figure 3.10 Tapering effects on bimorph PEH with series connection.

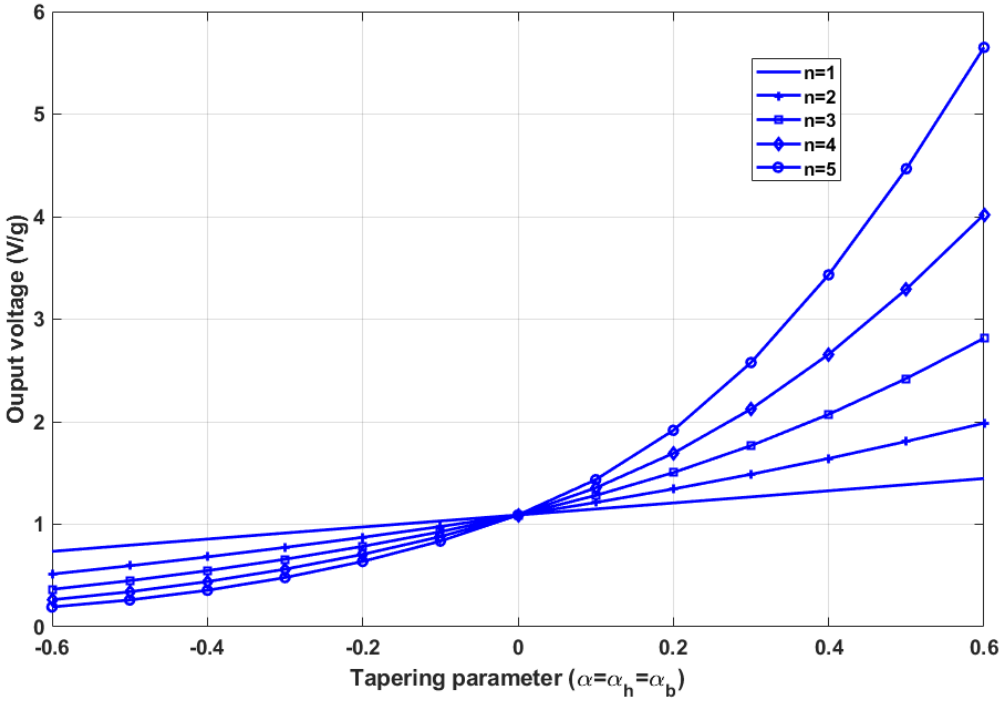

Figure 3.11 Tapering effects on bimorph PEH with parallel connection.

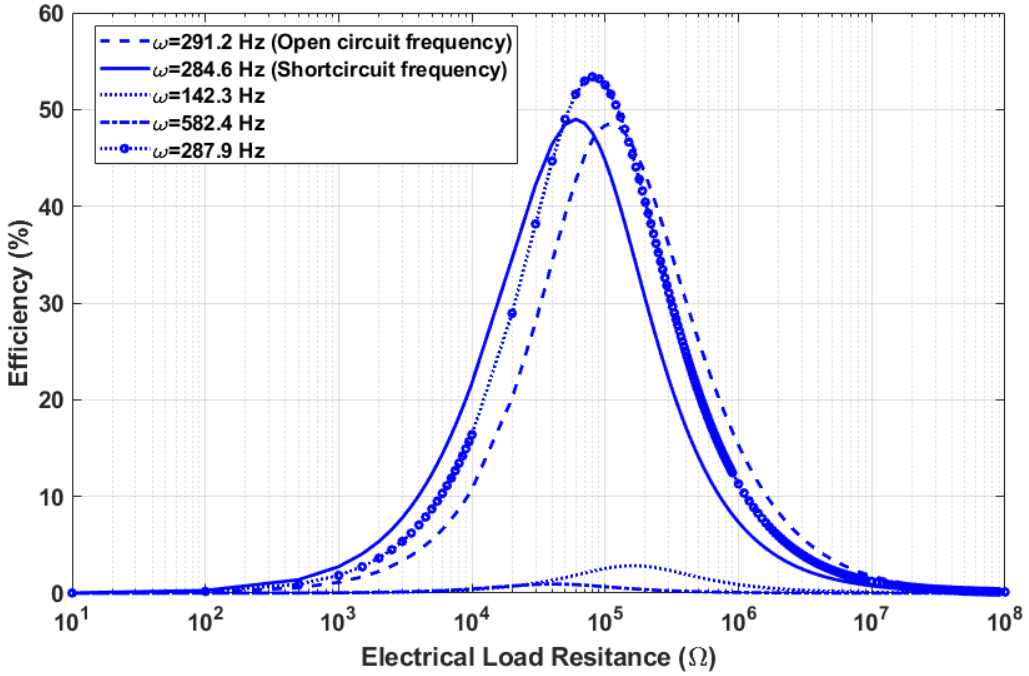

Figure 3.12 Efficiency alteration versus external load resistance at various operating frequencies.

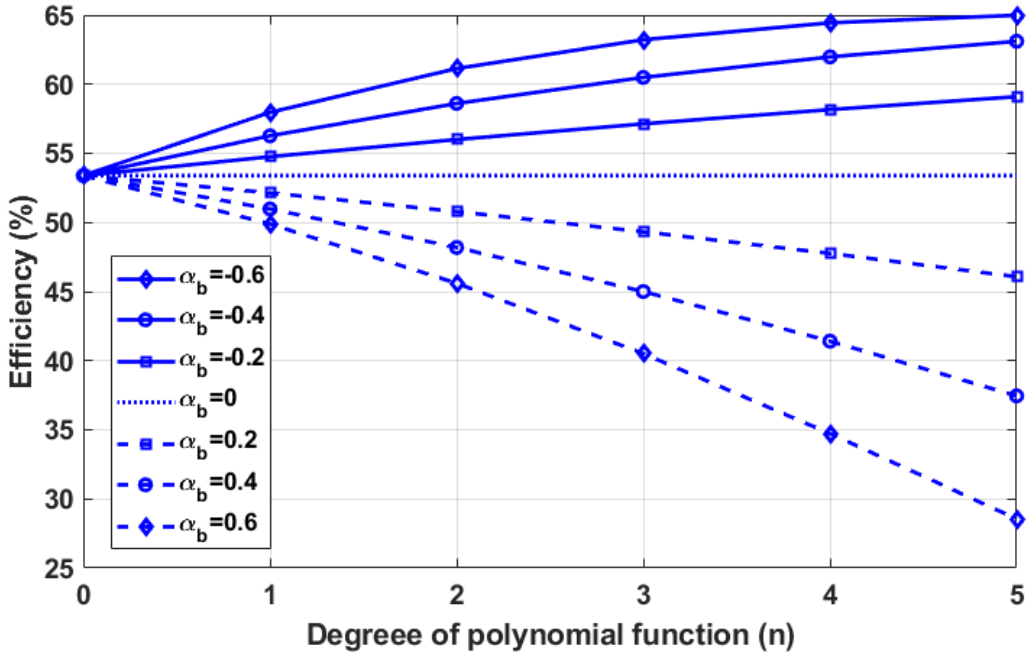

Figure 3.13 Efficiency alteration versus tapering ratio in width direction (α_b).

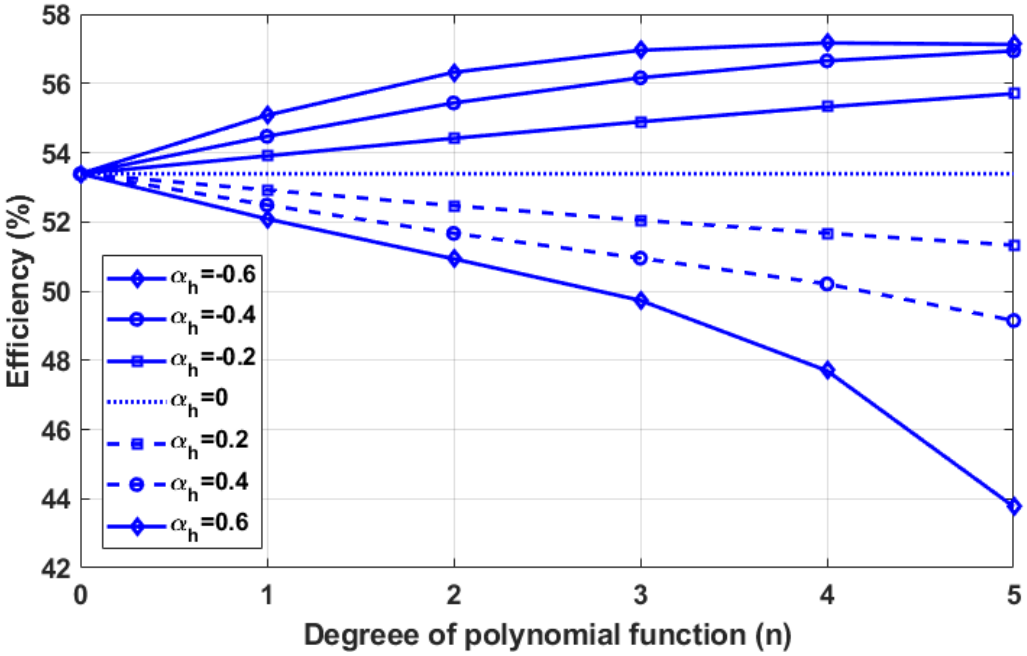

Figure 3.14 Efficiency alteration versus tapering ratio in height direction (α_h).

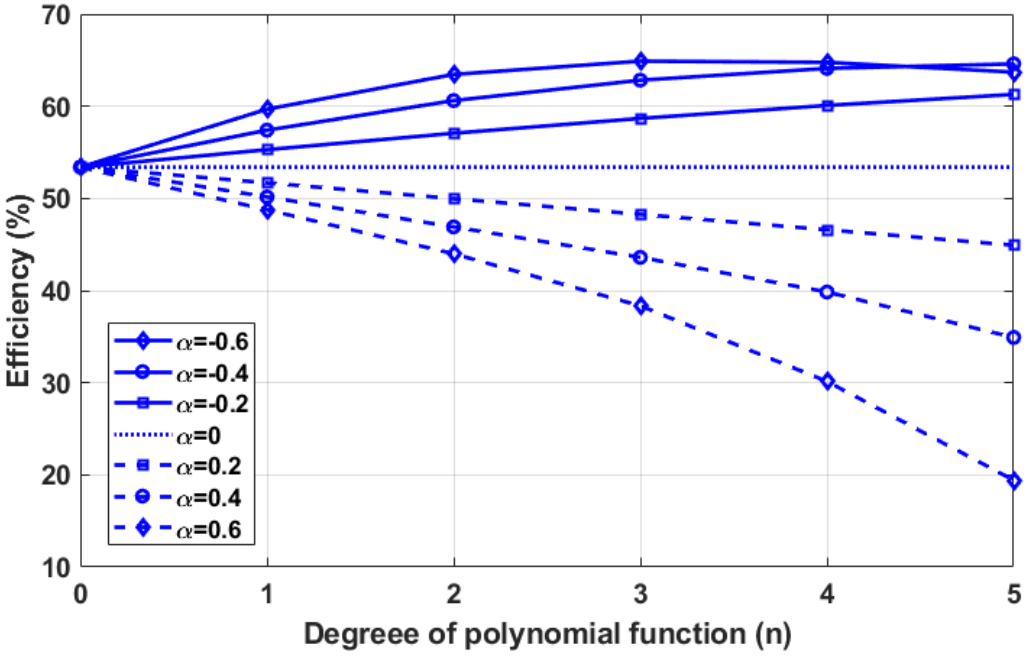

Figure 3.15 Efficiency alteration versus tapering ratio in height and width directions (α).

3.7 Conclusions

In this chapter, a numerical solution for tapered energy harvesting beam with different degrees of non-uniformity and tapering parameter has been presented. Here, two different beam theories including Euler-Bernoulli and Timoshenko have been considered to examine which one can more accurately model the system for different geometrical properties. To calculate the frequency and output voltage of the PEH with elements having 4-DOF and 8-DOF are applied for Euler-Bernoulli and Timoshenko configurations, respectively. The proposed elements are used to calculate the output voltage of unimorph and bimorph with parallel and series connections. Additionally, the efficiency of the above discussed smart structures for various non-uniformity conditions and external load resistance is obtained. Comparing the results with the literature proves the validity of the proposed elements. From the results it is obvious that when the degree of polynomial's function increases the output voltage rises as well so that changing the degree from one to five results in enhancement of electrical voltage by 306%. Additionally, increasing the tapering parameter from the minimum value ($\alpha = -0.6$) to maximum value ($\alpha = 0.6$) leads to increasing the maximum output voltage by 2867.3%. Therefore, it is feasible to improve the output voltage of the PEH by tapering it using polynomial function with higher degrees of non-uniformity. Geometric study demonstrates that for the beams with the small slenderness ratio (< 10) the difference between two above-mentioned theories is noticeable so that it is necessary to employ Timoshenko's formulation rather than Euler-Bernoulli to achieve more accurate results. Eventually, the results indicate that the maximum efficiency is occurring when the value of excitation frequency is ranging between the open-circuit and short-circuit conditions. Tapering ratio and degree of polynomial function have an increasing effect on the efficiency of PEH such that by converging the beam and raising *n* from 1 to 5 the efficiency can be improved by 22%.

Chapter 4 Performance enhancement of cantilever piezoelectric energy harvesters by sizing analysis

This chapter presents the results of the performance of piezoelectric cantilever beams in relation to their size and geometrical configuration. The power produced by cantilever beams which occupy same area and contain same amount of piezoelectric material are analyzed. The total produced power represents the main indicator of performance of a piezoelectric harvesting system while the area of the beams stays constant. Lightweight design is an important aspect in any industry, mainly in the aerospace. In this study, the effects of tapered shape on the efficiency and power output are studied. Finite element method with the application of superconvergent element is adopted here to solve the equations. It is observed that the trapezoidal geometry (converging beam) provides a higher output power while the efficiency decreases. Moreover, in order to prove that the power enhancement is achievable while the amount of piezoelectric material consumed is constant the new configuration is proposed. In the configuration an array of tapered beams connected in series is used instead of one single uniform rectangular beam. The proposed setting generates an output power of 1.817 mW at a resonant frequency of 284.6 Hz when excited by an input acceleration of 1 g. The only challenge is the fundamental frequency difference which is met with the application of thinner substrate and piezoelectric layers.

4.1 Introduction

Energy harvesting is a type of technology wherein the energy is captured from one or more external energy sources to be stored and eventually used for later applications. The subject has attracted considerable attention during the last decade due to the cost-effectiveness and efficiency of the system. The most important feature of power scavengers is their free energy sources usage which is collected from the wasted energy of the ambient surroundings. In comparison to the other common kinds of energy providers such as fossil fuels, they are environmentally-friendly and cost-effective. This rich source of energy is available in most of the industrial plants, machinery, vehicles of all types, and industrial machinery.

Nowadays, the energy scavenged from the harvesters have been known as an alternative source of energy. It has been considered as a support of the electric batteries supplying power for a wide variety of devices such as small wireless sensors and portable and wearable electronics owing to the noticeable advances in wireless technology [5, 7]. In addition to the weight addition and the high cost of maintenance, short life of batteries represents the most important obstacle compared to the long working life of power scavengers. Although there is an opportunity to replace or recharge the batteries, this type of solution is inefficient and sometimes not feasible because of the poor access to their locations. Hence, local recharging from scavenging the free released energy represents a feasible alternative for solving this problem. As a result, power harvesters have been taken into consideration by many researchers as a renewable-power source of portable or wireless devices in different areas [1]. Among the three types of converters including electromagnetic, electrostatic and piezoelectric, piezoelectric converters are advantageous structures with high electromechanical coupling [89]. As an exclusive advantage, they do not need any external voltage source and are a promising choice for the Micro-electromechanical systems (MEMS) application specially wireless sensor nodes [90]. The amount of generated power from these useful structures strongly depends on the different factors including the applied load, the frequency of vibration, the geometric features, and the boundary conditions [10].

Regarding the development of MEMS power generators, fixed or narrow operation frequency range and low power output are the most important challenges [72]. To address the issue, researchers always have been attempting to reach higher performance using different practical methods such as modification of shape, size, material properties and damping [81, 91-94].

Optimization of the active electrode area in order to maximize output is another important strategy illustrated by [95-97]. Another effective method is the application of an array of piezoelectric cantilevers instead of one single beam [98]. It not only covers a higher range of ambient frequencies, but also can help to improve the output power. To prove the efficiency of the strategy, Soliman et al. [99] presented a new architecture for wideband vibration-based micro-power generators (MPGs) with higher bandwidth compared to a traditional MPG. Also, Liu et al. [100] investigated a MEMS power generator array based on thick-film piezoelectric cantilever to improve both output power and frequency bandwidth. These cantilevers are tunable for the desired low frequencies in the 200-400 Hz range. As an optimization method, a new architecture consisting of an array of trapezoidal cantilevers on a circular rim was proposed [101]. They could increase the output power and decrease the natural frequency using the diverging beam and tip mass [2, 91, 102, 103]. The effectiveness of tapered beam configuration can also be seen in other research [11, 81, 104, 105]. Changing the thickness of the substrate layer or mounting a tip mass are two practical methods which have been exploited to change the resonance frequency of the cantilever energy harvesters [72]. Other studies were carried out to improve the output power and decrease the fundamental frequency through the application of a parallel or series array of piezoelectric energy harvesters (PEHs) [98, 106]. Splitting the piezoelectric layer into smaller segments is another strategy which was implemented to change the resonant frequency of a cantilever energy harvester [107]. In order to cover a wide range of excitation frequencies and attain higher output power, a piezoelectric generator was fabricated by multiple circular diaphragm array. [108]. They used four circular diaphragm piezoelectric harvesters with various tip masses which covered the resonance frequencies from 120 Hz to 225 Hz. Additionally, an AIN-based MEMS piezoelectric cantilever array including five piezoelectric cantilever beams and a single proof mass in series connection were presented to increase the output voltage and reduce the loss in a management circuit [109]. Although by the application of series and parallel connections there is possibility to improve the desired electrical output, utilization of more piezoelectric material is unavoidable. As a matter of fact, mass of the piezoelectric part plays an important role in the microfabrication cost of the energy harvesters. In fact, although conventional piezoelectric materials including PZT and PVDF are useful, their fabrication process is time-consuming and expensive. More importantly, they are not environmentally friendly materials. Thus, there is a need to improve the efficiency and electrical output without changing the used amount of piezoelectric material. In this chapter,

the effects of the tapered structure is investigated on the efficiency and power output of PEHS with the scope to figure out which structure provides the maximum efficiency or power. The beam is modeled as Timoshenko beam but it can be easily switched to the Euler-Bernoulli beam with the application of superconvergent element (SCE). Secondly, enhancement power is met with the application of an array of cantilever beams although the same amount of piezoelectric layer is consumed. This new design leads to 15.64% substrate weight reduction, as well. In order to tune the fundamental frequency, the thinner substrate and piezoelectric layers are applied. Overall it is shown by sizing a beam, modelled using the SCE model, it is possible to improve the power produced by the structure without alteration of the operation natural frequency of main system and total structure weight.

4.2 Tapered energy harvester

In this section, the theoretical model of the tapered energy harvester is presented. The cantilever beam has a non-uniform width, b(x), and height, h(x), varying according to the polynomial function, as shown in Fig. 4.1. It is assumed that perfect bonding is performed such that there is no slip between the piezoceramic layers and the substrate layer.

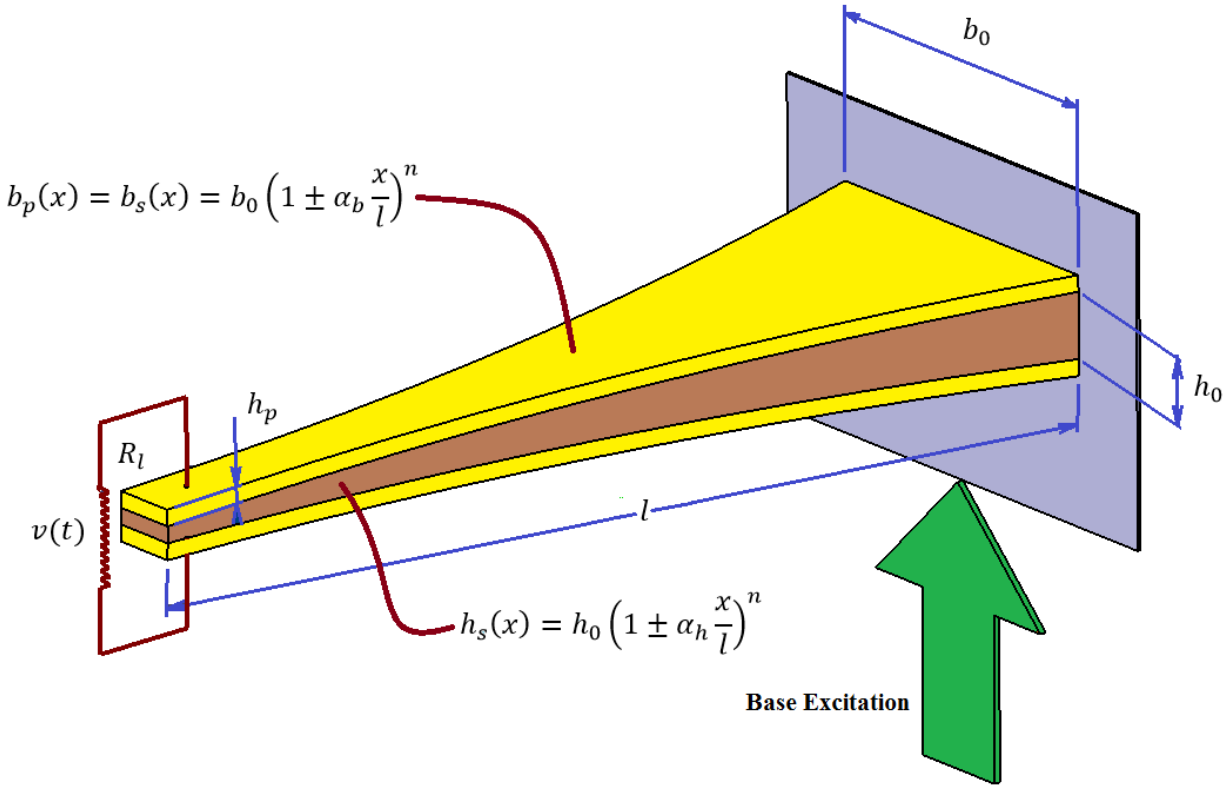

Figure 4.1 A 3D schematic model of piezoelectric based cantilever energy harvester with non-uniform width and height.

4.2.1 Equations of motion for a tapered bimorph PEHs

By the assumption of a Timoshenko beam, the displacement of a generic point can be described by:

$$\boldsymbol{R} = \begin{Bmatrix} R_x \\ R_y \\ R_z \end{Bmatrix} = \begin{Bmatrix} u(x,y,z,t) \\ v(x,y,z,t) \\ w(x,y,z,t) \end{Bmatrix} = \begin{Bmatrix} z\phi_x(x,t) \\ 0 \\ w_0(x,t) + g(t) \end{Bmatrix} \tag{4.1}$$

where w_0 are the displacements projected on the mid-plane, ϕ_x is the rotation of the corresponding cross section at point x and time t relative to the moving base, and $g(t)$ is the transverse translation

coming from the base motion. Using the definition of Lagrange strain tensor and using the non-zero components of the flexible displacement, the normal and shear strains are obtained as

$$\begin{cases} \epsilon_p = \dfrac{\partial u}{\partial x} = z\acute{\phi}_x & \dfrac{h_s}{2} \le z \le \dfrac{h_s}{2} + h_p \\ \epsilon_{xx} = \dfrac{\partial u}{\partial x} = z\acute{\phi}_x & -\dfrac{h_s}{2} \le z \le \dfrac{h_s}{2} \\ \epsilon_p = \dfrac{\partial u}{\partial x} = z\acute{\phi}_x & -\dfrac{h_s}{2} - h_p \le z \le -\dfrac{h_s}{2} \end{cases} \tag{4.2}$$

$$\begin{cases} \gamma_p = \dfrac{\partial u}{\partial z} + \dfrac{\partial w}{\partial x} = \phi_x + \acute{w}_0 & \dfrac{h_s}{2} \le z \le \dfrac{h_s}{2} + h_p \\ \gamma_{xz} = \dfrac{\partial u}{\partial z} + \dfrac{\partial w}{\partial x} = \phi_x + \acute{w}_0 & -\dfrac{h_s}{2} \le z \le \dfrac{h_s}{2} \\ \gamma_p = \dfrac{\partial u}{\partial z} + \dfrac{\partial w}{\partial x} = \phi_x + \acute{w}_0 & -\dfrac{h_s}{2} - h_p \le z \le -\dfrac{h_s}{2} \end{cases} \tag{4.3}$$

With the assumption of linear piezoelectric constitutive equations [53], the calculated piezoelectric constitutive equations are summarized in Eq. 2.7 [3], as.

$$\begin{Bmatrix} \epsilon_p \\ \gamma_p \\ D_3 \end{Bmatrix} = \begin{bmatrix} \dfrac{1}{E_p} & 0 & d_{31} \\ 0 & \dfrac{1}{K_s G_p} & 0 \\ d_{31} & 0 & \varepsilon_{33}^T \end{bmatrix} \begin{Bmatrix} \sigma_p \\ \tau_p \\ E_3 \end{Bmatrix} \tag{2.7}$$

where σ_p is the normal stress, τ_p is the shear stress, ϵ_p is the normal strain, γ_p is the shear strain, G_p is the shear modulus, E_p is the elastic modulus, D_3 is the electric displacement, d_{31} is the piezoelectric strain coefficient, ε_{33}^T is the dielectric permittivity of the piezoelectric layer at constant stress and finally K_s and E_3 are the shear correction factor and the electric field across the piezoelectric layer, respectively.

The next step through the derivation of governing equations is the application of the Hamilton's principle (Eq. 2.21).

$$\int_{t_1}^{t_2} (\delta T - \delta U + \delta W_{IE} + \delta W_{nc}) dt = 0 \tag{2.21}$$

where δT, δU, δW_{IE} and δW_{nc} are the virtual works of the total kinetic energy, the strain energy, the internal electrical energy and the energy corresponding to non-conservative mechanical force, respectively.

The kinetic and strain energies of the entire structure are described using the following equations.

$$\begin{aligned} U &= \frac{1}{2}\int [\sigma_{xx}\epsilon_{xx} + \tau_{xz}\gamma_{xz}] dV_s + \frac{1}{2}\int \left[\sigma_p \epsilon_p + \tau_p \gamma_p\right] dV_p \\ &= \frac{1}{2}\int_0^L \left[I_2^E \acute{\phi}_x{}^2 + I_0^G \left(\acute{w}_0{}^2 + \phi_x{}^2 + 2\phi_x \acute{w}_0\right)\right] dx \\ &\quad + \frac{1}{2}\int_0^L \left[J_2^E \acute{\phi}_x{}^2 + J_0^G \left(\acute{w}_0{}^2 + \phi_x{}^2 + 2\phi_x \acute{w}_0\right) + \frac{d_{31}}{h_p} J_1^E v(t) \acute{\phi}_x\right] dx \end{aligned} \tag{2.13}$$

$$\begin{aligned} T &= \frac{1}{2}\int \rho\left(\dot{\boldsymbol{R}}.\dot{\boldsymbol{R}}\right) dV + \frac{1}{2} M_t [(\dot{w}_0 + \dot{g})|_{x=l}]^2 + \frac{1}{2} I_t \left[\dot{\phi}_x|_{x=l}\right]^2 \\ &= \frac{1}{2}\int_0^L \left[I_0^\rho \dot{w}_0{}^2 + 2I_0^\rho \dot{w}_0 \dot{g} + I_0^\rho \dot{g}^2 + I_2^\rho \dot{\phi}_x{}^2\right] dx \\ &\quad + \frac{1}{2}\int_0^L \left[J_0^\rho \dot{w}_0{}^2 + 2J_0^\rho \dot{w}_0 \dot{g} + J_0^\rho \dot{g}^2 + J_2^\rho \dot{\phi}_x{}^2\right] dx \\ &\quad + \frac{1}{2} M_t [(\dot{w}_0 + \dot{g})|_{x=l}]^2 + \frac{1}{2} I_t \left[\dot{\phi}_x|_{x=l}\right]^2 \end{aligned} \tag{4.4}$$

where M_t and I_t are the tip mass and its associated moment of inertia. Other coefficients are also defined as follows

$$I_i^E \triangleq \iint z^i E_s dy dz\,, \quad I_0^G \triangleq \iint K_s z^i G_s dy dz\,, \quad I_i^\rho \triangleq \iint z^i \rho_s dy dz\,, i = 0,1,2 \tag{2.15}$$

$$J_i^E \triangleq \iint z^i E_p dydz\ ,\ \ J_0^G \triangleq \iint K_s z^i G_p dydz\ ,\ \ J_i^\rho \triangleq \iint z^i \rho_p dydz\,, i = 0,1,2 \tag{2.16}$$

Additionally, the internal electrical energy in the piezoelectric layer can be calculated as follows

$$\begin{aligned} \mathrm{W}_{IE} &= \frac{1}{2}\int E_3 D_3\, dV_p = -\frac{1}{2}\frac{v(t)}{h_p}\int \left[E_p d_{31}\left(z\acute{\phi}_x\right) - \frac{v(t)}{h_p}\varepsilon_{33}^S\right] dV_p \\ &= -\frac{1}{2}\frac{v(t)}{h_p} d_{31}\int_0^L J_1^E \acute{\phi}_x dx + \frac{1}{2}C_p v(t)^2 \end{aligned} \tag{4.5}$$

where C_p is the internal capacitance of the piezoceramic defined by Eq. 2.18:

$$C_p = \varepsilon_{33}^S \frac{A_p}{h_p} \tag{2.18}$$

where ε_{33}^S is the dielectric permittivity at constant strain and A_p is the electrode area.

In the above equations, dots and prime symbols identify derivatives with respect to time and space (i.e.. x), respectively. The only non-conservative virtual work is owing to the electric charge output $Q_u(t)$ which is defined in Eq. 2.22

$$\delta W_{nc} = Q(t)\delta v(t) \tag{2.22}$$

To complete the modeling, the effects of damping should be taken into consideration. In this study, the proportional damping (Rayleigh damping) is applied [65].

Regarding the connection of top and bottom piezoelectric layers, there are two different configurations named parallel and series schemes [3]. The relationships between the characteristics of the piezoceramic layers including voltages, charges and piezoelectric strain coefficients specify the type of scheme.

4.2.2 Discretization of equations using superconvergent element (SCE)

The final step is discretization of the coupled model. Finite element model (FEM) with the application of superconvergent element is employed here. This type of element contains two nodes and four degrees-of-freedom (DOF) which include two DOF in the transverse direction and two DOF in the rotational direction (Fig. 2.2). The element provides the precise response with the minimum number of elements since the shape functions are derived by using static equilibrium (Appendix C). One of the most important advantages of this practical element is the simple transferring method. In fact, it is possible to switch readily from the Timoshenko to the Euler-Bernoulli by changing the value of one coefficient (β). Hence, analysis based on both beam theories can be carried out without performing extra calculations [52]. Using the calculated shape functions available in Appendix C, the displacement parameters in terms of the nodal displacements are represented in Eq. (4.6).

$$\begin{bmatrix} w_0(x,t) \\ \phi_x(x,t) \end{bmatrix} = \begin{bmatrix} N_w(x) \\ N_\phi(x) \end{bmatrix} a(t) = \begin{bmatrix} \psi_1^e(x) & \psi_2^e(x) & \psi_3^e(x) & \psi_4^e(x) \\ \varphi_1^e(x) & \varphi_2^e(x) & \varphi_3^e(x) & \varphi_4^e(x) \end{bmatrix} \begin{bmatrix} W_1^e(t) \\ \phi_1^e(t) \\ W_2^e(t) \\ \phi_2^e(t) \end{bmatrix} \tag{4.6}$$

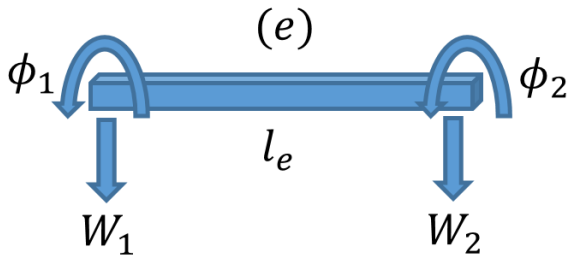

Figure 2.2 Two-node finite element with four DOF.

where $N_w(x)$ and $N_\phi(x)$ are the shape functions and $a(t)$ is the unknown generalized coordinates. By substitution of Eq. (4.6) into Eq. (2.21) and by performing integration by parts, the electromechanical coupling equations for a typical finite element result in Eqs. (2.25) and (2.27). Addition of the Rayleigh damping accounting for the mechanical dissipative effects is the last stage of modelling (Eq. (2.28)).

$$\boldsymbol{M^e\ddot{a}(t) + C^e\dot{a}(t) + K^e a(t) - \theta^e v(t) = f^e} \tag{2.25}$$

$$\overline{C_p}\dot{v}(t) + \frac{v(t)}{R_l} + \boldsymbol{\theta^{eT}\dot{a}(t)} = 0 \tag{2.27}$$

$$\boldsymbol{C^e} = \mu\boldsymbol{M^e} + \gamma\boldsymbol{K^e} \tag{2.28}$$

where μ and γ are the constants of mass and stiffness proportionality. Terms $\boldsymbol{M^e}$, $\boldsymbol{C^e}$, $\boldsymbol{K^e}$, $\boldsymbol{\theta^e}$, $\boldsymbol{f^e}$ are, respectively, the mass matrix; the damping matrix; the elastic stiffness matrix; the electromechanical coupling matrix and the vector of dynamical forces corresponding to one element of the piezoelectric cantilever beam, and $\overline{C_p}$ is the equivalent capacitance (Appendix E).

4.2.3 Solution of the electromechanical coupling equations

By the assumption of the input in the harmonic form, $(t) = Xe^{i\omega t}$, and assembling the elements of the cantilever energy harvester the components of the forcing vector become:

$$\boldsymbol{f^e} = \left[\omega^2 X \int_0^{l_e} \left(I_0^\rho + J_0^\rho\right) {N_w}^T dx\right] e^{i\omega t} \tag{2.29}$$

The assembled steady-state forms of electromechanical coupling equations can be achieved as Eqs. 2.30 and 2.31 by the definition of the steady-state response and the voltage output. These two parameters are considered $\boldsymbol{a(t)} = \boldsymbol{A}e^{i\omega t}$ and $v = Ve^{i\omega t}$, respectively.

$$(-\boldsymbol{M}\omega^2 + i\omega\boldsymbol{C} + \boldsymbol{K})\boldsymbol{A} - \boldsymbol{\theta}V = \boldsymbol{F} \tag{2.30}$$

$$i\omega\boldsymbol{\theta^T A} + \left(i\omega\overline{C_p} + \frac{1}{R_l}\right)V = 0 \tag{2.31}$$

After solving the above equations, the complex voltage is obtained as

$$v(t) = -i\omega\left(i\omega\overline{C_p} + \frac{1}{R_l}\right)^{-1}\boldsymbol{\theta^T}\left[-\boldsymbol{M}\omega^2 + i\omega\boldsymbol{C} + \boldsymbol{K} + i\omega\left(i\omega\overline{C_p} + \frac{1}{R_l}\right)^{-1}\boldsymbol{\theta\theta^T}\right]^{-1}\boldsymbol{F}e^{i\omega t} \tag{2.34}$$

4.3 Expressions of power density and efficiency

To compare the performance of different systems and structures it is necessary to define one type of measurements. Regarding the piezoelectric energy harvesters, electrical output power extracted from the structure is one kind of calculation which has been widely used. Although this is a practical measurement, it cannot provide a precise and correct evaluation because the value strongly depends on the size, vibration environment and circuit conditions [87]. In fact, application of a larger beam can result in higher output power. For the comparison of two different configurations the mechanical input power is one important factor which should not be neglected. In this regard, there are other measurement parameters including the power density (output power divided by the piezoelectric layer volume) and efficiency which have been of primary interest. In this chapter, both parameters are taken into consideration for the comparison target and their results are analyzed and compared.

Efficiency specifies the amount of the input mechanical energy (P_{in}) which can be converted into the output electrical power (P_{out}) (Eq. 3.6).

$$\Gamma = \frac{P_{out}}{P_{in}} \tag{3.6}$$

where P_{in} is the energy coming from the shaker which creates the excitation. Thus, the amount of input energy can be written as [86]

$$P_{in} = \boldsymbol{f^e}\dot{\boldsymbol{a}}(\boldsymbol{t}) \tag{3.7}$$

By having the input and output energies, the harvesting efficiency is defined as

$$\Gamma = \left|\frac{\boldsymbol{v(t)I(t)}}{\boldsymbol{f^e\dot{a}(t)}}\right|$$

$$= \left|\frac{\left[-i\omega\left(i\omega\overline{C_p}+\frac{1}{R_l}\right)^{-1}\boldsymbol{\theta^T}\left[-\boldsymbol{M}\omega^2+i\omega\boldsymbol{C}+\boldsymbol{K}+i\omega\left(i\omega\overline{C_p}+\frac{1}{R_l}\right)^{-1}\boldsymbol{\theta\theta^T}\right]^{-1}\right]^2\boldsymbol{F^2}}{i\left[-\boldsymbol{M}\omega^2+i\omega\boldsymbol{C}+\boldsymbol{K}+i\omega\left(i\omega\overline{C_p}+\frac{1}{R_l}\right)^{-1}\boldsymbol{\theta\theta^T}\right]^{-1}R_l\boldsymbol{F^2}\omega}\right| \quad (3.8)$$

4.4 Results and discussion

Before the parametric study of the energy harvester is carried out, there is a need to validate the numerical solution. To satisfy the requirement, the output voltage and fundamental frequency of uniform and non-uniform beams are firstly compared with those available in literature. After that, the influence of non-uniformity on both the power and efficiency are studied to figure out which configuration (converging or diverging beams) can result in the maximum desired measurement parameters. Finally, the application of an array of PEHs (Fig. 4.2) instead of having one single cantilever energy harvester is proposed as the array has the capability to harvest more power.

In the first example, the convergence of the superconvergent element is verified by considering a bimorph cantilever beam investigated by Erturk and Inman [3] for both with and without the tip mass. The properties of the investigated bimorph piezoelectric beam which are connected in series are summarized in Table 2.1.

Table 2.1 Properties of the bimorph piezoelectric cantilever beam.

Property	Piezoelectric layer	Substrate layer
Material	PZT-5H	Brass
Density ρ (kg/m^3)	7500	9000
Length (mm)	24.53	24.53
Thickness (mm)	0.265	0.14
Width (mm)	6.4	6.4
Young's modulus E (GPa)	60.6	105
Piezoelectric strain coefficient d_{31}(pC/N)	-274	–
Dielectric permittivity at constant strain ε_{33}^{S} (nF/m)	25.55e3	–
Shear modulus G (GPa)	23	40

To be able to compare and validate the results the short-circuit and open-circuit conditions are considered as $R_l = 470\ \Omega$ and $R_l = 995\ k\Omega$, respectively. In fact, these values are in agreement with the ones proposed in the open literature [3]. The fundamental resonance frequency of the PEH based on the Timoshenko beam theory for two types of considerations are provided in Tables 4.1-4.2.

Table 4.1 Fundamental resonance frequency of piezoelectric energy harvester without tip mass.

1st natural frequency	Experimental (Hz) [3]	SCE (Hz)	RD (%)
Short circuit, ($R_l = 470\ \Omega$)	502.5	504.7	0.44
Open circuit, ($R_l = 995\ k\Omega$)	524.7	526.9	0.42

Table 4.2 Fundamental resonance frequency of piezoelectric energy harvester with tip mass (0.239g).

1st natural frequency	Experimental (Hz) [3]	SCE (Hz)	RD (%)
Short circuit, ($R_l = 470\ \Omega$)	338.4	338.7	0.089
Open circuit, ($R_l = 995\ k\Omega$)	356.3	355.6	0.2

The excellent convergence rate of SCE is obvious from the results in which using only one superconvergent element the difference between the experimental and theoretical values for both conditions is negligible (less than 0.5%). Hence, the represented SCE has a very good rate of convergence for the study of piezoelectric energy harvesters.

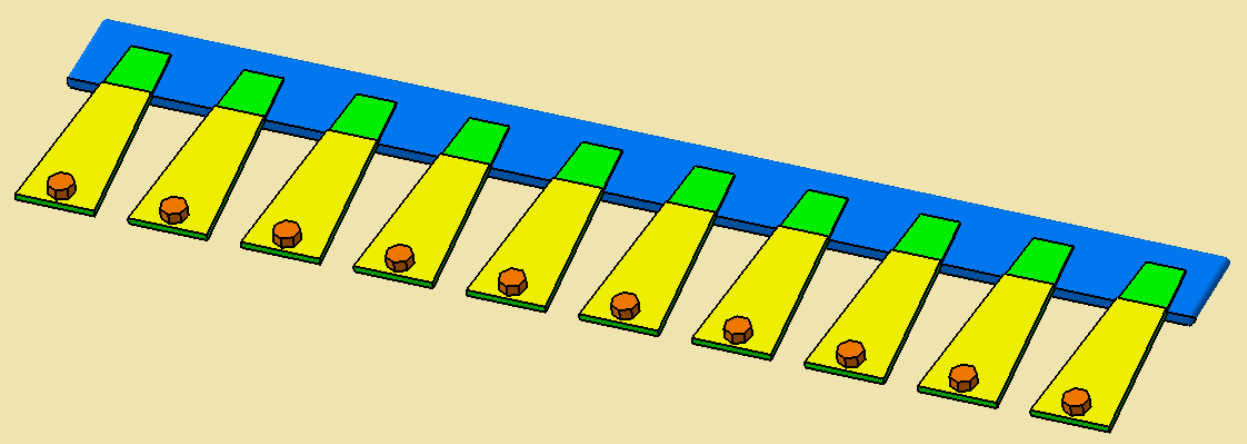

Figure 4.2 A 3D simulated structure of an array of diverging bimorph PEHs

As the second part of validation, the output voltage of one non-uniform PEH is compared with the literature [72]. They assumed that the width of the beam is varying exponentially through the length by $b(x) = b_0 e^{-cx}$. The properties of studied PEH are listed in Table 3.1. The output voltage for five different tapering parameters are calculated and provided in Table 4.3. The electrical resistance and damping ratio are taken 1000 Ω and 1 percent, respectively.

Table 3.1 Properties of the bimorph piezoelectric cantilever beam.

Property	Piezoelectric layer	Substrate layer
Material	PZT-4	Steel
Density ρ (kg/mm^3)	7960	7800
Length (mm)	60	60
Thickness (mm)	0.6	0.7
Initial width b_0(mm)	10	10
Young's modulus E (GPa)	81.3	200
Piezoelectric strain coefficient d_{31}(pC/N)	-123	–
Dielectric permittivity at constant strain ε_{33}^{S} (nF/m)	13.059	–
Shear modulus G (GPa)	31.3	76.9

Table 4.3 Validation of piezoelectric energy harvester's voltage for different tapering values.

c	0	5	10	15	20
Analytical (V/g) [72]	0.6252	0.5479	0.4802	0.4214	0.3704
SCE element (V/g)	0.6252	0.5470	0.4800	0.4225	0.3729
RD (%)	**0**	**0.16**	**0.042**	**0.26**	**0.67**

It can be concluded again that SCE has a great rate of convergence so that with the application of only one SCE the relative error between the numerical and analytical results is less than 0.7 percent.

In the next example, the effects of tapering ratio on the power density and efficiency of the PEH is analyzed. The energy harvester has the same properties as described in the previous example. To optimize the system, the effects of tapering ratio (α) and the degree of polynomial function are investigated and depicted in Figs. 4.3-4.6. The results show that by increasing the tapering ratio (application of diverging beam) the power output increases while the efficiency decreases. Obviously, increasing the content of piezoelectric material enables the increasing pattern of the output power. The input absorbed energy from the environment will yield more power at the cost of reduced efficiency for the diverging beams. In other words, for the diverging beam the amount of input absorbed energy is higher in comparison to converging structure, leading to smaller efficiency. Additionally, by the comparison of graphs associated with α_b and α_h

illustrated in Figs. 4.3-4.6 it is concluded that the effects of tapering ratio in width direction (α_b) yields more power output and higher efficiency. It is necessary to point out that the variation of efficiency and the power output are investigated here for the fixed value of load resistance providing small values. In order to maximize the parameters the value of external load resistance should be optimized as well [3].

To study the influence of tapered beam on the performance, the variation of power FRF curves for both tapering parameters is shown separately in Figs. 4.7-4.8. It can be found that the peak voltage of power significantly increases by 2038% while the tapering ratio changes from $\alpha_b = -0.6$ to $\alpha_b = 0.6$. Although the power output escalates, the fundamental natural frequency decreases significantly. As the tapering parameter varies from 0.6 for diverging beam to -0.6 for converging beam, the resonance frequency increases by 522% from 147.58 Hz to 917.81 Hz. Consequently, we get variation in frequency range and the peak of output power when α_h is changing but the changes are not as dramatic as the α_b case. The degree of polynomial function is another determining parameter for the output power as the influence is depicted in Fig. 10. The power output is increased by 1744.5% for tapered beam with n=5 with respect to uniform beam for which $\alpha_b = \alpha_h = 0$. The enhancement of electrical output is due to increasing the surface of the structure. In fact, since the piezoelectric layer is the part contributing to the generation of power output, increasing the polynomial degree results into the expansion of the surface of cantilever beam covered by the piezoelectric material and exposed to strain. This will be resulting in higher electrical output. Thus, the above analysis and investigation shows while the power output increases for the diverging beam the frequency reduces.

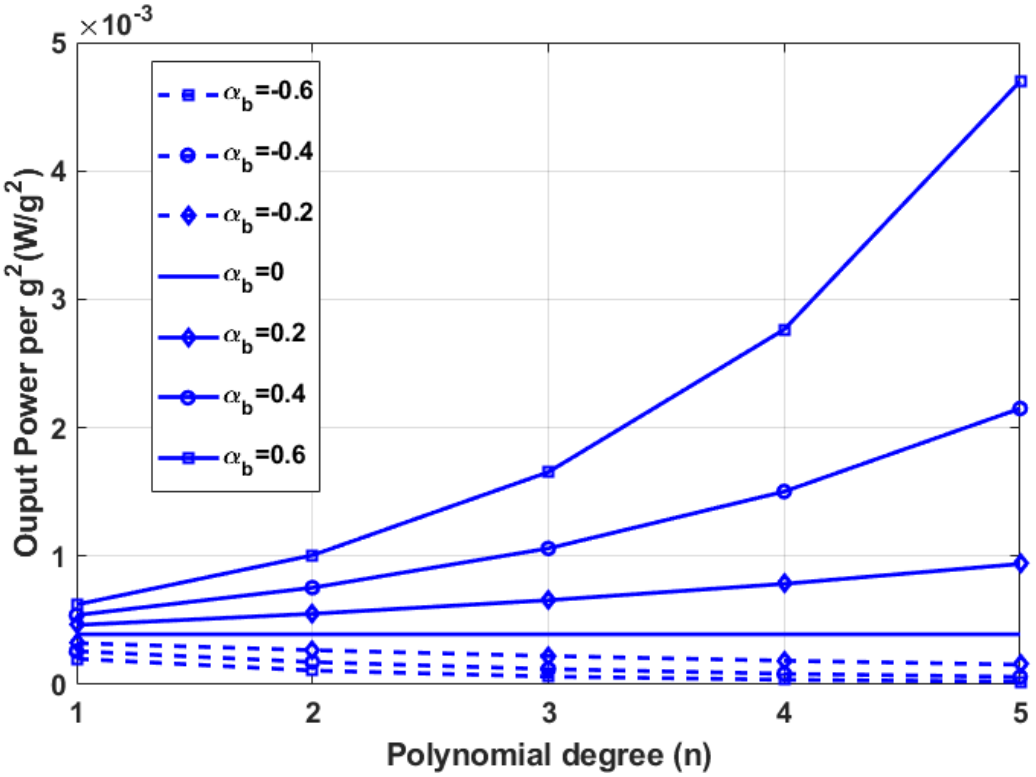

Figure 4.3 Power output variation versus polynomial degree under different width taper ratios (α_b).

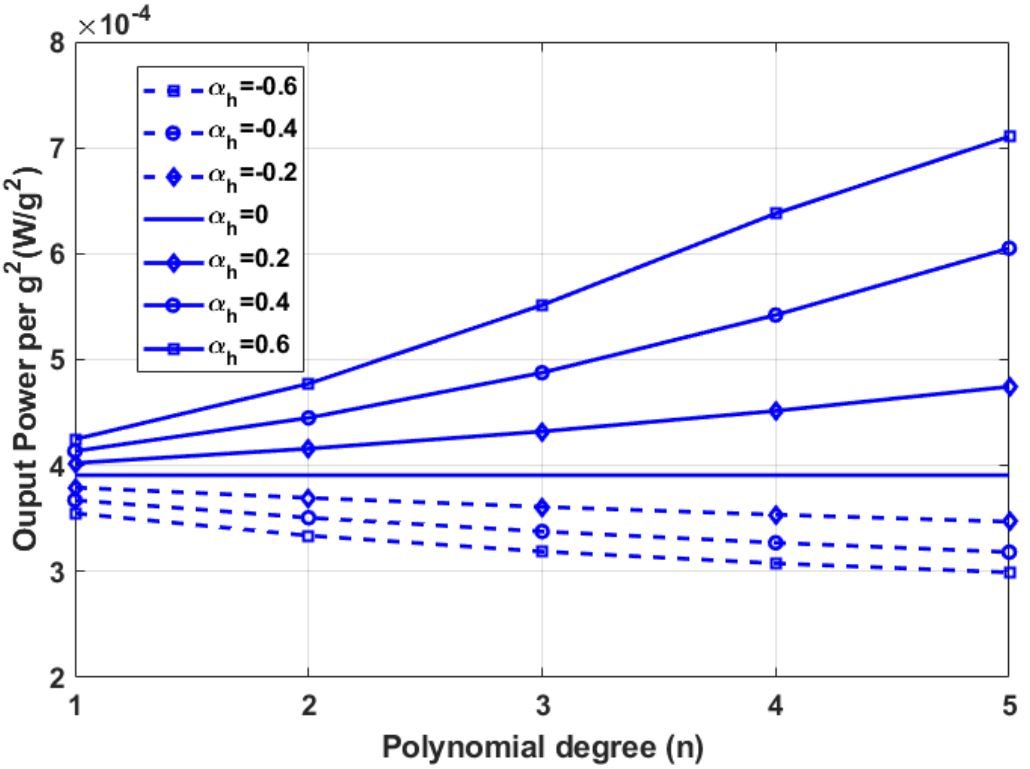

Figure 4.4 Power output variation versus polynomial degree under different height taper ratios (α_h).

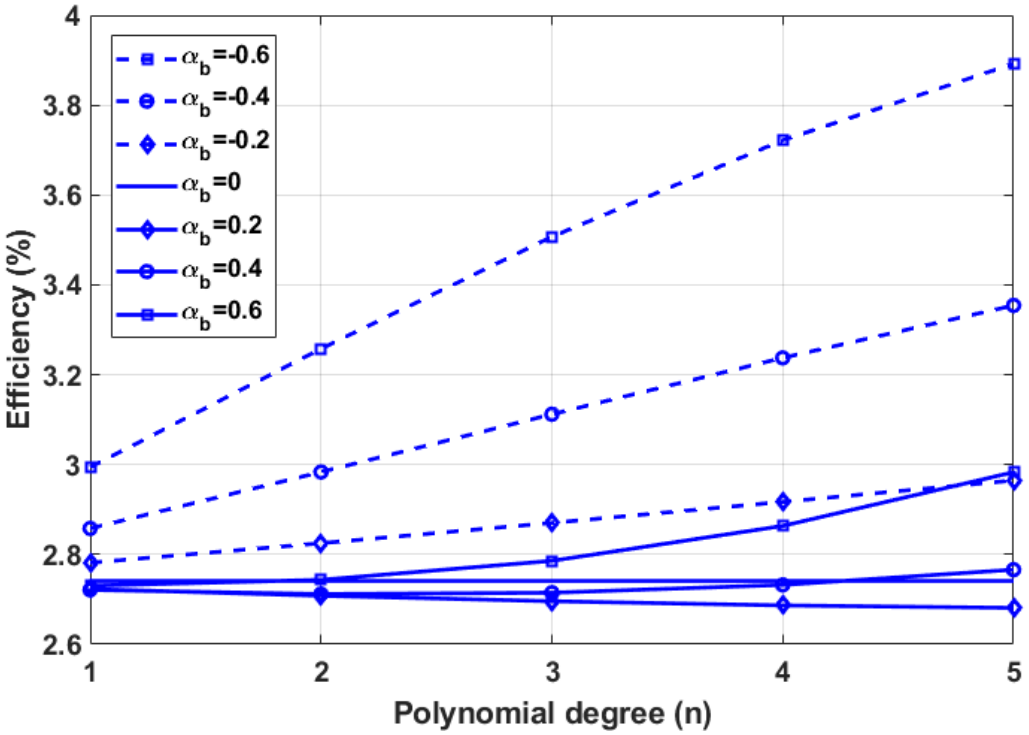

Figure 4.5 Efficiency variation versus polynomial degree under different width taper ratios (α_b).

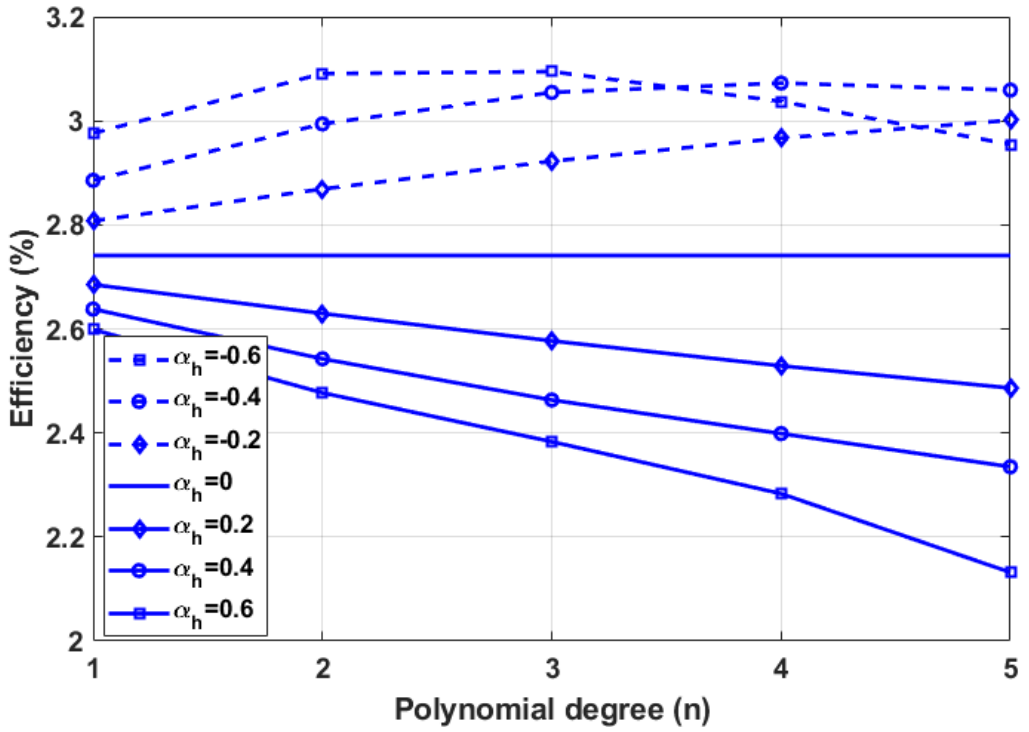

Figure 4.6 Efficiency variation versus polynomial degree under different height taper ratios (α_h).

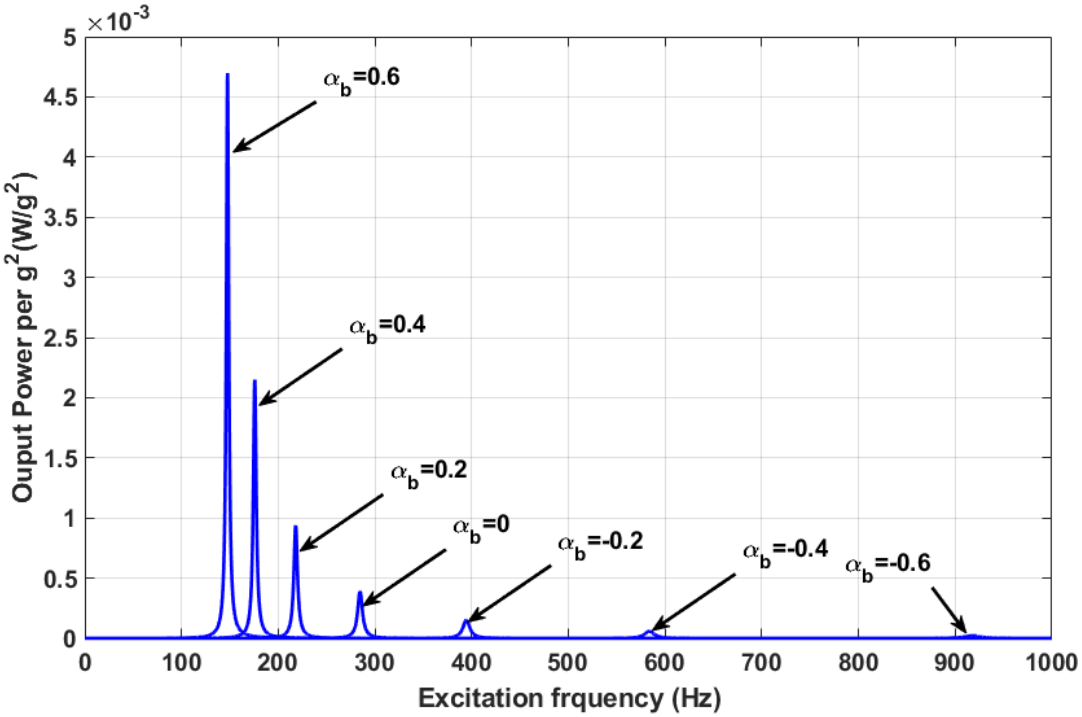

Figure 4.7 A power FRF curves for quintic tapered beam in width direction.

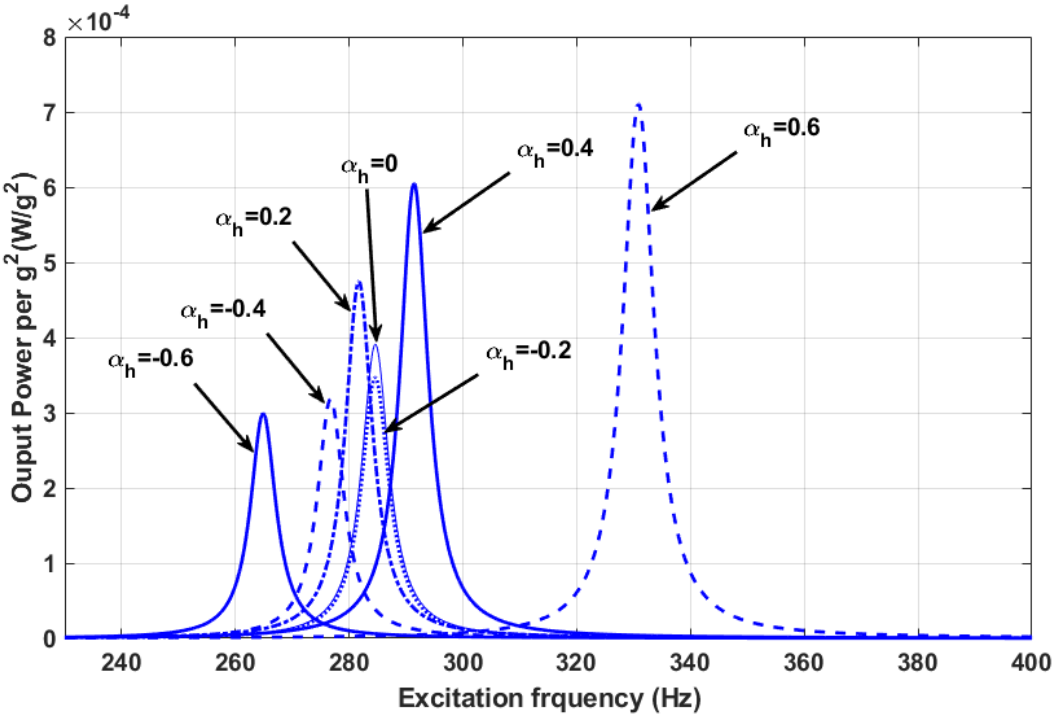

Figure 4.8 A power FRF curves for quintic tapered beam in height directions.

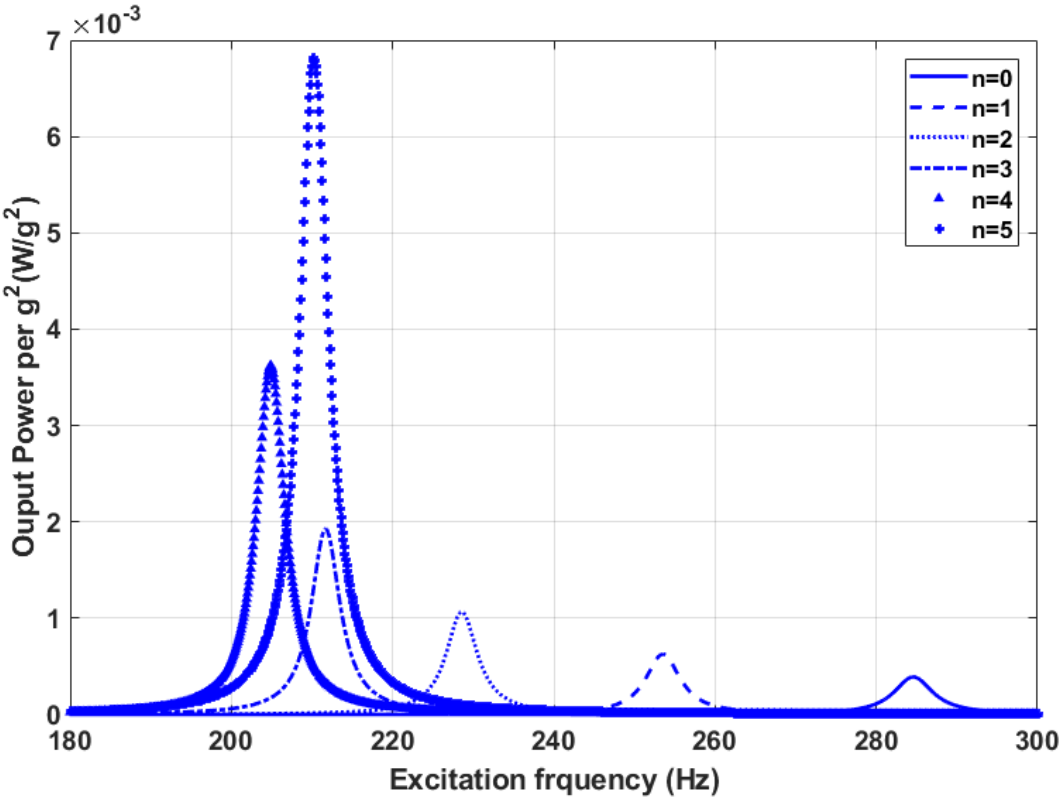

Figure 4.9 A power FRF curves for tapered beam ($\alpha_b = \alpha_h = 0.5$) of different polynomial degrees.

In the next example the amount of power output per volume of piezoelectric layers is investigated using the application of an array of PEHs instead of having one single beam. The properties of the PEHs are the same as in previous examples. Since the effects of sizing is important the ratio of length over width of the beam is kept constant for comparison. Application of smaller beams will result in the increased fundamental frequency. This frequency difference for the beams with the smaller size should be surmounted since the target is maximization of output power without the change of operation frequency. Application of tip mass has been one of the simplest and most useful methods used to tune the frequency. Selection of an appropriate tip mass could change the mass of system to meet the desirable natural frequency. The tip mass attached to the tip of the cantilever PEH such that the center line of the cube is at the tip of the beam [3]. The variation of power for different arrays of beams with the same volume is shown in Figs. 4.10-4.11. By analyzing the results, it can be concluded that the application of smaller cantilever beams and tip masses (for the frequency tuning) provides the possibility to increase the power noticeably. Decreasing the size of the beams resulted in increasing the output power. For example, by the

application of 25 beams connecting in series the corresponding power increases by 958% with respect to that of the uniform beam although the operation frequency remains constant, around 284.6 Hz which was considered for validation purposes. Here series connection is considered since it can render higher extracted output power and voltage in comparison to the parallel connection [109]. Although the smaller size has an increasing effect on the power output the amount of required tip mass for the beam with this small size is not feasible. In fact, this tiny beam cannot withstand the $M_t = 47.7\ g$. Moreover, addition of this amount of mass to the structure will result in escalating the total mass. Thus, the modification should be made to decrease the amount of required proof mass or even remove it entirely. To satisfy the requirement application of thinner beam method is employed.

Reducing the thickness of piezoelectric and substrate layers is the desired method considered here. From Fig. 4.7 it appears that increasing the tapering ratio not only results in the reduction of resonance frequency, but also amplification of the electrical power output. This kind of useful feature is used to remove the tip mass completely. The new structure consists of an array of tapered beams ($\alpha_b = 0.6\,, \alpha_h = 0\,, \mathrm{n} = 5$). The thickness of the piezoelectric and substrate layers are considered to be the same, as well. In order to find a suitable value for the thickness its effect on the natural frequency should be firstly analyzed. This analysis is necessary to figure out for which thickness one can reach the desired resonant frequency of 284.6 Hz. The effect of increasing thickness for the array of beams is shown in Fig. 4.12. The active/passive layer thickness is varied from 0.1 mm to 0.5 mm. As it was expected the graphs show that there is a linear relationship between the frequency and the thickness. Hence, for every array of the beams with specific size there is an optimal thickness value. The comparison of power FRFs per unit mass of piezoelectric layers between the original rectangular beam and the modified tapered beams is represented in Fig. 4.13. The results show that the new designed systems are capable of scavenging more power but the fundamental natural frequency is the same for all structures. The overlapping of the curves indicate that the analyzed configurations provide the same amount of power. The produced output power per unit mass is 88.32 mW/kg under 1.0 g which is 29.5% higher with respect to the one provided by a single uniform beam. Although the structure harvests more energy there is still room to increase the output by the change of length-to-width ratio.

As the last step, the effects of ratio of the length over the width of the tapered beam ($\alpha_b = 0.6\,, \alpha_h = 0\,, \mathrm{n} = 5$) is investigated to find the optimum value. As is obvious from Fig. 4.14,

decreasing the ratio can result in increasing the maximum output power of the system. It is worth mentioning that the resonant frequency is kept the same for all ratios. By reducing the ratio from 12 to 3 there is a possibility to enhance the output power by 267%. It is noticeable that the width at the free end of the beam is the limiting factor. In other words, since the converging tapered beam is considered the ratio should be a feasible value in order to achieve an acceptable structure. The comparison of power FRFs per mass of the piezoelectric material between the primary uniform beam and the new designed tapered ones with different lengths over width ratios is calculated and represented in Fig. 4.15. As the completing part, a performance comparison between an array of 14 tapered bimorph cantilever beams with the geometry: $\alpha_b = 0.6$, $\alpha_h = 0$, n = 5 , $l = 15\text{mm}$, $b_0 = 5\text{mm}$, $h_p = h_s = 0.077\text{mm}$ and the primary uniform cantilever beam is analyzed and shown in Fig. 4.16. The curves reveal that the output power dramatically increases from 0.391 mW to 0.940 mW (140% more power). In this enhanced design not only the amount of piezoelectric material consumed is constant, but the mass of the substrate layer is reduced by 15.64%.

By and large, it has been shown that by the adoption of sizing analysis and application of an array of beams in series connection instead of one single beam one can noticeably improve the power output of the system. It should be pointed out that the amount of used active material and fundamental natural frequency remain constant for the comparison. To offset the tip mass concern the thinner layers can be used but the acceptable amount of thickness reduction depends on the fabrication limitation and the stability of the structure. In other words, it is not possible to decrease the thickness more below the limit of buckling or to the level that the beam could wrinkle. Another practical way which can help in the tuning target is the application of substrate layer with lower modulus of elasticity resulting in lower natural frequencies. This is for further analysis which can be considered to achieve more power output with less amount of required tip mass. Paper-based piezoelectric structures are among the potential structures which can be used to satisfy the requirements [110]. In other words, these advantages can be adopted to not only improve the output power, but also keep the fundamental frequency small is the application of paper-based piezoelectric structures. Although the new designed PPEHs have the electrical properties in the same range of conventional piezoelectric materials (PVDF and PZT), their mechanical properties such as modulus of elasticity is much smaller resulting in lower natural frequency. The fabrication procedure of these kinds of piezoelectric materials is explained in Appendix F.

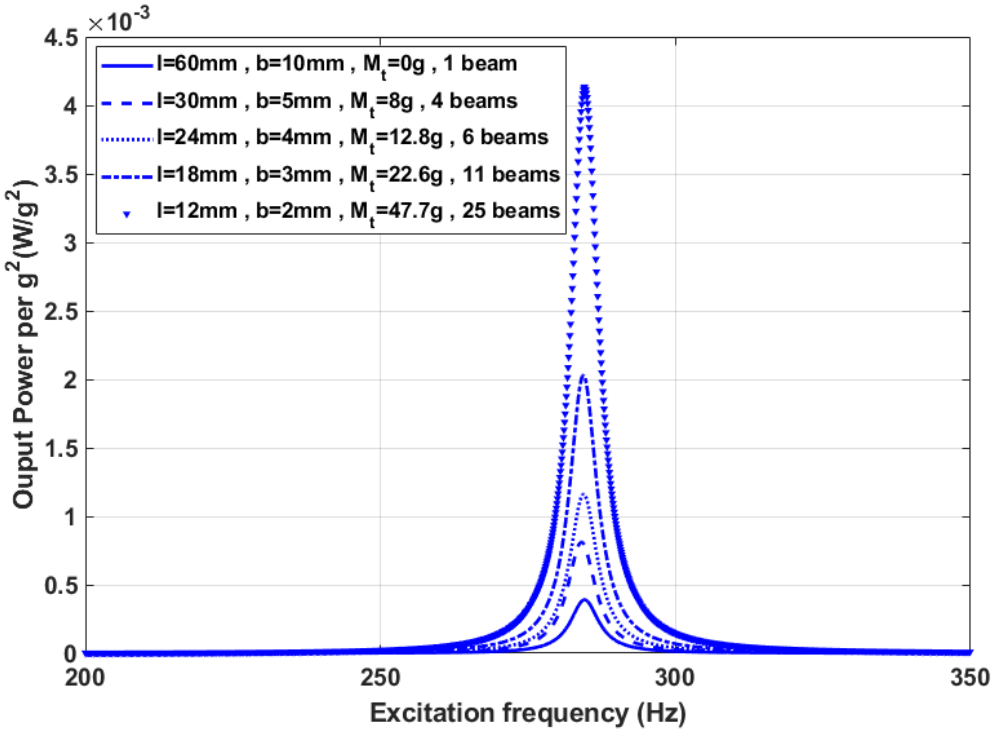

Figure 4.10 Comparison of power FRFs between one uniform beam and an array of multiple uniform beams.

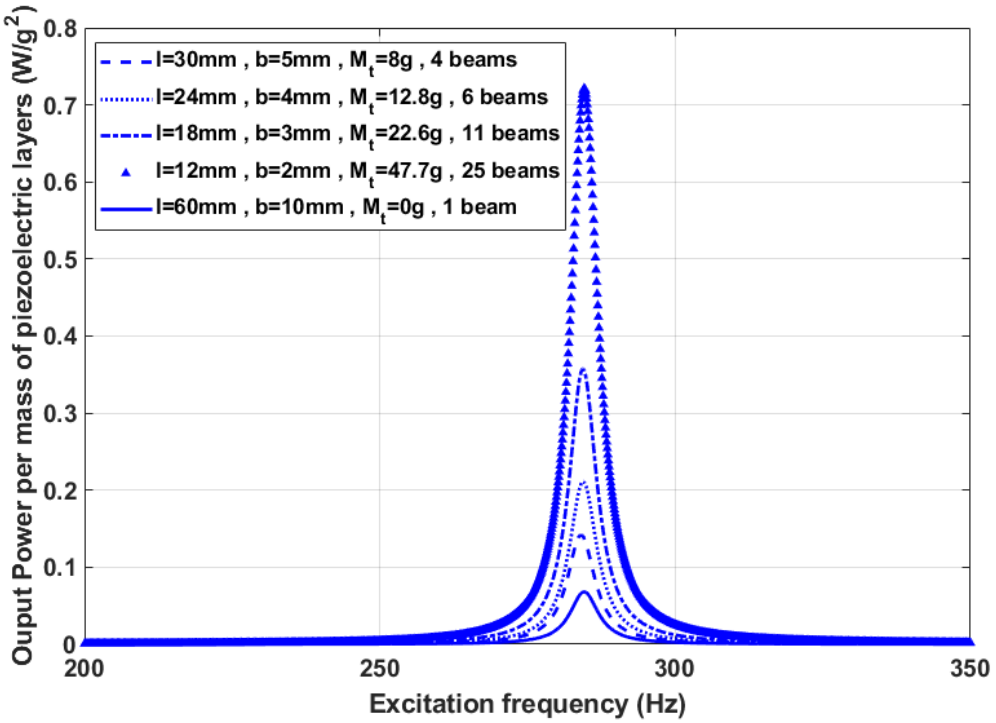

Figure 4.11 Comparison of power FRFs per piezoelectric mass between different beam sizes.

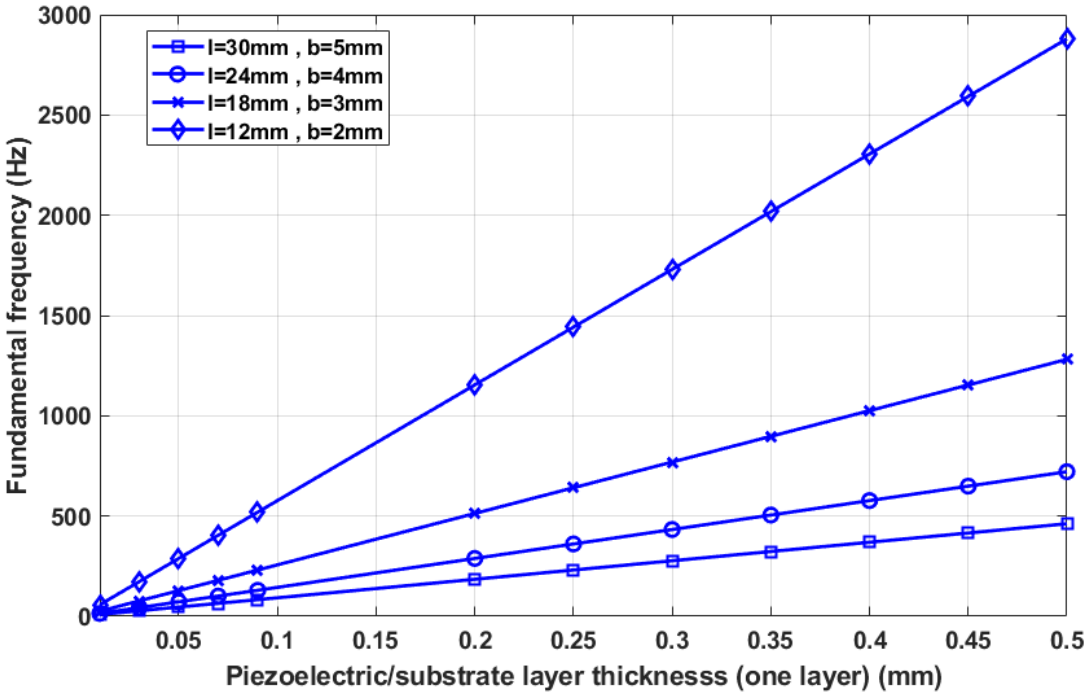

Figure 4.12 Fundamental frequency as a function of piezoelectric/substrate layer thickness ($h_p = h_s$).

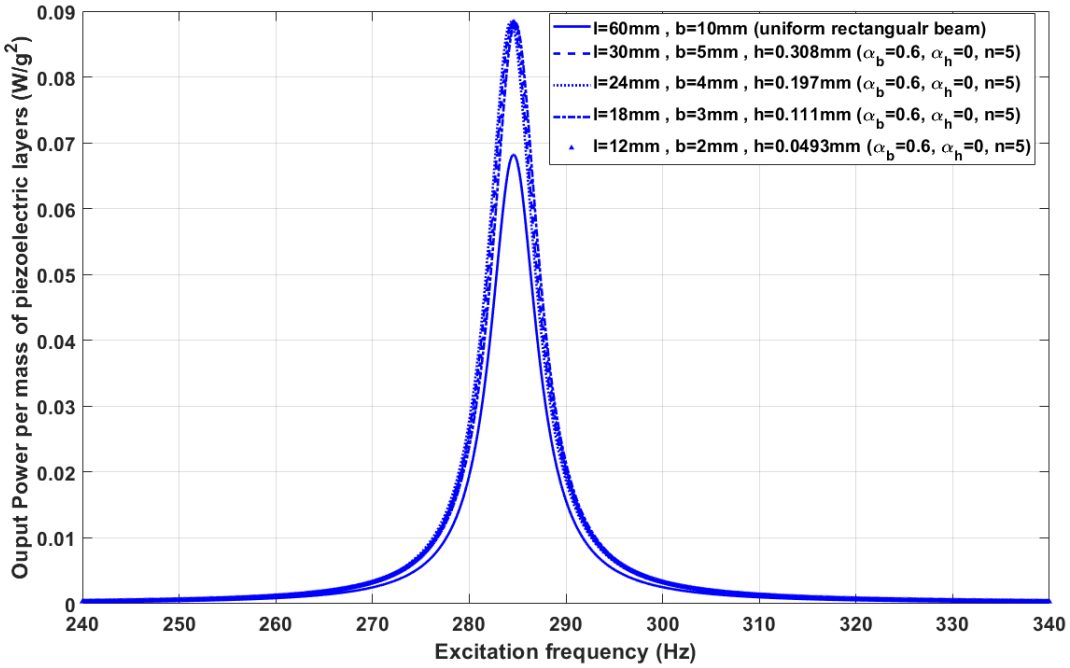

Figure 4.13 Comparison of power FRFs per piezoelectric mass between different beam sizes.

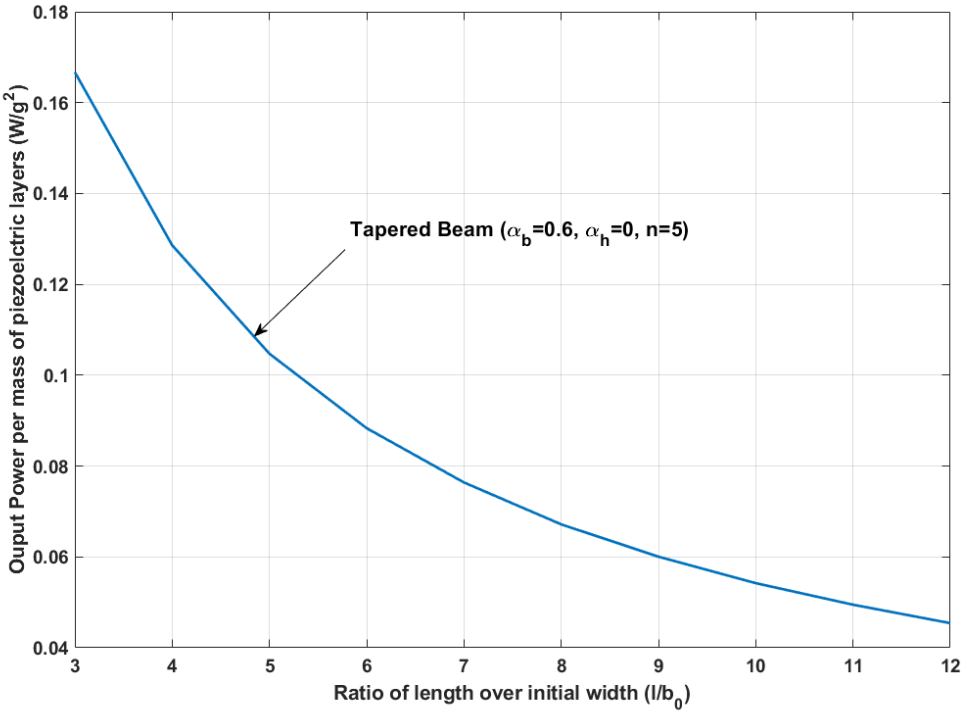

Figure 4.14 Comparison of maximum power output per piezoelectric mass between different beam ratios.

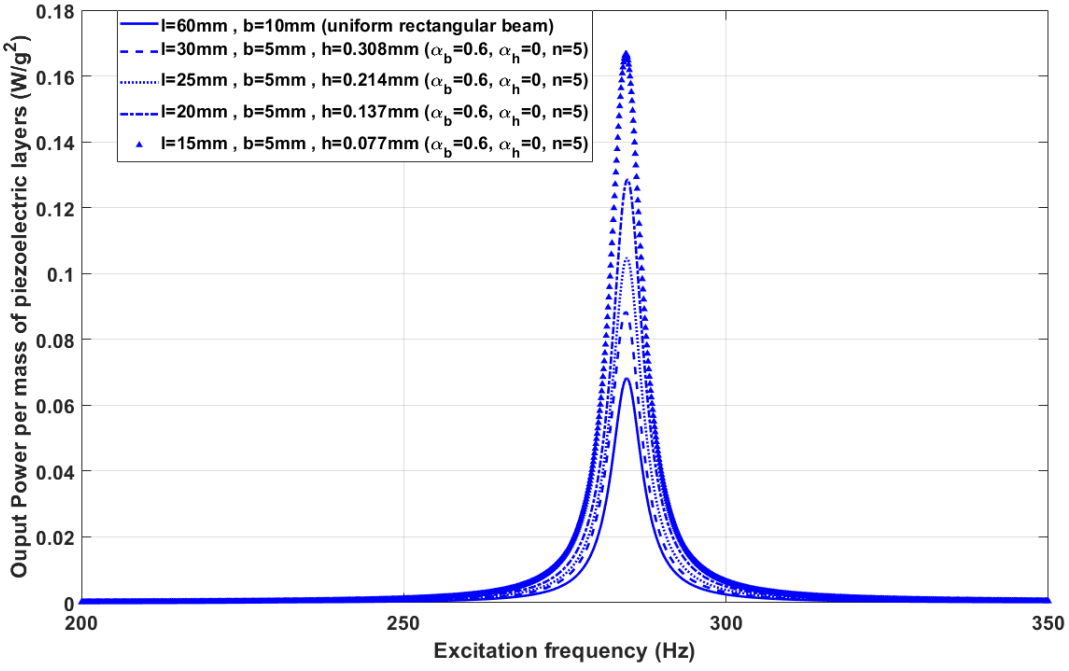

Figure 4.15 Comparison of power FRFs per piezoelectric mass between different length/width ratios.

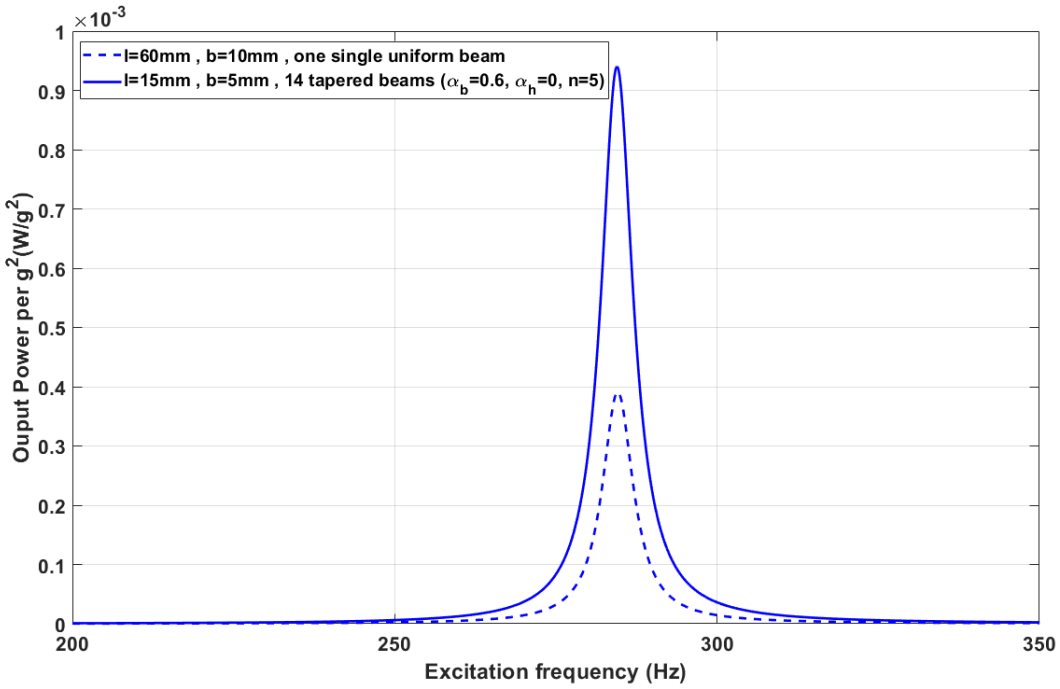

Figure 4.16 Comparison of power FRFs between the primary uniform beam and an array of tapered beams.

4.5 Conclusions

In this chapter, the effects of tapered beam on both the efficiency and the power output of PEHs were investigated. The influence of sizing on the amount of scavenged power was also studied and an enhanced system consisting of an array of uniform beams was proposed. For the analysis of the structure the superconvergent beam was taken into consideration. To validate the accuracy of the element the results available in the literature were compared. Application of this proposed element provided the great possibility of switching readily from the Timoshenko to the Euler-Bernoulli by changing the value of one coefficient (β).

Analysis of the non-uniform beams showed that when the tapering ratio increases (diverging beam) the output power rises while the efficiency decreases, and vice versa. Expanding the degree of polynomial function also intensified the increasing/decreasing pattern. For example, changing the degree from $n = 0$ to $n = 5$ for the tapered beam with the tapering properties $\alpha_b = \alpha_h = 0.5$ resulted in the power output increase by 1644.5%. The mentioned paradox for the trends of efficiency and power is originated from different amounts of input energy. It should be pointed out that changing the geometry of the beam (application of converging or diverging beam) changes

the fundamental resonance frequency of the structure, as well. It is feasible to improve the objective target (efficiency or power) by tapering according to a polynomial function. It can be concluded that although application of diverging beam results in the power output enhancement it increases the weight which is an important subject in different industries such as aerospace. In order to save more material, the sizing analysis and application of an array of beams was targeted as the second feasible concept.

In order to improve the power output with the same amount of material a new system consisting of an array of tapered beams (diverging beams) was proposed. In the new architecture although the same amount of piezoelectric material was used the harvested electrical power output increased significantly by 140%. Additionally, the weight of substrate layer is reduced by 15.64% by the application of thinner substrate layer. The results showed that in order to increase the power output it is not always necessary to employ thicker piezoelectric layers. The power output strongly depends on the properties of the system, especially the external load resistance. For the design of the new system the operation frequency (fundamental natural frequency) was kept constant. To tune the natural frequency of the smaller arrays of tapered beams to the original uniform beam the thinner layers were employed. Therefore, the new proposed architecture could provide a solution for the challenging task of recharging the batteries in wireless sensor nodes.

Chapter 5 Performance of non-uniform functionally graded piezoelectric (FGP) energy harvester beams

The appearance of functionally graded piezoelectric materials (FGPMs) has solved the lamination problem of the conventional piezoelectric structures. FGPMs are the new materials with unexplored capabilities. This chapter theoretically investigates the effects of non-uniformity on the performance of the FGPM cantilever beams subjected to harmonic excitation. The governing equations are derived based on Timoshenko and Euler-Bernoulli beam theories. The finite element method with the application of superconvergent element is employed here for the discretization and the vibration analysis of the system. The present model is validated by comparing the numerical results with the experimental results of piezoelectric energy harvesters of conventional shapes available in the open literature. Parametric studies are carried out with respect to the effects of tapering ratios, the degree of non-uniformity, load resistance, and the volume fraction parameter on the electrical output power and the fundamental resonance frequency. It was observed that the application of diverging beams noticeably enhances the power output per mass of piezoelectric element extracted while decreases the natural frequency which is advantageous for scavenging energy from ambient surroundings. The results reveal that there is an optimal value for the non-homogeneous parameter leading to the maximized harvested energy under different operating conditions.

5.1 Introduction

Energy harvesting and scavenging from external surrounding sources has become an interesting subject of research recently because the source of energy is freely available and its recuperation is environmentally friendly. Nowadays, the attention towards this subject has greatly increased owing to the simplicity and cost-effectiveness of the structure. In order to scavenge energy, the mechanical vibrations must be converted into electrical energy. This objective can be met through one of the three major conversion mechanisms including electrostatic, electromagnetic, and piezoelectric [5].

Piezoelectric energy harvester is one of the useful structures employed for direct energy harvesting from ambient vibrations to generate electrical energy. In comparison to electrostatic and electromagnetic approaches, the piezoelectric approach has high power conversion potential from the systems with small sizes [111]. These features exclude the application of piezoelectric energy harvesters (PEHs) to generate electrical energy for small devices such as autonomous wireless sensors [1]. A conventional piezoelectric energy harvester usually consists of a cantilever beam with a proof mass attached at the free end of the beam used for frequency tuning and increased deflection. The piezoelectric layers are glued on the top and bottom surfaces of the substructure. Based on the number of attached piezoelectric layers they are categorized into unimorph (one layer) and bimorph (two layers) configurations [6]. The conventional piezoelectric structures consist of a substrate and piezo layers. This configuration might lead to the existence of lamination problem owing to the stress discontinuity at the interface. To address the lamination problem while satisfying the high thermal and mechanical resistance properties functionally graded materials were developed by the Japanese in the 1960s [112]. They developed types of composites having a smooth variation of material properties from one surface to another. The concept has drawn attention for the design of piezoelectric energy harvesters.

Functionally graded piezoelectric materials (FGPMs) have been developed to remove discontinuity and render the sensing and actuating structures with a low level of stress concentration. By optimizing the volume fraction of two constituent phases it is possible to produce larger displacements resulting in higher output power [113]. The principle can also help designers to increase the lifetime of energy harvesting devices. This is a new type of practical approach requiring more attention and study.

So far, relatively limited studies have been carried out on the piezoelectric energy harvesters with various designs and represented approaches. The finite element modeling of functionally graded piezoelectric (FGP) cantilever beams in unimorph or bimorph configurations subjected to harmonic input was presented by [114]. They assumed the material properties of both the substructure and piezoelectric layers are graded across the thickness showing the power generated by functionally graded harvester is greater than the generated power by flexible PVDF harvester. They subsequently analyzed the time domain frequency of FGPMs subjected to random vibration [115]. Dealing with nonlinear vibration of bimorph FGPMs is another study carried out with some research team [113]. They considered the geometrical nonlinear terms (von Kármán nonlinearities) with the assumption of the Rayleigh beam theory. The theoretical results were validated using finite element simulation showing excellent agreements. Additionally, the new analytical model for the development of a functionally graded piezoelectric energy harvester (FGPEH) accounting the general nonlinear geometry was presented recently [116]. The need for systems with more scavenged power has pushed forward researchers to look for solutions. Parametric study and optimization of the design parameters are the strategies which can be adopted to improve the performance of piezoelectric energy harvesters. In this regard, [117] investigated theoretically the optimized energy harvesting characteristics of FGPM under harmonic excitation. It was revealed that the FGPM energy harvesters have superiority over the conventional structures so that by the optimization of the volume fraction parameter one can maximize the amount of scavenged energy under different operating conditions. One of the common approaches to enhance the power is the geometry modification of cantilever beams. This approach can create uniform strain distribution through the length of the beam and eventually higher electrical power output [72]. This is the kind of optimization process which has not taken into consideration about FGPEHs. Hence, further insight into the subject needs to be provided to be able to render higher electrical outputs.

In this chapter, the energy harvesting characteristics of tapered FGP cantilever beams subjected to harmonic excitation are investigated. The electromechanical coupling equations are derived using Hamilton's principle based on Timoshenko beam theory. Although the structure is modeled based on the first-order beam theory it can be easily converted to the Euler-Bernoulli beam theory with the application of superconvergent element considered here developed for FGPMs [52]. The studied system consists of a tapered bimorph beam in a series configuration wherein the width of the beam is changing based on the polynomial function with various degrees, ranging from one to

five. Firstly, in order to validate the results, the numerical solution is validated by the theoretical and experimental results in the literature. Furthermore, the parametric study is carried out to find the optimized system for different operating conditions. Tapering ratio, degree of the polynomial function, load resistance and volume fraction parameter are the design parameters and their effects on the performance of the structure are analyzed.

5.2 Formulation

A sketch of tapered FGP cantilever beam is shown in Fig. 5.1. The system is composed of a substrate layer covered by piezoelectric layers connected in series. The beam is excited at its base and it is assumed that there is a perfect bonding between the layers. The beam width varies along its length represented by $b(x)$, as explained in Eq. (5.1). A proof mass is also attached on the end of the beam for the fundamental frequency regulation.

$$b(x) = b_0\left(1 \pm \alpha\frac{x}{L}\right)^n \tag{5.1}$$

where α and n are the tapering ratio and polynomial function's degree, respectively.

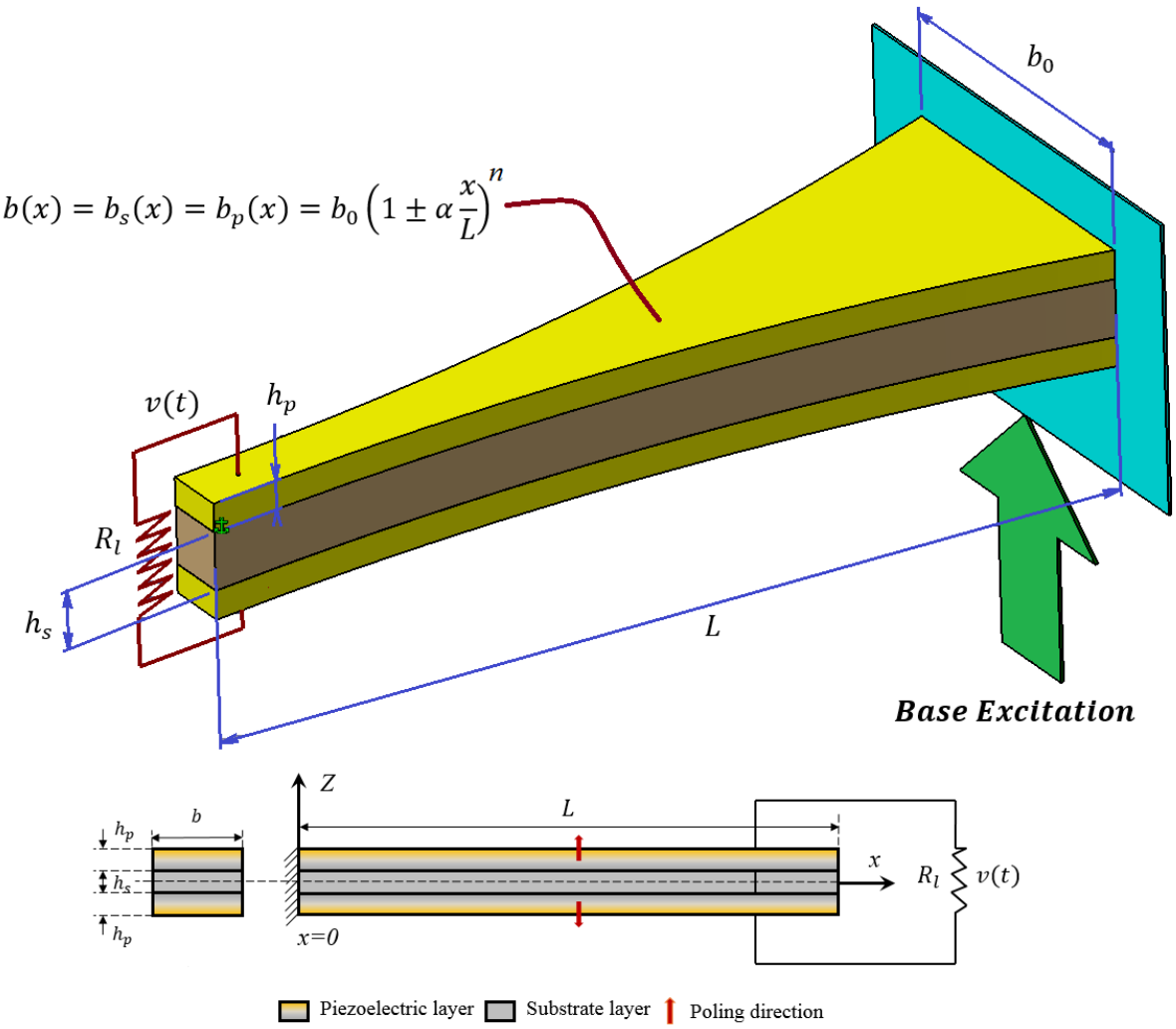

Figure 5.1 Cantilevered bimorph FGPEH under series connection.

5.2.1 Functionally graded piezoelectric model

In the considered system, the substrate layer is assumed to be made of pure metallic constituent while the piezoelectric layers are composed of both metallic and piezoelectric materials. The physical properties of each point of the functionally graded material obey the power-law function [113], expressed as:

$$p(z) = p_p + (p_s - p_p)\left(1 + \frac{h_s - 2|z|}{2h_p}\right)^N \tag{5.2}$$

where the subscripts p and s represent the piezoelectric and metallic phase, respectively. In Eq. (2), $p(z)$ denotes a typical material property (such as Young's modulus, density or piezoelectric constants) and the power N could be a variable, N ≥ 0. It is noticeable that when $N \to \infty$ the functionally graded parts are converging into pure piezoelectric layers.

5.2.2 Electromechanical coupling equations of non-uniform FGPEH

In order to derive the constitutive equations, at the outset it is necessary to calculate the total internal and external energies of the system. Based on Timoshenko beam theory, the displacement of a generic point is described by Eq. (4.1).

$$\boldsymbol{R} = \begin{Bmatrix} u(x,y,z,t) \\ v(x,y,z,t) \\ w(x,y,z,t) \end{Bmatrix} = \begin{Bmatrix} z\phi_x(x,t) \\ 0 \\ w_0(x,t) + g(t) \end{Bmatrix} \tag{4.1}$$

In Eq. (4.1), the variable w_0 is the displacements projected on the mid-plane, ϕ_x is the rotation of corresponding cross section at point x and time t relative to the moving base and $g(t)$ is the transversal translation coming from the base motion.

With the assumption of Lagrange strain tensor and linear piezoelectric constitutive equations [53], the kinetic and strain energies of the entire structure are described using the following equations.

$$\begin{aligned} U &= \frac{1}{2}\int [\sigma_{xx}\epsilon_{xx} + \tau_{xz}\gamma_{xz}]dV_s + \frac{1}{2}\int [\sigma_p\epsilon_p + \tau_p\gamma_p]dV_p \\ &= \frac{1}{2}\int_0^L \left[I_2^E \acute{\phi}_x{}^2 + I_0^G\left(\acute{w}_0{}^2 + \phi_x{}^2 + 2\phi_x\acute{w}_0\right)\right]dx \\ &+ \frac{1}{2}\int_0^L \left[J_2^E \acute{\phi}_x{}^2 + J_0^G\left(\acute{w}_0{}^2 + \phi_x{}^2 + 2\phi_x\acute{w}_0\right) + \frac{d_{31}}{h_p}J_1^E v(t)\acute{\phi}_x\right]dx \end{aligned} \tag{2.13}$$

$$
\begin{aligned}
T = \frac{1}{2}\int \rho\left(\dot{\boldsymbol{R}}.\dot{\boldsymbol{R}}\right)dV + \frac{1}{2}M_t[(\dot{w}_0 + \dot{g})|_{x=l}]^2 + \frac{1}{2}I_t\left[\dot{\phi}_x|_{x=l}\right]^2 \\
= \frac{1}{2}\int_0^L \left[I_0^\rho {\dot{w}_0}^2 + 2I_0^\rho \dot{w}_0\dot{g} + I_0^\rho \dot{g}^2 + I_2^\rho {\dot{\phi}_x}^2\right]dx \\
+ \frac{1}{2}\int_0^{\mathrm{L}} \left[J_0^\rho {\dot{w}_0}^2 + 2J_0^\rho \dot{w}_0\dot{g} + J_0^\rho \dot{g}^2 + J_2^\rho {\dot{\phi}_x}^2\right]dx \\
+ \frac{1}{2}M_t[(\dot{w}_0 + \dot{w}_b)|_{x=l}]^2 + \frac{1}{2}I_t\left[\dot{\phi}_x|_{x=l}\right]^2
\end{aligned}
\tag{4.4}
$$

where σ_p is the normal stress, τ_p is the shear stress, ϵ_p is the normal strain, γ_p is the shear strain, G_p is the shear modulus, E_p is the elastic modulus, D_3 is the electric displacement, d_{31} is the piezoelectric strain coefficient, ε_{33}^T is the dielectric permittivity of piezoelectric layer at constant stress and finally K_s and E_3 are the shear correction factor and the electric field across the piezoelectric layer. Additionally, M_t and I_t are the tip mass and its associated moment of inertia. The integral coefficients are also defined in the following

$$
I_i^E \triangleq \iint z^i E_s dydz\ ,\ \ I_0^G \triangleq \iint K_s z^i G_s dydz\ ,\ \ I_i^\rho \triangleq \iint z^i \rho_s dydz\ , i = 0,1,2 \tag{2.15}
$$

$$
\begin{aligned}
J_i^E \triangleq \iint z^i E_p(y)dydz\ ,\ \ J_0^G \triangleq \iint K_s z^i G_p(y)dydz\ ,\ \ J_i^\rho \triangleq \iint z^i \rho_p(y)dydz\ , i \\
= 0,1,2
\end{aligned}
\tag{5.3}
$$

It should be pointed out that the material properties E_p, G_p, and ρ_p are defined using Eq. (5.2). The internal electrical energy is defined as follows:

$$
\begin{aligned}
\mathrm{W}_{IE} = \frac{1}{2}\int E_3 D_3\, dV_p = -\frac{1}{2}\frac{v(t)}{h_p}\int \left[E_p d_{31}\left(z\acute{\phi}_x\right) - \frac{v(t)}{h_p}\varepsilon_{33}^S\right]dV_p \\
= -\frac{1}{2}\frac{v(t)}{h_p}d_{31}\int_0^L J_1^E \acute{\phi}_x dx + \frac{1}{2}C_p v(t)^2
\end{aligned}
\tag{4.5}
$$

where C_p is the internal capacitance of the piezoceramic parts. The capacitance for one layer of piezoelectric material is calculated as in Eq. (2.18).

$$C_p = \varepsilon_{33}^S \frac{A_p}{h_p} \tag{2.18}$$

where ε_{33}^S is the dielectric permittivity at constant strain and A_p is the electrode area.

The only remaining part is the calculation of the non-conservative virtual work owing to the electric charge output $Q_u(t)$ defined in Eq. (2.22).

$$\delta W_{nc} = Q(t)\delta v(t) \tag{2.22}$$

By having all of the energy parts, the governing equations can be derived by the application of Hamilton's principle (Eq. 2.21).

$$\int_{t_1}^{t_2} (\delta T - \delta U + \delta W_{IE} + \delta W_{nc}) dt = 0 \tag{2.21}$$

where δT, δU, δW_{IE} and δW_{nc} are the virtual works of the total kinetic energy, the strain energy, the internal electrical energy and the energy from non-conservative mechanical force, respectively.

Analyzing the effects of damping structure is the completing part required to be added to the equations to increase the accuracy of modeling. The proportional damping (Rayleigh damping) is applied here [65].

5.3 Discretization of equations using superconvergent element (SCE)

In order to derive the coupling equations, it is necessary to discretize the coupled model. There are different methods which can be adopted to meet the requirements. Finite element model (FEM) is the kind of useful method employed here. Regarding FEM, the superconvergent element is considered for higher accuracy. This type of element contains two nodes and four degrees-of-

freedom (DOF), including two DOF in the transverse direction and two DOF in the rotational direction (Fig. 2.2). As one of the noticeable advantages, the element provides a precise response with the minimum number of elements since the shape functions are derived by using static equilibrium (Appendix C). Another remarkable advantage of this practical element is the simple switching method between the Timoshenko and Euler-Bernoulli beam theories. In fact, it is possible to switch readily from the Timoshenko to the Euler-Bernoulli by changing the value of one coefficient (β), as described in Appendix C. Hence, application of this element results in an analysis of both beam theories without the need of extra calculations [52]. Considering the shape function of the SCE, the displacement parameters in terms of the nodal displacements are represented in Eq. (4.5).

$$\begin{bmatrix} w_0(x,t) \\ \phi_x(x,t) \end{bmatrix} = \begin{bmatrix} N_w(x) \\ N_\phi(x) \end{bmatrix} a(t) = \begin{bmatrix} \psi_1^e(x) & \psi_2^e(x) & \psi_3^e(x) & \psi_4^e(x) \\ \varphi_1^e(x) & \varphi_2^e(x) & \varphi_3^e(x) & \varphi_4^e(x) \end{bmatrix} \begin{bmatrix} W_1^e(t) \\ \phi_1^e(t) \\ W_2^e(t) \\ \phi_2^e(t) \end{bmatrix} \tag{4.5}$$

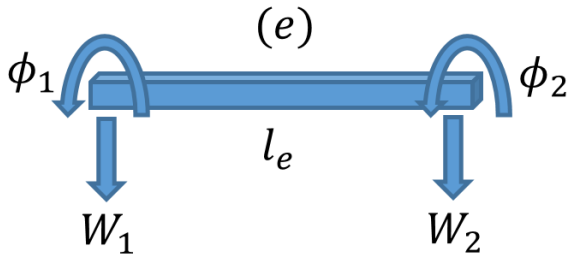

Figure 2.2 Two-node finite element with four DOF.

where $N_w(x)$ and $N_\phi(x)$ are the shape functions and $a(t)$ is the vector of unknown generalized coordinates. By substitution of Eq. (4.5) into Eq. (2.21), addition of the Rayleigh damping and performing integration by parts, the electromechanical coupling equations for a typical finite element is obtained in Eqs. (2.25) and (2.27). The damping parts accounts for the mechanical dissipative effects (Eq. (2.28)).

$$\boldsymbol{M^e \ddot{a}(t) + C^e \dot{a}(t) + K^e a(t) - \theta^e v(t) = f^e} \tag{2.25}$$

$$\overline{C_p} \dot{v}(t) + \frac{v(t)}{R_l} + \boldsymbol{\theta^{eT} \dot{a}(t)} = 0 \tag{2.27}$$

$$\boldsymbol{C^e} = \mu \boldsymbol{M^e} + \gamma \boldsymbol{K^e} \tag{2.28}$$

where μ and γ are the constants of mass and stiffness proportionality. Terms $\boldsymbol{M^e}$, $\boldsymbol{C^e}$, $\boldsymbol{K^e}$, $\boldsymbol{\theta^e}$, $\boldsymbol{f^e}$ are, respectively, the mass matrix; the damping matrix; the elastic stiffness matrix; the electromechanical coupling matrix and the vector of dynamical forces corresponding to one element of the piezoelectric cantilever beam, and $\overline{C_p}$ is the equivalent capacitance (Appendix E).

5.4 Frequency response of the coupling equations

Assume the FGPEH is exposed to a harmonic base displacement $g(t) = Xe^{i\omega t}$, where ω is the excitation frequency. Using this assumption, the forcing vector is calculated as

$$\boldsymbol{f^e} = \left[\omega^2 X \int_0^{l_e} \left(I_0^\rho + J_0^\rho\right) {N_w}^T dx\right] e^{i\omega t} \tag{2.29}$$

Since the applied force is assumed to be harmonic, the nodal displacement and the output voltage can be defined as $\boldsymbol{a(t)} = \boldsymbol{A}e^{i\omega t}$ and $v = Ve^{i\omega t}$, respectively. Therefore, the assembled steady-state forms of electromechanical coupling equations can be summarized as Eqs. (2.30) and (2.31).

$$(-\boldsymbol{M}\omega^2 + i\omega\boldsymbol{C} + \boldsymbol{K})\boldsymbol{A} - \boldsymbol{\theta}V = \boldsymbol{F} \tag{2.30}$$

$$i\omega\boldsymbol{\theta^T A} + \left(i\omega\overline{C_p} + \frac{1}{R_l}\right)V = 0 \tag{2.31}$$

Solving the above equation simultaneously derives the output voltage explicitly as follows

$$v(t) = -i\omega\left(i\omega\overline{C_p} + \frac{1}{R_l}\right)^{-1} \boldsymbol{\theta^T}\left[-\boldsymbol{M}\omega^2 + i\omega\boldsymbol{C} + \boldsymbol{K} + i\omega\left(i\omega\overline{C_p} + \frac{1}{R_l}\right)^{-1}\boldsymbol{\theta\theta^T}\right]^{-1}\boldsymbol{F}e^{i\omega t} \tag{2.34}$$

5.5 Validation and parametric studies

In this section, initially, the validation part is carried out to verify the accuracy of the present structure and the considered element. Subsequently, the effects of different parameters including the external load resistance, volume fraction parameter, tapering ratio and the degree of non-uniformity are investigated to arrive at the optimal system rendering the highest amount of electrical power.

5.5.1 Validation of the present model

Like the first part, the convergence of the superconvergent element and the accuracy of the present numerical solution is validated by investigating two different systems. The first system consists of a uniform bimorph cantilever beam as previously reported [62]. As is already mentioned, the present theory of FGPEH can be easily reduced into that of conventional piezoelectric laminate beams by setting the parameter $n \to \infty$. The mechanical and electrical properties of the bimorph piezoelectric beam connected in series are listed in Table 5.1. Other calculating parameters are $R_l = 1000\Omega,\ M_t = 12g,\ I_t = 0,\ \xi = 0.027$. The frequency response functions (FRFs) of output voltage using the experimental analysis and the present method are compared and depicted in Fig. 5.2. From the graphs it is seen that the results are in very good agreement.

Table 5.1 Properties of the bimorph piezoelectric cantilever beam.

Property	Piezoelectric layer	Substrate layer
Material	PZT-5H	Brass
Density ρ (kg/m^3)	7800	9000
Length (mm)	50.8	50.8
Thickness (mm)	0.26	0.14
Width (mm)	31.8	31.8
Young's modulus E (GPa)	66	105
Piezoelectric strain coefficient d31(pC/N)	-190	–
Dielectric permittivity at constant strain ε_{33}^{S} (nF/m)	13.28	–

The numerical fundamental frequency calculated using the present model is 45.7 Hz which is in agreement with the experimental frequency (45.6 Hz). This comparison proves the excellent convergence rate of SCE in which, by using only one superconvergent element the difference between the experimental and theoretical values is extremely low (0.22%).

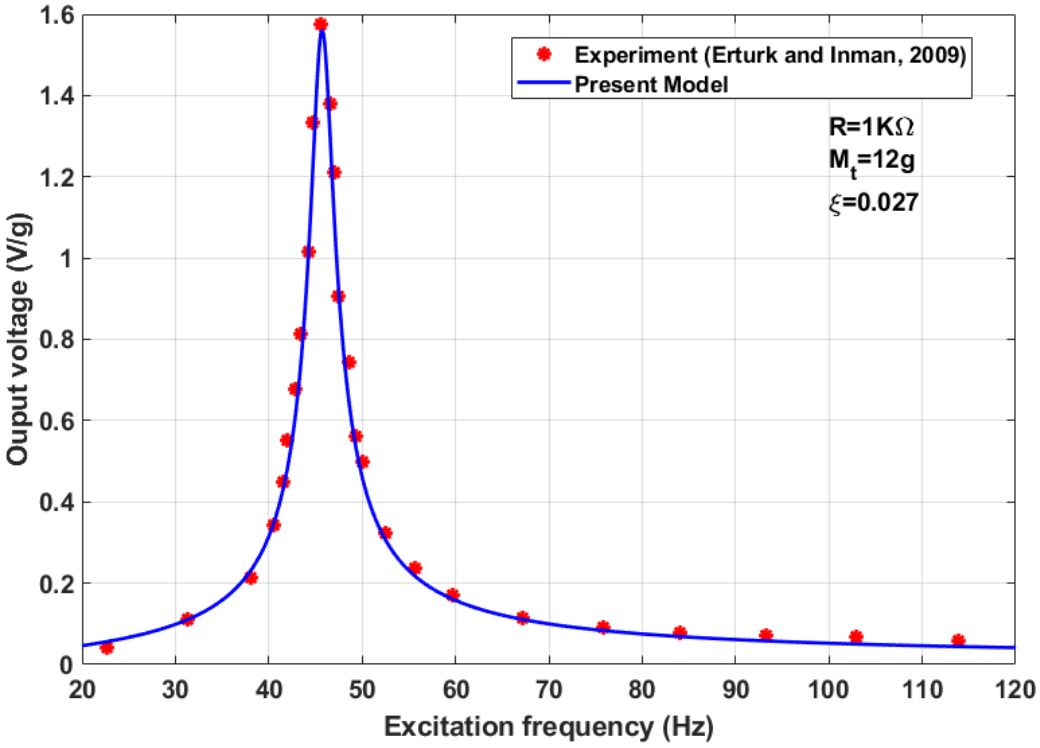
Experiment (Erturk and Inman, 2009)
Present Model
R=1KΩ
M_t=12g
ξ=0.027
Ouput voltage (V/g)
Excitation frequency (Hz)
0
0.2
0.4
0.6
0.8
1
1.2
1.4
1.6
20
30
40
50
60
70
80
90
100
110
120

(a)

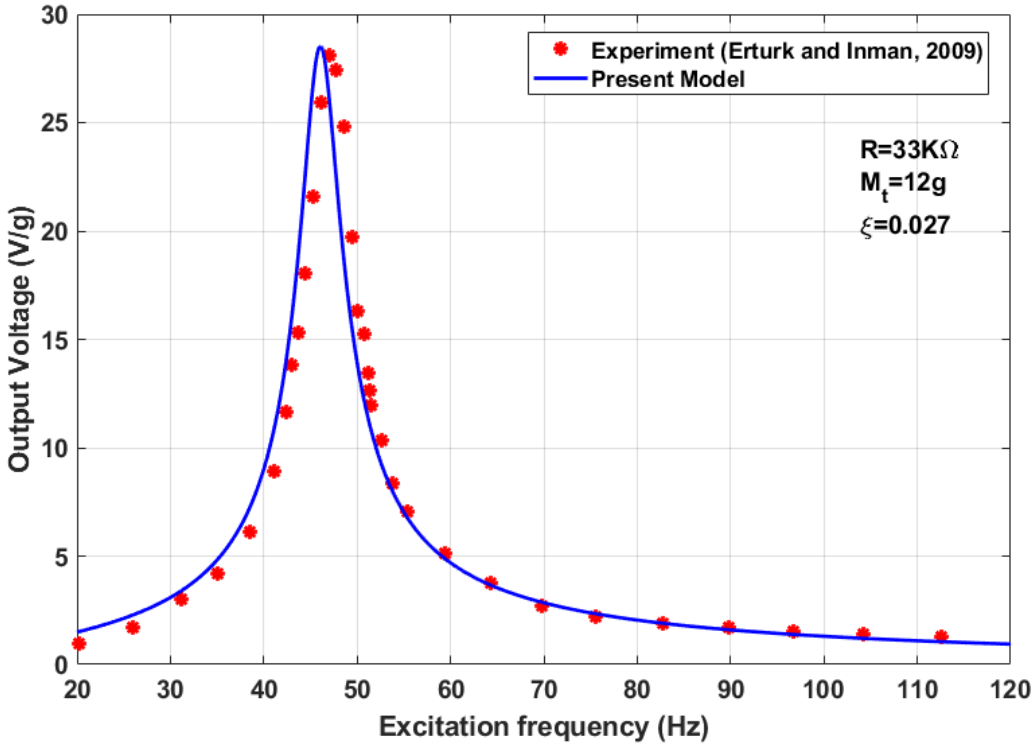
Experiment (Erturk and Inman, 2009)
Present Model
R=33KΩ
M_t=12g
ξ=0.027
Output Voltage (V/g)
Excitation frequency (Hz)
0
5
10
15
20
25
30
20
30
40
50
60
70
80
90
100
110
120

(b)

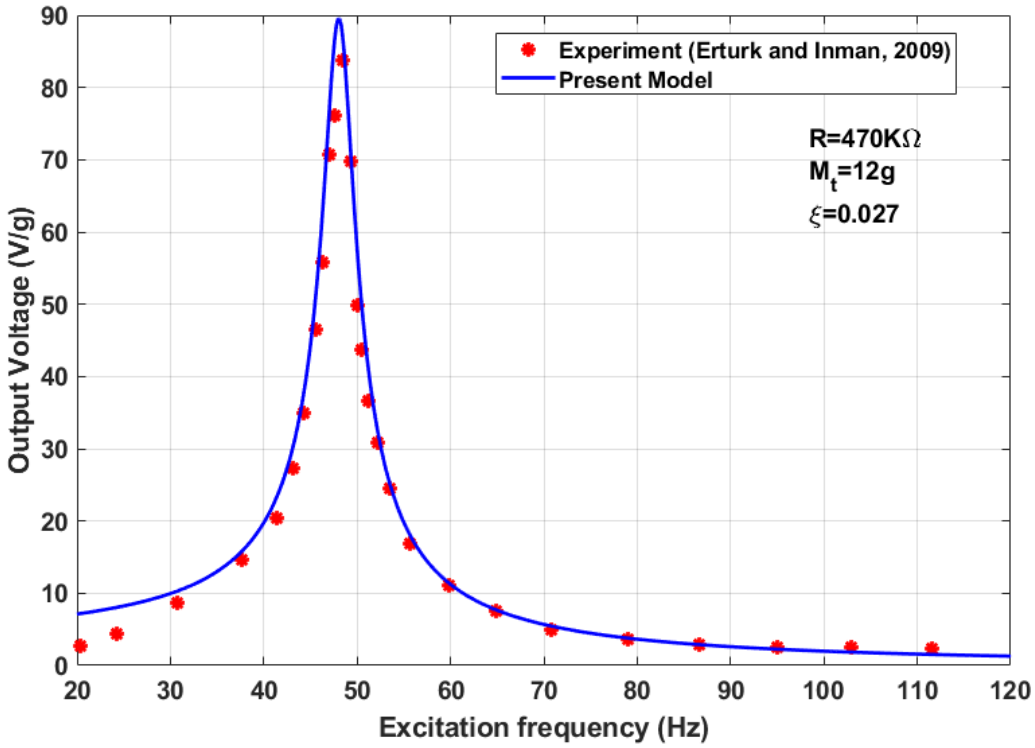

(c)

Figure 5.2 Validation of the power frequency response functions for different load resistances; (a) Voltage FRF for 1kΩ, (b) Voltage FRF for 33kΩ, (c) Voltage FRF for 470kΩ.

In the second part of the validation, the output voltage of one non-uniform PEH is analyzed [72]. It was assumed that the width of the beam is varying exponentially through the length given by $b(x) = b_0 e^{-cx}$. The electrical resistance and damping ratio are taken 1000 Ω and 1 percent, respectively, and other properties are listed in Table 3.1. The output voltage for different geometric conditions are achieved and provided in Table 5.1. As can be seen, the relative error between the numerical and analytical results is less than 0.7 percent although only one SCE is employed.

Table 3.1 Properties of the bimorph piezoelectric cantilever beam.

Property	Piezoelectric layer	Substrate layer
Material	PZT-4	Steel
Density ρ (kg/m^3)	7960	7800
Length (mm)	60	60
Thickness (mm)	0.6	0.7
Width (mm)	10	10
Young's modulus E (GPa)	81.3	200
Piezoelectric strain coefficient d31(pC/N)	-123	–
Dielectric permittivity at constant strain ε_{33}^{S} (nF/m)	13.059	–

Table 4.3 Validation of piezoelectric energy harvester's voltage for different tapering values.

c	0	5	10	15	20
Analytic (V/g) [72]	0.6252	0.5479	0.4802	0.4214	0.3704
SCE element (V/g)	0.6252	0.5470	0.4800	0.4225	0.3729
Difference (%)	0	0.16	0.042	0.26	0.67

In the last part of validation the results of the present study for the uniform functionally graded beam are compared with the results presented by [117]. The verifications are carried out under two different damping ratios in the case of $n = 1$. As shown in Fig. 5.3, the predicted frequency responses of the average output power are in good agreement with that in the open literature. The figure indicates that with increasing the damping ratio a dramatic reduction occurs in the peak value of the average power.

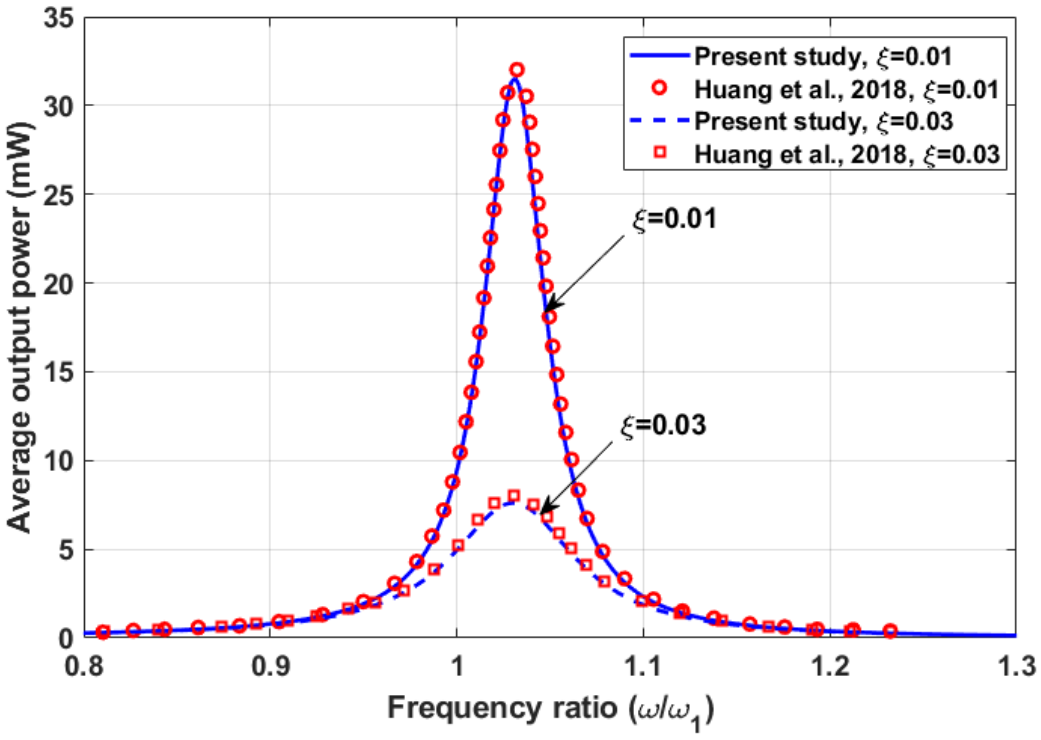

Figure 5.3 Frequency response of the average power under different damping ratios.

5.5.2 The effects of non-uniformity on the performance of tapered FGPEHs

To optimize the performance, the effects of different parameters need to be investigated. In the first part, in order to investigate the effects of non-uniformity one bimorph non-uniform beam with the properties listed in Table 3.1 is considered. It is assumed that there is pure piezoelectric layers for the piezoelectric part ($N \to \infty$). The maximum output voltage and power for different types of non-uniform beams are calculated, as shown in Figs. 5.4-5.5. Additionally, the variation of the fundamental natural frequency is plotted in Fig. 5.6. The results are computed for the electrical resistance of 1000Ω and the damping ratio of 0.01.

As shown, there are similar changing patterns in the curves of output voltage and power. By increasing the degree of polynomial function and tapering ratio the electrical output increases. As an example, changing the polynomial degree from zero (straight beam) to five for the highest tapering ratio case ($\alpha = 0.6$) can result in 246.5% and 1100.9% improvement in voltage and power, respectively. Conversely, the fundamental frequency would decrease if the polynomial degree increases for the diverging beams ($\alpha > 0$). This kind of pattern is useful for the design of

energy harvesters which scavenge energy from the ambient surroundings in which the fundamental frequency is lower than 200 Hz [5]. Hence, application of the diverging beams can result in not only increasing the electrical output, but also decreasing the fundamental resonance frequency. Admittedly, the desirable resonance frequency determines the optimal non-uniformity values.

To prove the enhancement efficiency of diverging beams the normalized output power variation of FGPEH (power per mass of piezoelectric parts) for different non-uniformity conditions is plotted in Fig. 5.7. It is clear from the figure that the normalized power increases monotonically with increasing tapering ratio along with the polynomial degree. For example, application of a converging beam with the properties $\alpha = 0.6$ and $N = 5$ leads to 174% normalized power enhancement.

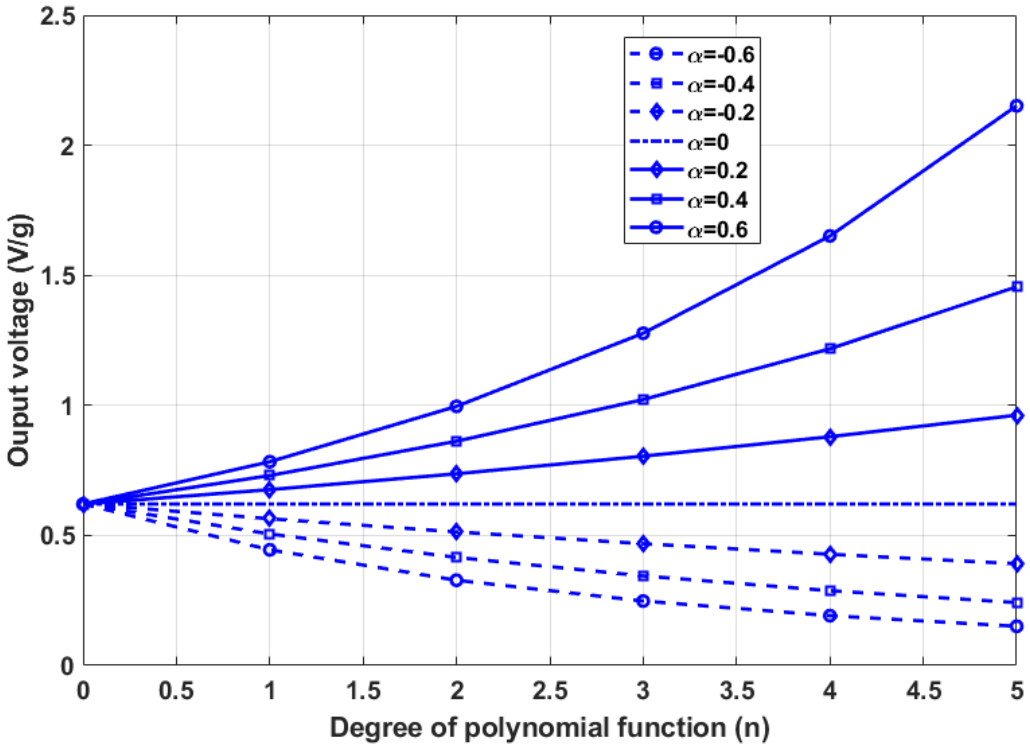

Figure 5.4 Output voltage variation versus polynomial's degree under different tapering ratios.

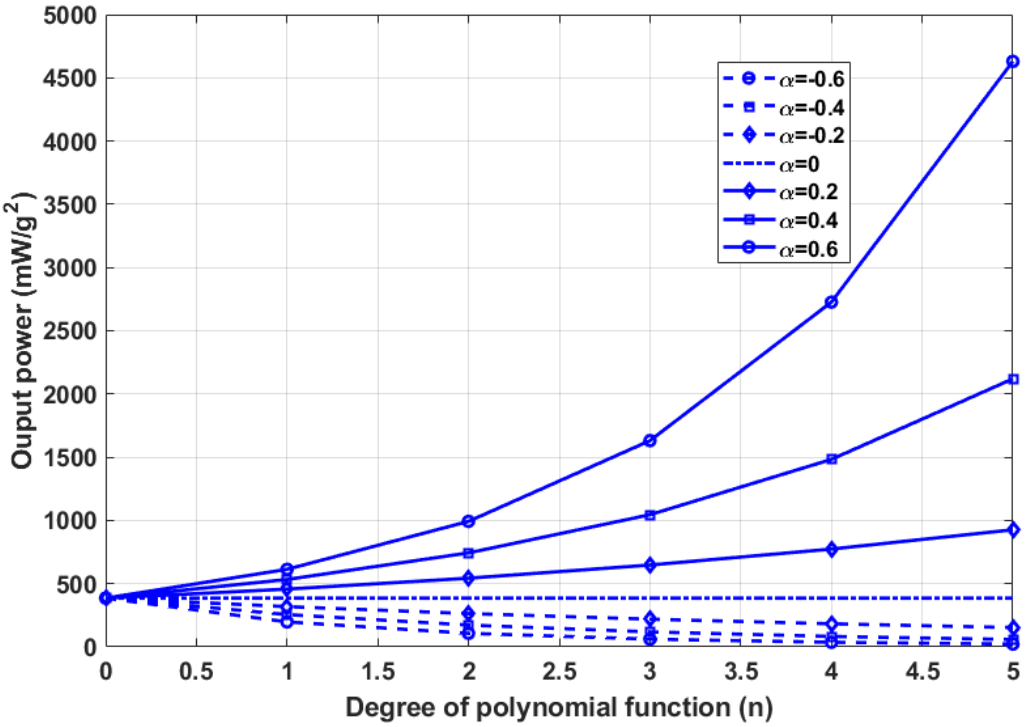

Figure 5.5 Output power variation versus polynomial's degree under different tapering ratios.

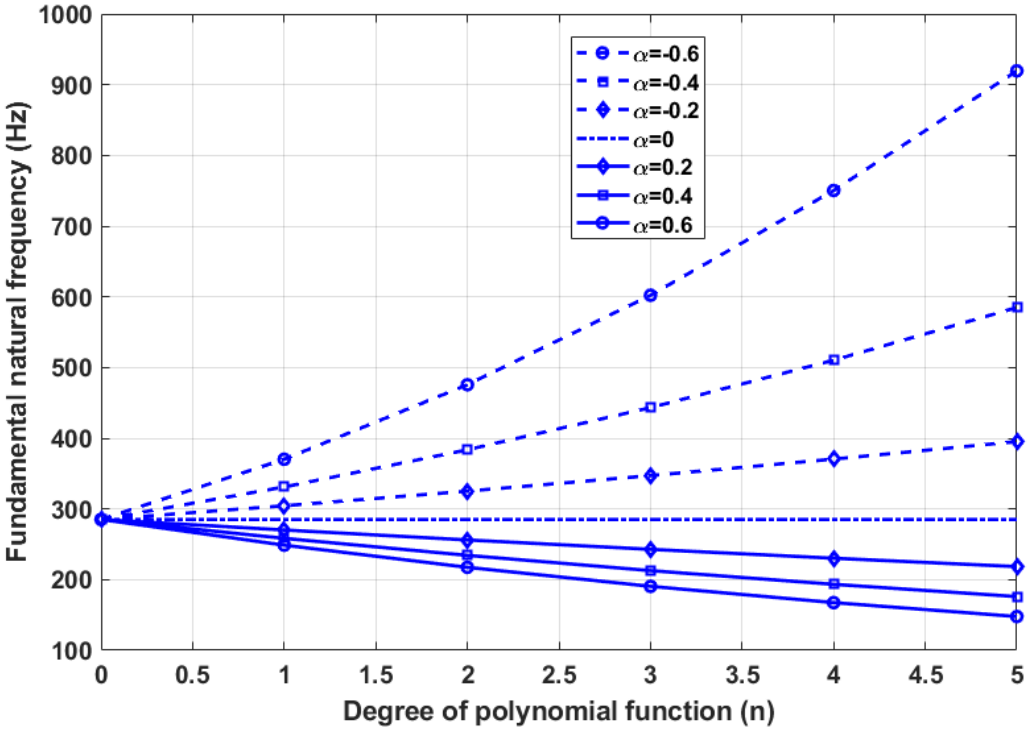

Figure 5.6 Fundamental frequency variation versus polynomial's degree under different tapering ratios.

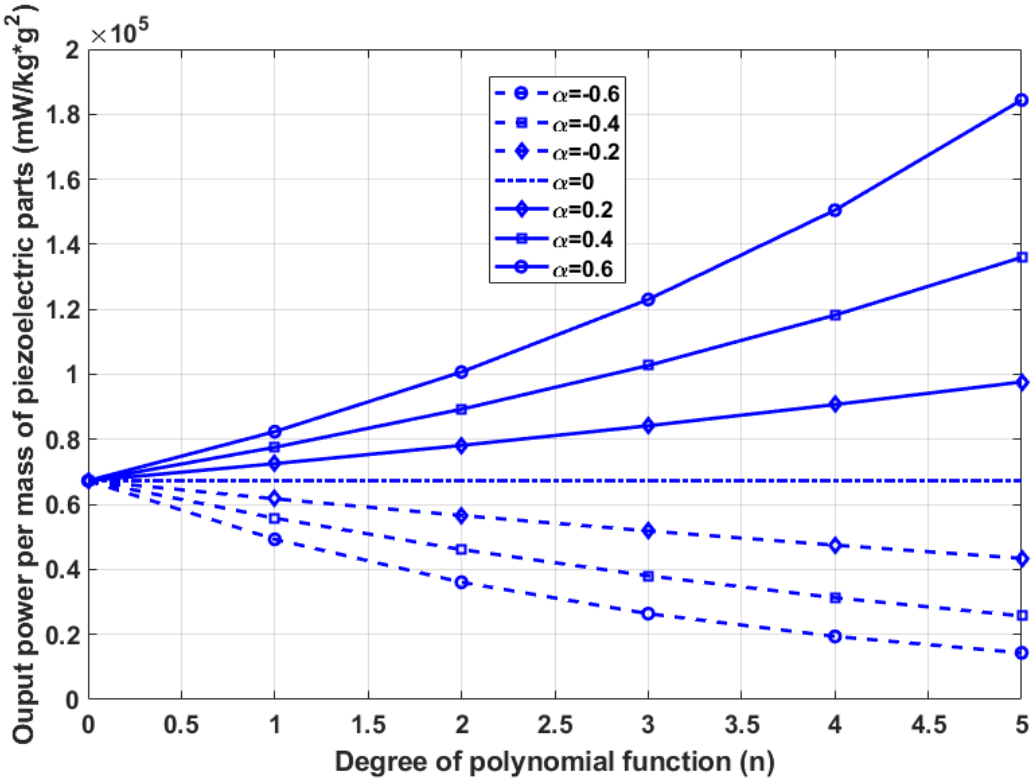

Figure 5.7 Variation of output power per mass of piezoelectric parts versus different non-uniformity conditions.

5.5.3 Effects of volume fraction parameter on the performance of tapered FGPEHs

As the second part of study, the influence of volume fraction parameter on the natural frequency and the electrical outputs are investigated. The variation of parameters is illustrated in Figs. 5.8-5.9. As is obvious from the graphs, the curves of electrical outputs obey similar changing rules. They start from zero, which corresponds to pure metallic phase (N=0), and as n increases, both curves rise to the maximal values to hit a plateau. Unlike the electrical output parameters, the fundamental natural frequency decreases as the volume fraction parameter goes up. Increasing the parameter n has a decreasing effect so that the figures indicate a dramatic reduction in the peak values when n changes from 0.1 to 10. The decreasing pattern continues to the point that the values reach a minimum value while n is around 15 and then experiences a period of stability. There is a trade-off between the output power and frequency for the design of an optimized system. Thus, when the operating frequency is pre-determined, there is an optimal volume fraction value corresponding to the maximal energy harvesting performance.

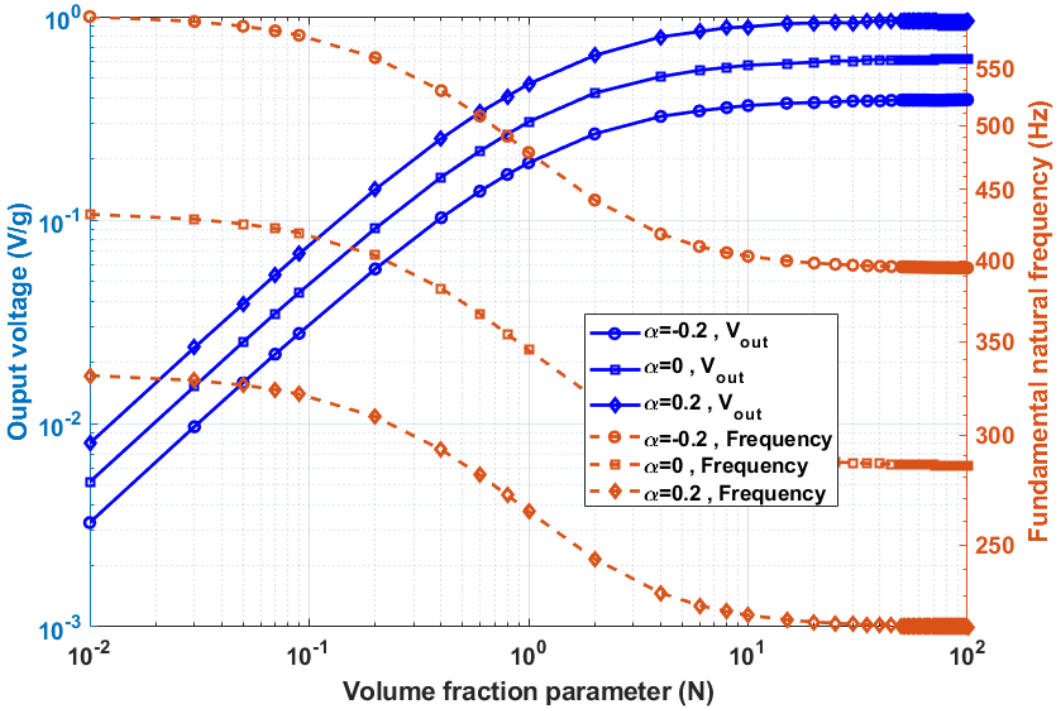

Figure 5.8 Output voltage and frequency variation of FGPEH versus volume fraction parameter for quintic geometry (N=5).

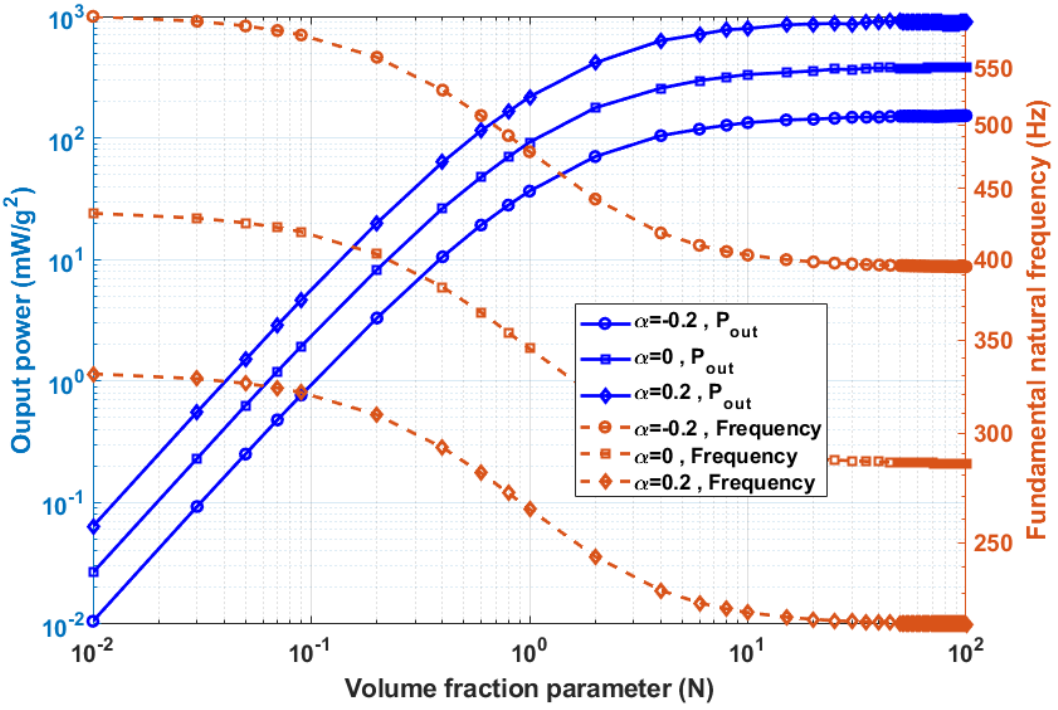

Figure 5.9 Output power and frequency variation of FGPEH versus volume fraction parameter for quintic geometry (N=5).

To better understand the effects of non-uniformity, the variation of the electrical power output and fundamental natural frequency for two tapered FGPEH versus a wide range of volume fraction parameter is depicted in Figs. 5.10-5.11. The variation is calculated for three different degrees of polynomial function. Figs. 5.10-5.11 show the variation behavior for a diverging beam ($\alpha = 0.6$) and a converging beam ($\alpha = -0.6$), respectively. As to be expected, by increasing the volume fraction parameter the electrical output increases to reach a stable value. Conversely, the fundamental resonance frequency decreases to experience a minimum value around 15 Hz and remain constant as N rises. The variation pattern for the converging beam is the same as the diverging geometry while increasing n leads to higher and lower power outputs for diverging and converging beams, respectively.

In the last part of this section the variation of the difference between the open-circuit and short-circuit frequencies versus the functionally graded parameter n is analyzed, as depicted in Fig. 5.12. The results for both the converging and diverging beams with different tapering ratios are computed. The percentage of frequency difference is defined in Eq. 5.4. It can be concluded from the figure that the frequency difference rises as the volume fraction parameter increases. The maximum difference belongs to the pure piezoelectric constituent. Additionally, the higher the tapering ratio is, the larger the frequency difference would result.

$$FD = \frac{\left[\omega_{open-circuit} - \omega_{short-circuit}\right]}{\omega_{short-circuit}} \times 100 \tag{5.4}$$

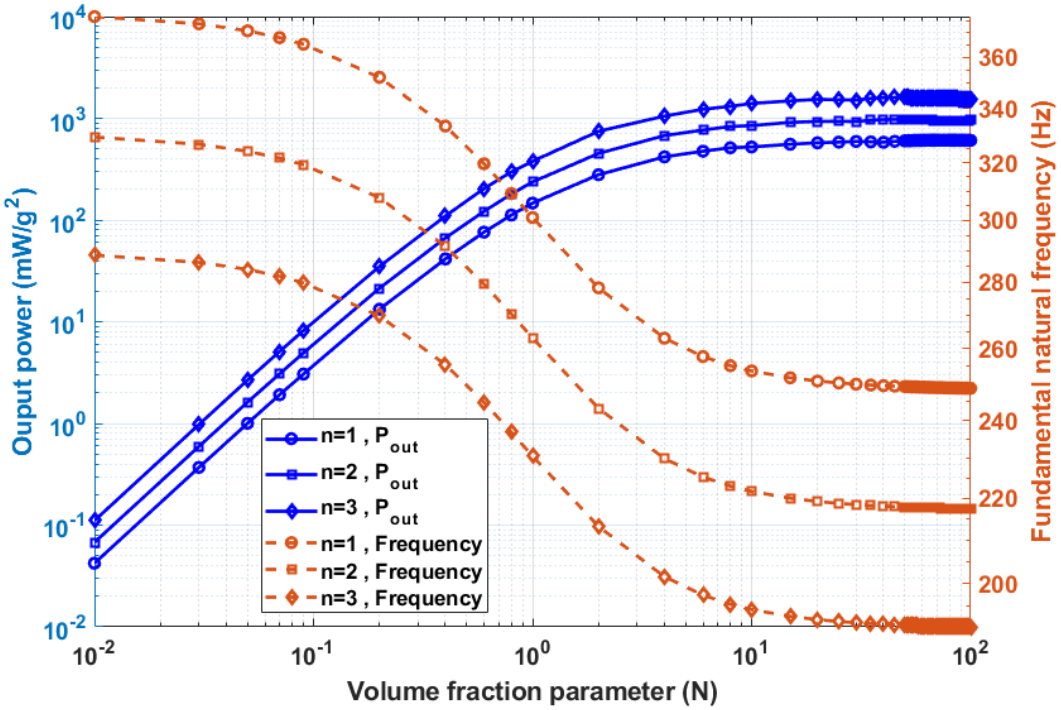

Figure 5.10 Output power and frequency variation of diverging FGPEH ($\alpha = 0.6$) versus volume fraction parameter under different polynomial degrees.

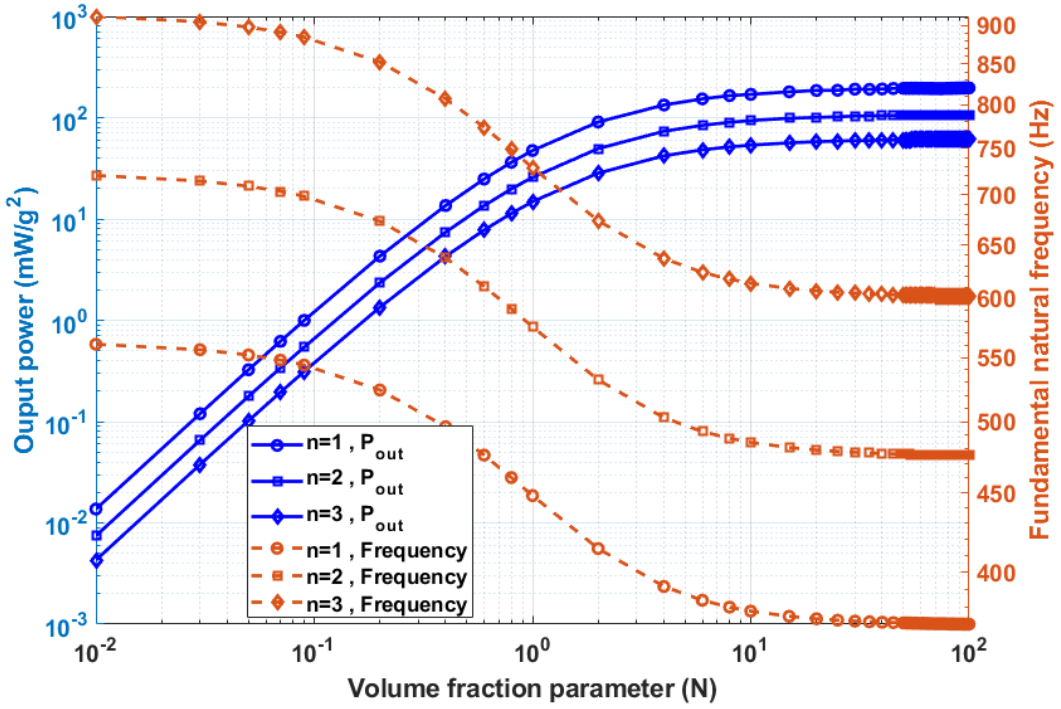

Figure 5.11 Output power and frequency variation of converging FGPEH ($\alpha = -0.6$) versus volume fraction parameter under different polynomial degrees.

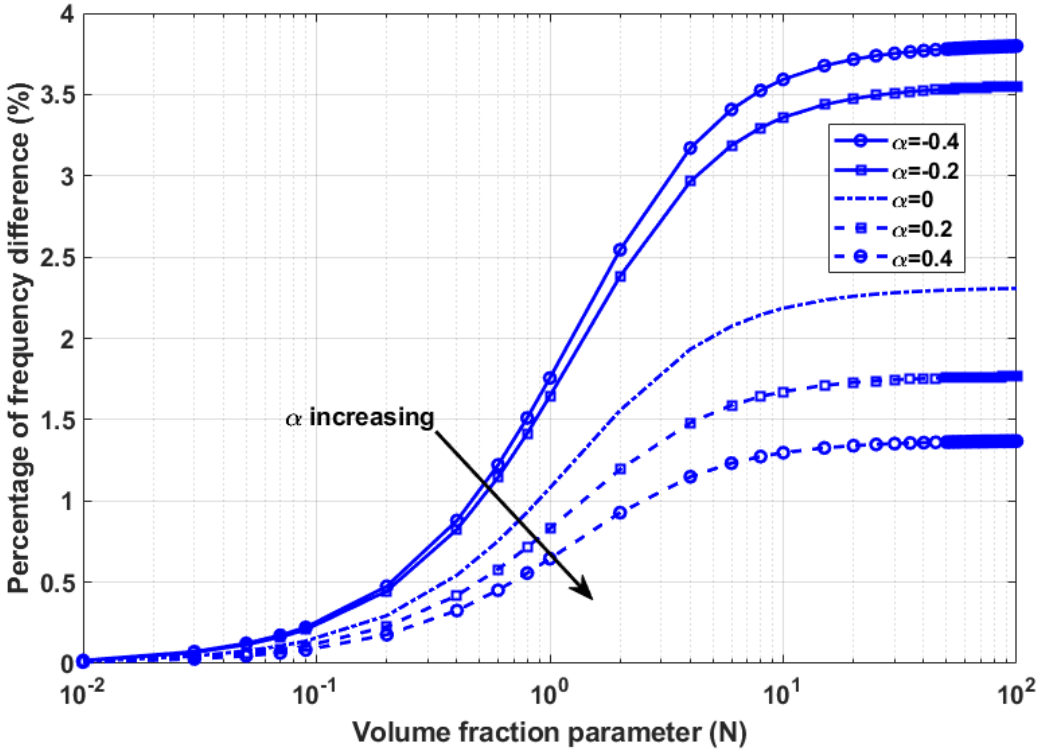

Figure 5.12 Frequency difference variation versus volume fraction parameter under different tapering ratios.

5.5.4 The effect of external load resistance on the performance of tapered FGPEHs

The following part will focus on the effects of the external load resistance on the energy harvesting performance of non-uniform FGPEHs. Firstly, the effects of load resistance on the electrical output and resonance frequency of a converging and a diverging beam are investigated, as shown in Figs. 5.13-5.16. The load resistance selection covers the short-circuit and open-circuit cases. Setting R_l to be 102 and 106 represent the short-circuit and open-circuit cases, respectively [62]. As the results show, with the volume fraction parameter increasing, the output power increases to reach a maximum value and remain constant. Additionally, by raising the employed load resistance the output power gradually increases until the open-circuit condition case for which the output power tends to be stable during the whole range of employed volume fraction parameter. Figs. 5.13 and 5.15 illustrate that the variation pattern of output power should be divided into two separate areas. The first area belongs to $n < 0.02$ in which the rise of the load resistance has an increasing effect on the output power. For the second section ($n > 0.02$) there is an optimal

resistance value in the range 104-106 corresponding to the maximal harvested power. The predicted changing patterns are in agreement with the results presented by [117]. Conversely, the short-circuit and open-circuit frequencies reduce gradually from the maximum value associated with $n = 0$ to the minimum values when $n \to \infty$.

In the second part of this section, the effects of external load resistance on the output power of tapered FGPEHs are examined in Figs. 5.17-5.20. Four different cases with n=0.1, 1, 10, and 100 are considered. From the results of the analysis, it is obvious that for every considered condition there is an optimal load resistance leading to the highest amount of scavenged energy. As the load resistance increases from zero the output power increases dramatically to reach a peak and plunging down after passing the optimal value. As was expected, the peak values of diverging beams are larger than converging beams while their resonance frequencies are lower. It is also noticeable that increase of n pushes back the peak values towards the lower external load resistance.

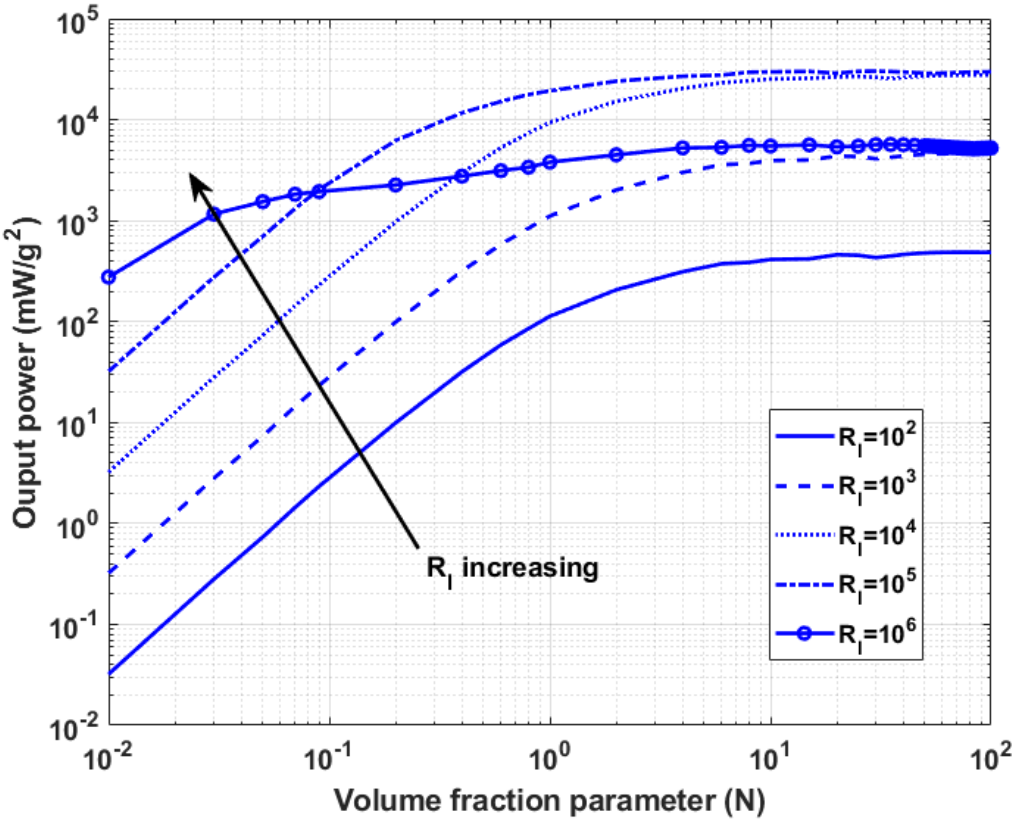

Figure 5.13 Output power variation of a diverging FGPEH ($\alpha = 0.6$, $N = 5$) under different external load resistances.

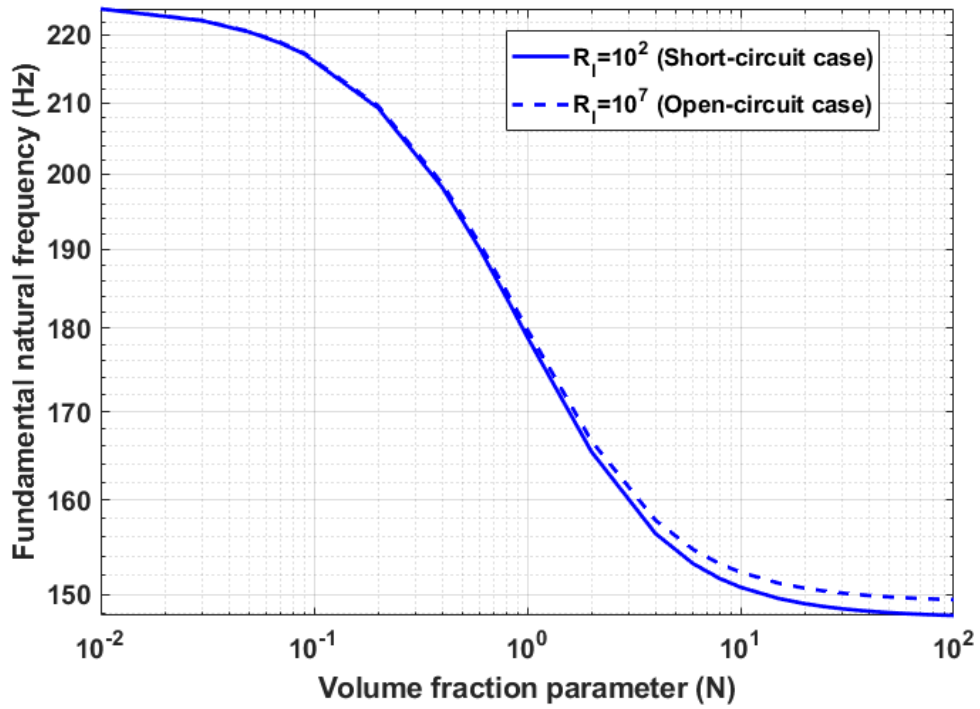

Figure 5.14 1st frequency variation of a diverging FGPEH ($\alpha = 0.6$, $N = 5$) under short- and open-circuit conditions.

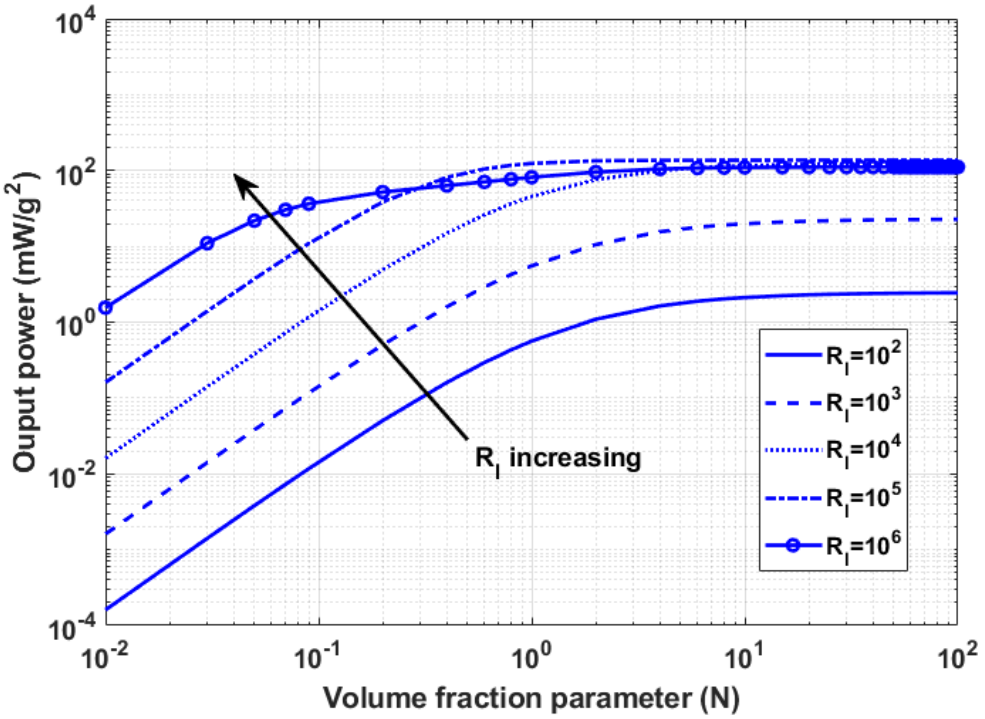

Figure 5.15 Output power variation of a converging FGPEH ($\alpha = -0.6$, $N = 5$) under different external load resistance.

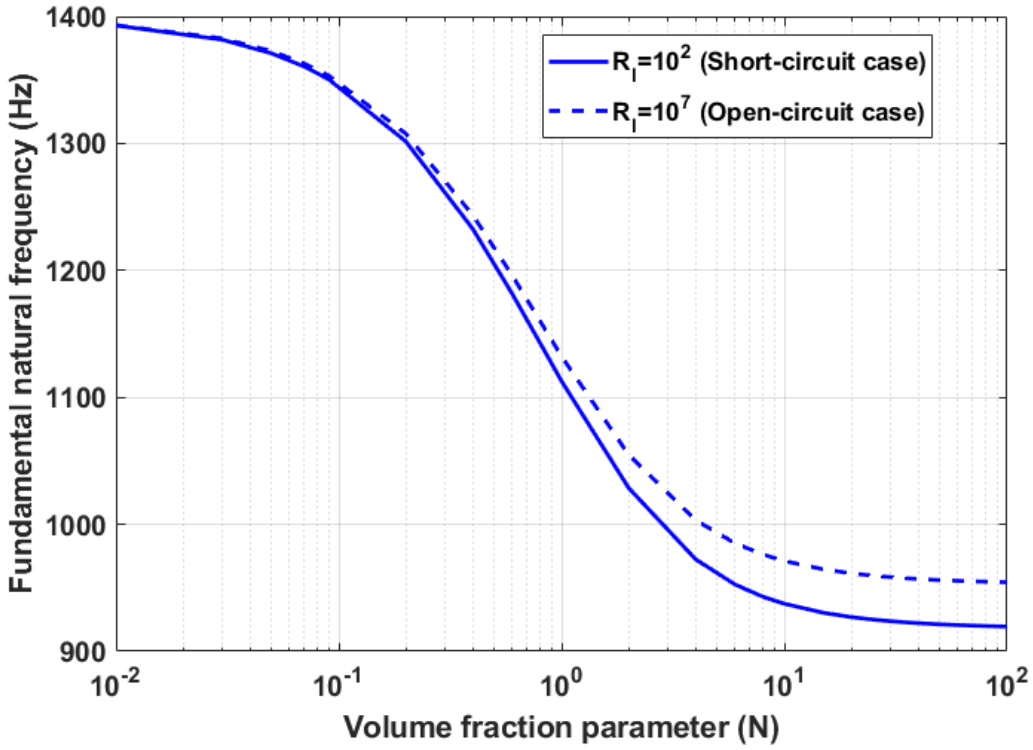

Figure 5.16 1st frequency variation of a converging FGPEH ($\alpha = -0.6$, $N = 5$) under short- and open-circuit conditions.

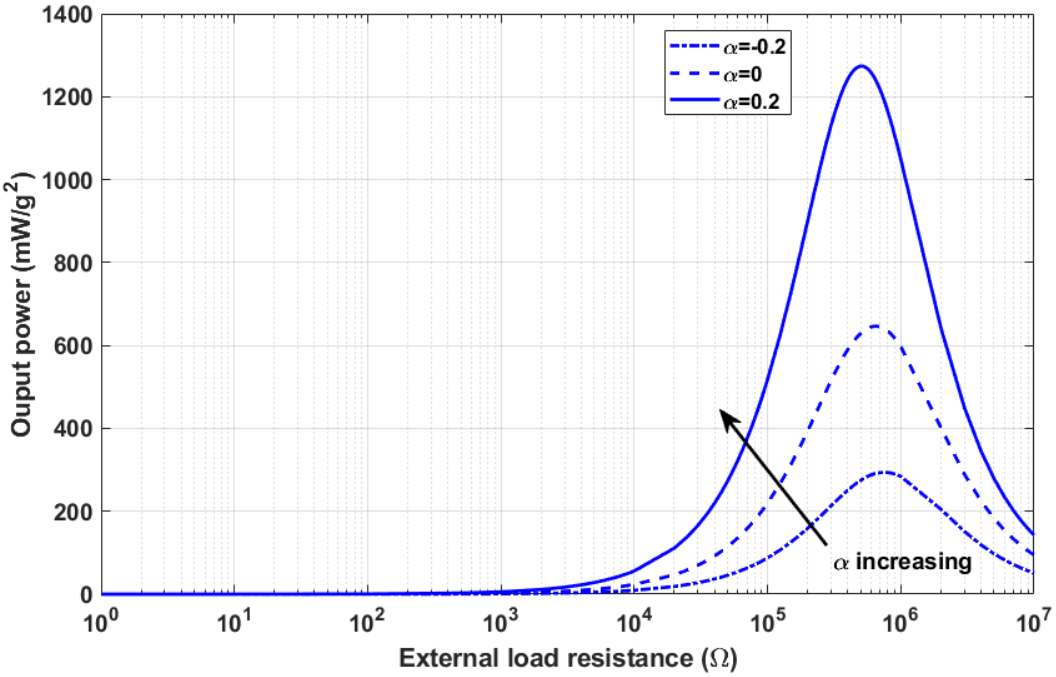

Figure 5.17 Output power variation of FGPEH ($n = 0.1$, $N = 5$) versus external load resistance under different tapering ratios.

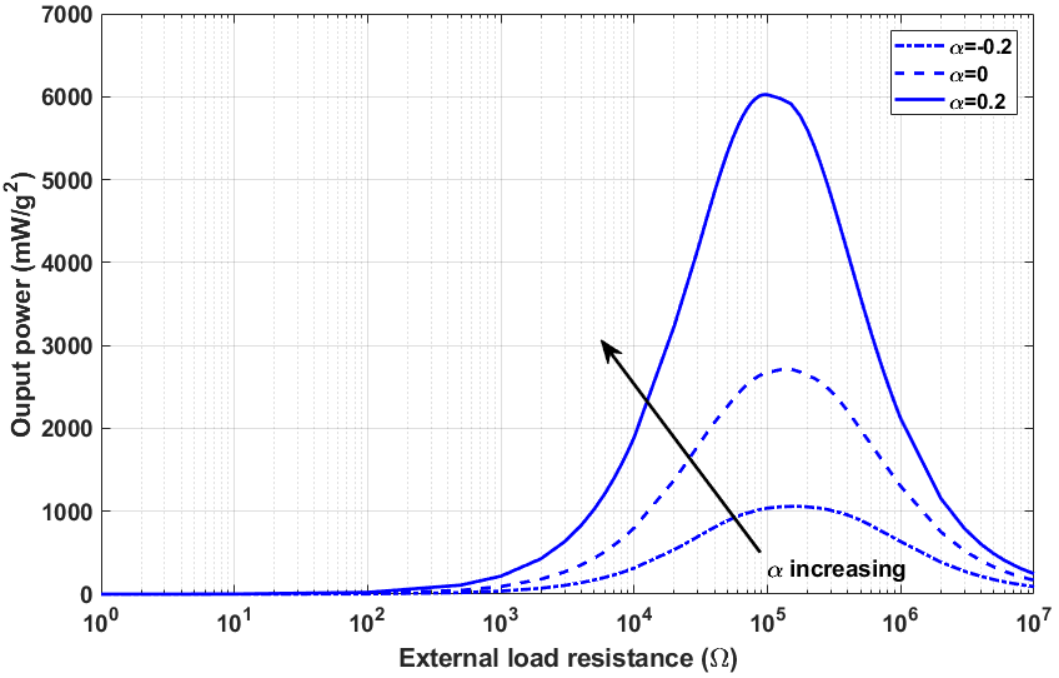

Figure 5.18 Output power variation of FGPEH ($n = 1, N = 5$) versus external load resistance under different tapering ratios.

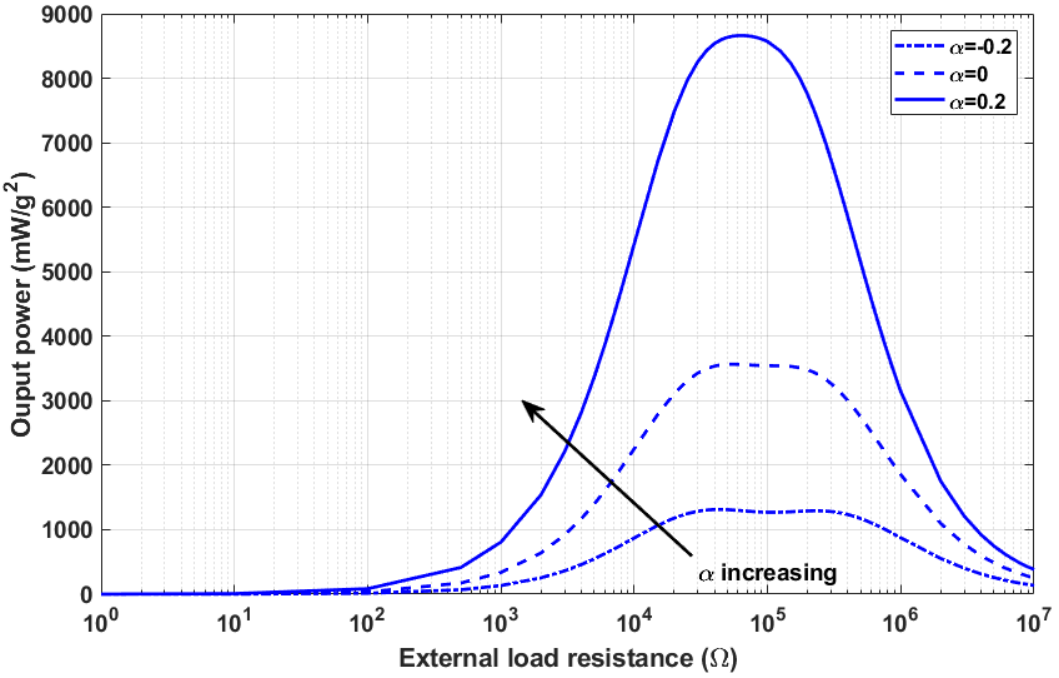

Figure 5.19 Output power variation of FGPEH ($n = 10, N = 5$) versus external load resistance under different tapering ratios.

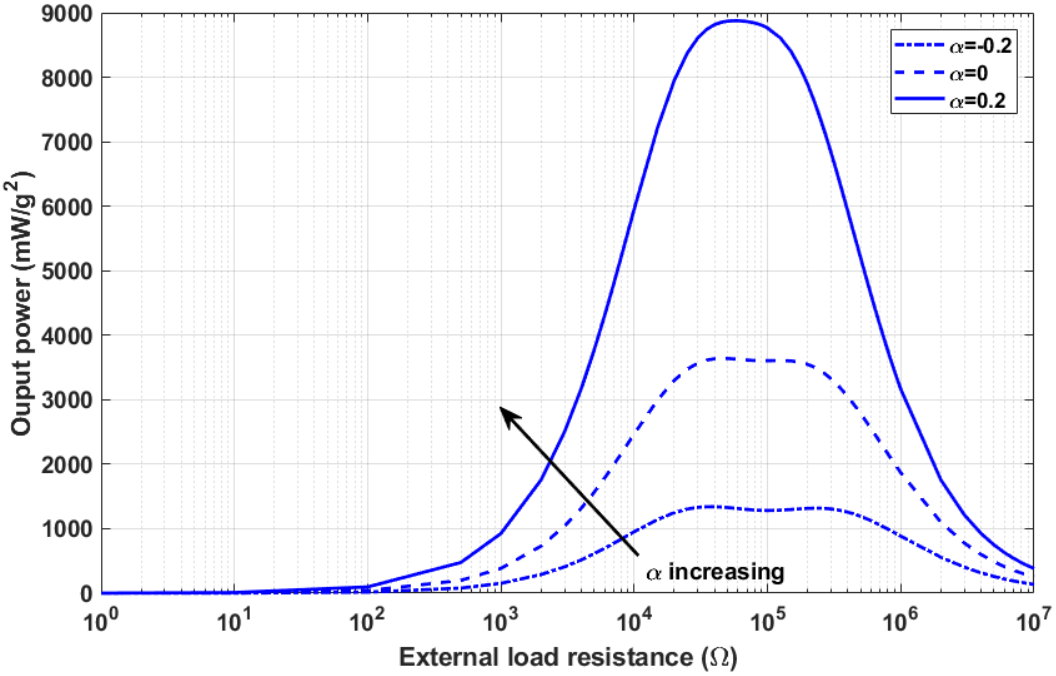

Figure 5.20 Output power variation of FGPEH ($n = 100, N = 5$) versus external load resistance under different tapering ratios.

5.6 Conclusions

In this chapter, the performance variation of non-uniform bimorph FGPEHs under different design parameters are analyzed. To numerically calculate the desired outputs a 4-DOF superconvergent element is employed. The presented element has the potential to examine both Euler-Bernoulli and Timoshenko beam theories. In fact, by changing one parameter of this element one can switch from the Timoshenko beam theory to the Euler-Bernoulli theory (Appendix A). It can provide the numerical results for different geometrical properties with a high degree of accuracy in good correlation to the experimental ones. To prove the accuracy of results, the numerical results are first validated for particular cases with other theoretical and experimental results from the open literature. In the following, the effects of different parameters including the degree of polynomial function, tapering ratio, external load resistance and volume fraction on the electrical outputs and fundamental natural frequency are examined. From the results, it is obvious that the degree of non-uniformity and the ratio of volume fraction of two constituent phases play an important role in the amount of scavenged energy and the first resonance frequency. The results show that the energy harvesting efficiency of FGPEHs can be easily controlled by adjusting the

non-uniformity and inhomogeneous parameters. Based on the investigations, the most important conclusions could be briefly listed as follows:

►The fundamental frequency increases with decreasing tapering ratio (application of converging beams) and this effect can be intensified by increasing the degree of polynomial function and vice versa for the diverging beams.

► Application of converging and diverging beams result in lower and higher electrical output power, respectively. Like the resonance frequency, the decreasing (increasing) influence can be amplified by the application of higher polynomial function degrees.

► Application of the diverging beams can result in not only increasing the electrical output, but also decreasing the fundamental resonance frequency which represents an advantageous geometry for scavenge energy from the ambient surroundings with low fundamental frequencies disturbance.

► For FGPEHs, the fundamental frequency decreases uniformly as the material volume fraction rises. Conversely, the volume fraction parameter has an increasing effect on the output power so that the maximum values belong to the pure piezoelectric constituent.

► For tapered FGPEH, the increasing load resistance has an enhancing effect on the output power and decreasing effect on the fundamental natural frequency for both converging and diverging beams.

► By increasing the volume fraction parameter the difference between the short-circuit and open-circuit frequencies increase to reach to the highest value for the pure piezoelectric condition ($n \to \infty$).

► The largest frequency difference between the short-circuit and open-circuit cases belongs to the converging beams.

► Raising the volume fraction parameter moves back the peak values of output power towards the lower external load resistances.

► Under a predetermined operating frequency, there is an optimal volume fraction parameter and tapering geometry providing the maximal output power.

Chapter 6 Summary, conclusions and future work

The conclusions of this research as well as the suggested future work are presented in this chapter. Firstly, the general conclusions are stated in the first section. The suggested future work is covered in the second section.

6.1 Summary

Paper-based smart systems are new and presented with their advantages along with their parametric studies. These systems are still in their early stages of development. The introdctory review of smart materials especially paper-based piezoelectric energy harvetsers is completely covered in the first chapeter. They possess exclusive merits in comparison to the conventional piezoelectric smart systems made entirely of PVDF or PZT. Unlike the conventioal piezoelectric materials they are lightweight, cost-effective, biodegradable, biocompatible, foldable, environmentally friendly, disposable, inexpensive to fabricate, portable and flexible. Additionally, compared to other flexible materials cellulose has a much lower coefficient of thermal expansion leading to the high thermal stability of final devices [17]. The only deficiency which needs to be surmounted is the lower performance. Based on the experimental research presented in the literature, the amount of extracted power from these smart materials are much lower than the regular piezoelectric energy harvesters. Hence, there is a need to study these structures to find out ways to improve the performance and efficiency enhancement. To satisfy the need, there are different venues which can be pursued including the enhancement of piezoelectric properties through functionalizing paper, geometry modification, and sizing. In this research, these solutions are separately considered and investigated. As there is no experimental work on paper based cantilever type piezoelectric energy harvesters, the validation of the proposed models made from PZT are available in the open literature. A first step in this investigation is the validation of the models and the concepts presented in the above work. This step has been completed and further investigations on paper based piezo cantilever like energy harvesters are now feasible.

In order to study the effects of different parameters, it is first necessary to formulate a theoretical model which can accurately predict the behavior of the system. Moreover, to solve the governing equations an efficient and accurate solution method is essential. Hence, the second chapter of this study is devoted to address these issues. In the second chapter, the structure of cantilever piezoelectric energy harvester is first modelled based on Euler-Bernoulli and Timoshenko beam theories. After that, finite element method with the application of a superconvergent element is applied to discretize the governing equations. The validation of the results using SCE shows a very good rate of convergence and excellent agreement between the

theoretical and experimental results reported in literature. The material presented in the chapter was published in the Journal of Intelligent Material Systems and Structures.

As the second step, in order to study the influence of the geometry modification, the behavior of cantilever piezoelectric energy harvesters under bending motion is modelled and investigated in the third chapter. Polynomial function with different degrees of non-uniformity introduced by changing their highest degree term from one to five is the kind of structure considered. The results indicate that improvement of the electrical output is feasible using polynomial function with higher degrees of non-uniformity. Efficiency is another important factor scrutinized in this chapter showing that its enhancement is achievable using the application of non-uniform geometries. The material presented in the chapter was published in the Journal of Intelligent Material Systems and Structures.

Sizing is one of the most important factors which needs to be considered for the performnce enhancement and weight reduction simultaneously. By sizing, it is possible to improve the desired output power without the application of extra piezoelectric material. This important issue is addressed in the third chapter. Here, a new system consisting of an array of tapered beams (diverging beams) was presented. In the new system although the same amount of piezoelectric material was used the harvested electrical power output and the weight of substrate layer increased and reduced, respectively. It is worth mentioning that the operation frequency was kept constant for the design of the new system. The material presented in this chapter was submitted to publication to the International Journal of Smart and Nano Materials

To complete the study, the effect of functionalizing is studied in the 5th chapter. In this chapter, the performance analysis of non-uniform bimorph functionally graded piezoelectric energy harvesters are analyzed. Study indicates that the degree of non-uniformity and the ratio of volume fraction play important roles in the 1st resonance frequency and subsequently the amount of scavenged energy. The material presented in this chapter was submitted to publication to the Journal of Intelligent Material Systems and Structures.

6.2 Conclusions

As it has been mentioned in the abstract, one of the main objective of this study is the performance enhancement piezoelectric energy harvesters which is met using the geometry modification, sizing

analysis and functionalizing the structure. Based on the investigations carried out in each chapter devoted to every recommended solution, the main conclusions could be briefly listed below:

- SCE is an element with a great range of convergence which only requires very few elements to capture the output resulting in the reduction of time and the cost of computation.
- It is more suitable to model the beam using the Timoshenko assumptions only for smaller values of slenderness ratio (less than 5).
- The degree of polynomial function has an increasing effect on the output voltage so that changing the degree from one to five results in enhancement of electrical voltage by 306%.
- Changing the geometry from a converging beam ($\alpha = -0.6$) to a diverging beam ($\alpha = 0.6$) leads to increasing the maximum output voltage by 2867.3%.
- Application of the diverging beams can both increase the electrical output and decrease the fundamental resonance frequency, respectively. This is an advantageous feature for scavenge energy from sources with low fundamental frequencies.
- The maximum output voltage is produced by the bimorph structure in parallel connection.
- By converging the beam and raising the power "n" from 1 to 5 the efficiency can be improved by 22%.
- The results indicate that the maximum efficiency is located between the open-circuit and short-circuit frequencies.
- By the application of a series of beams with optimized sizing the harvested electrical power output increased significantly by 140% although the same amount of piezoelectric material was used. Additionally, the weight of substrate layer is reduced by 15.64% by the application of thinner substrate layer.
- The fundamental frequency decreases uniformly as the material volume fraction rises while the output power rises such that the maximum values belong to the pure piezoelectric constituent.
- Increasing the volume fraction parameter widens the frequency gap difference between the short-circuit and open-circuit frequencies. In other words, the maximum amount of frequency difference occurred for the pure piezoelectric condition ($n \to \infty$).

● Rising the volume fraction parameter pushes the peak values of output power towards the lower external load resistances.

● For each excitation frequency there is always an optimal volume fraction parameter and tapering geometry leading to the maximal output power.

6.3 Particular contributions and future work

In this thesis, different gaps associated with the knowledge of piezoelectric energy harvesters were addressed in order to enhance the performance of PPEHs. In the following, the suggested future work regarding the improvement of the structures are listed.

1) Experimental validation of the achieved theoretical results for extended ranges of parameters.
2) Parameter optimization regarding the geometry and sizing of the structure.
3) Type and size of the selected electrodes are effective parameters which could change the amount of scavenged energy from the structure.
4) Owing to the nature of cantilever beams the volumetric strain is higher near the root of the beam (clamped end) while vibrating [96]. Thus, the non-uniformly distributed strain phenomenon along the length of the cantilever beam can yield an optimal value for the area of piezoelectric layer(s). Thus, optimization of piezoelelectrode coverage is another aspect that needs to be studied. In fact, performance anlysis of partially covered piezoelectric energy harvesters is of importance to maximize the scavenged output power.
5) It is worthwhile to carry out more investigations on the system comprising small piezoelectric patches placed at different locations of the substrate layer rather than wholly covered substrate layers.
6) Study of the fabrication of paper-based piezolectric energy harvesters is essential. Fiber cellulose impregnated with piezolectric materials can be tailored so as to fulfill specific needs such as requisite hydrophilicity, permeability, reactivity, functionality, piezoelectric properties etc. Based on the range of excitation frequencies there is the possibility to functionalize the paper-based smart structures such that it works with the maximum efficiency within the specified range. In other words, changing the percentage of component parts or the effective working conditions such as humidity are the influential parameters which can help one to achieve the goal.
7) Modeling and analysis of multilayer piezoelectric energy harvesters (stack of piezoelectric layers) is another effective strategy in the way of performance enhancenment. By

increasing the piezoelectric layers one may be able to enhance the efficiency and performance of structures.

8) Develop a mathematical/theoretical model –with emphasis on the physics- to accurately predict the results of paper-based mechanical energy harvesters as the one layer structure.

References

[1] Kim HS, Kim J-H, Kim J. "A review of piezoelectric energy harvesting based on vibration," *International journal of precision engineering and manufacturing*. 2011; 12(6), 1129-41.
[2] Bowen C, Kim H, Weaver P, Dunn S. "Piezoelectric and ferroelectric materials and structures for energy harvesting applications," *Energy & Environmental Science*. 2014; 7(1), 25-44.
[3] Erturk A, Inman DJ. Piezoelectric energy harvesting: John Wiley & Sons; 2011.
[4] Crawley EF, De Luis J. "Use of piezoelectric actuators as elements of intelligent structures," *AIAA journal*. 1987; 25(10), 1373-85.
[5] Roundy S, Wright PK, Rabaey J. "A study of low level vibrations as a power source for wireless sensor nodes," *Computer communications*. 2003; 26(11), 1131-44.
[6] Chalasani S, Conrad JM, editors. A survey of energy harvesting sources for embedded systems. Southeastcon, 2008 IEEE; 2008: IEEE.
[7] Sodano HA, Inman DJ, Park G. "A review of power harvesting from vibration using piezoelectric materials," *Shock and Vibration Digest*. 2004; 36(3), 197-206.
[8] Li H, Tian C, Deng ZD. "Energy harvesting from low frequency applications using piezoelectric materials," *Applied physics reviews*. 2014; 1(4), 041301.
[9] Kendall CJ. Parasitic power collection in shoe mounted devices: Citeseer; 1998.
[10] Dutoit NE, Wardle BL, Kim S-G. "Design considerations for MEMS-scale piezoelectric mechanical vibration energy harvesters," *Integrated ferroelectrics*. 2005; 71(1), 121-60.
[11] Beeby SP, Tudor MJ, White N. "Energy harvesting vibration sources for microsystems applications," *Measurement science and technology*. 2006; 17(12), R175.
[12] Thomson W. Theory of vibration with applications: CRC Press; 1996.
[13] Priya S, Song H-C, Zhou Y, Varghese R, Chopra A, Kim S-G, et al. "A review on piezoelectric energy harvesting: materials, methods, and circuits," *Energy Harvesting and Systems*. 2019; 4(1), 3-39.
[14] Sharma PK, Baredar PV. "Analysis on piezoelectric energy harvesting small scale device–a review," *Journal of King Saud University-Science*. 2019; 31(4), 869-77.
[15] Klemm D, Heublein B, Fink HP, Bohn A. "Cellulose: fascinating biopolymer and sustainable raw material," *Angewandte Chemie International Edition*. 2005; 44(22), 3358-93.
[16] Kim J, Lee H, Kim HS. "Beam vibration control using cellulose-based Electro-Active Paper sensor," *International Journal of Precision Engineering and Manufacturing*. 2010; 11(6), 823-7.
[17] Kim KH, Lee KY, Seo JS, Kumar B, Kim SW. "Paper-based piezoelectric nanogenerators with high thermal stability," *Small*. 2011; 7(18), 2577-80.
[18] Kumar S, Pandey CM, Hatamie A, Simchi A, Willander M, Malhotra BD. "Nanomaterial-Modified Conducting Paper: Fabrication, Properties, and Emerging Biomedical Applications," *Global Challenges*. 2019; 3(12), 1900041.

[19] Mishra S, Unnikrishnan L, Nayak SK, Mohanty S. "Advances in piezoelectric polymer composites for energy harvesting applications: A systematic review," *Macromolecular Materials and Engineering*. 2019; 304(1), 1800463.
[20] Mahadeva SK, Walus K, Stoeber B. "Paper as a platform for sensing applications and other devices: a review," *ACS applied materials & interfaces*. 2015; 7(16), 8345-62.
[21] Huang J, Zhu H, Chen Y, Preston C, Rohrbach K, Cumings J, et al. "Highly transparent and flexible nanopaper transistors," *Acs Nano*. 2013; 7(3), 2106-13.
[22] Abas Z, Kim HS, Zhai L, Kim J, Kim J-H. "Electrode effects of a cellulose-based electro-active paper energy harvester," *Smart Materials and Structures*. 2014; 23(7), 074003.
[23] Pushparaj VL, Shaijumon MM, Kumar A, Murugesan S, Ci L, Vajtai R, et al. "Flexible energy storage devices based on nanocomposite paper," *Proceedings of the National Academy of Sciences*. 2007; 104(34), 13574-7.
[24] Müller R, Clegg D. "Automatic paper chromatography," *Analytical Chemistry*. 1949; 21(9), 1123-5.
[25] Martinez AW, Phillips ST, Butte MJ, Whitesides GM. "Patterned paper as a platform for inexpensive, low-volume, portable bioassays," *Angewandte Chemie International Edition*. 2007; 46(8), 1318-20.
[26] Shiroma LY, Santhiago M, Gobbi AL, Kubota LT. "Separation and electrochemical detection of paracetamol and 4-aminophenol in a paper-based microfluidic device," *Analytica chimica acta*. 2012; 725, 44-50.
[27] Arena A, Donato N, Saitta G, Bonavita A, Rizzo G, Neri G. "Flexible ethanol sensors on glossy paper substrates operating at room temperature," *Sensors and Actuators B: Chemical*. 2010; 145(1), 488-94.
[28] Lin C-W, Zhao Z, Kim J, Huang J. "Pencil drawn strain gauges and chemiresistors on paper," *Scientific reports*. 2014; 4, 3812.
[29] Kim J, Yang SY, Yun G-Y, Jang S, Yun K, editors. Cellulose electro-active paper: actuator, sensor and beyond. Electroactive Polymer Actuators and Devices (EAPAD) 2009; 2009: International Society for Optics and Photonics.
[30] Lemaire E, Moser R, Borsa CJ, Shea H, Briand D. "Green Paper-based Piezoelectric Material for Sensors and Actuators," *Procedia Engineering*. 2015; 120, 360-3.
[31] Kim J, Seo YB. "Electro-active paper actuators," *Smart Materials and Structures*. 2002; 11(3), 355-60.
[32] Yun S, Kim J, Lee K-S. "Evaluation of cellulose electro-active paper made by tape casting and zone stretching methods," *International Journal of Precision Engineering and Manufacturing*. 2010; 11(6), 987-90.
[33] Toroń B, Szperlich P, Nowak M, Stróż D, Rzychoń T. "Novel piezoelectric paper based on SbSI nanowires," *Cellulose*. 2017; 25(1), 7-15.
[34] Ge L, Wang S, Yu J, Li N, Ge S, Yan M. "Molecularly Imprinted Polymer Grafted Porous Au-Paper Electrode for an Microfluidic Electro-Analytical Origami Device," *Advanced Functional Materials*. 2013; 23(24), 3115-23.

[35] Klasner SA, Price AK, Hoeman KW, Wilson RS, Bell KJ, Culbertson CT. "based microfluidic devices for analysis of clinically relevant analytes present in urine and saliva," *Analytical and bioanalytical chemistry*. 2010; 397(5), 1821-9.
[36] Kim J, Yun S, Ounaies Z. "Discovery of cellulose as a smart material," *Macromolecules*. 2006; 39(12), 4202-6.
[37] Shi K, Huang X, Sun B, Wu Z, He J, Jiang P. "Cellulose/BaTiO3 aerogel paper based flexible piezoelectric nanogenerators and the electric coupling with triboelectricity," *Nano Energy*. 2019; 57, 450-8.
[38] Shin D-M, Hong SW, Hwang Y-H. "Recent Advances in Organic Piezoelectric Biomaterials for Energy and Biomedical Applications," *Nanomaterials*. 2020; 10(1), 123.
[39] Fukada E. "Piezoelectricity as a fundamental property of wood," *Wood Science and Technology*. 1968; 2(4), 299-307.
[40] Sugiyama J, Chanzy H, Maret G. "Orientation of cellulose microcrystals by strong magnetic fields," *Macromolecules*. 1992; 25(16), 4232-4.
[41] Kimura F, Kimura T, Tamura M, Hirai A, Ikuno M, Horii F. "Magnetic alignment of the chiral nematic phase of a cellulose microfibril suspension," *Langmuir*. 2005; 21(5), 2034-7.
[42] Bordel D, Putaux J-L, Heux L. "Orientation of native cellulose in an electric field," *Langmuir*. 2006; 22(11), 4899-901.
[43] Kondo T, Togawa E, Brown RM. "“Nematic ordered cellulose”: a concept of glucan chain association," *Biomacromolecules*. 2001; 2(4), 1324-30.
[44] Ba Y, Bao J, Song R, Zhu C, Zhang X, editors. Printing Paper-Like Piezoelectric Energy Harvesters Based on Natural Cellulose Nanofibrils. 2019 20th International Conference on Solid-State Sensors, Actuators and Microsystems & Eurosensors XXXIII (TRANSDUCERS & EUROSENSORS XXXIII); 2019: IEEE.
[45] Roundy S, Wright PK. "A piezoelectric vibration based generator for wireless electronics," *Smart Materials and structures*. 2004; 13(5), 1131.
[46] Hagood NW, Chung WH, Von Flotow A. "Modelling of piezoelectric actuator dynamics for active structural control," *Journal of intelligent material systems and structures*. 1990; 1(3), 327-54.
[47] Sodano HA, Park G, Inman D. "Estimation of electric charge output for piezoelectric energy harvesting," *Strain*. 2004; 40(2), 49-58.
[48] DuToit NE, Wardle BL. "Experimental verification of models for microfabricated piezoelectric vibration energy harvesters," *AIAA journal*. 2007; 45(5), 1126-37.
[49] Erturk A, Inman DJ. "Issues in mathematical modeling of piezoelectric energy harvesters," *Smart Materials and Structures*. 2008; 17(6), 065016.
[50] Reddy JN. Mechanics of laminated composite plates and shells: theory and analysis: CRC press; 2004.
[51] Segerlind LJ. Applied Finite Element Analysis: Wiley; 1984.
[52] Reddy JN. Energy principles and variational methods in applied mechanics: John Wiley & Sons; 2017.

[53] Leo DJ. Engineering analysis of smart material systems: John Wiley & Sons; 2007.
[54] Wang G. "Analysis of bimorph piezoelectric beam energy harvesters using Timoshenko and Euler–Bernoulli beam theory," *Journal of Intelligent Material Systems and Structures*. 2013; 24(2), 226-39.
[55] Choi W, Jeon Y, Jeong J-H, Sood R, Kim S-G. "Energy harvesting MEMS device based on thin film piezoelectric cantilevers," *Journal of Electroceramics*. 2006; 17(2-4), 543-8.
[56] Cook-Chennault K, Thambi N, Sastry A. "Powering MEMS portable devices—a review of non-regenerative and regenerative power supply systems with special emphasis on piezoelectric energy harvesting systems," *Smart Materials and Structures*. 2008; 17(4), 043001.
[57] DeVoe DL, Pisano AP. "Modeling and optimal design of piezoelectric cantilever microactuators," *Journal of Microelectromechanical systems*. 1997; 6(3), 266-70.
[58] Badel A, Guyomar D, Lefeuvre E, Richard C. "Efficiency enhancement of a piezoelectric energy harvesting device in pulsed operation by synchronous charge inversion," *Journal of Intelligent Material Systems and Structures*. 2005; 16(10), 889-901.
[59] Ottman GK, Hofmann HF, Bhatt AC, Lesieutre GA. "Adaptive piezoelectric energy harvesting circuit for wireless remote power supply," *IEEE Transactions on power electronics*. 2002; 17(5), 669-76.
[60] Erturk A, Inman DJ. "A distributed parameter electromechanical model for cantilevered piezoelectric energy harvesters," *Journal of vibration and acoustics*. 2008; 130(4), 041002.
[61] Erturk A, Inman DJ. "On mechanical modeling of cantilevered piezoelectric vibration energy harvesters," *Journal of Intelligent Material Systems and Structures*. 2008; 19(11), 1311-25.
[62] Erturk A, Inman DJ. "An experimentally validated bimorph cantilever model for piezoelectric energy harvesting from base excitations," *Smart materials and structures*. 2009; 18(2), 025009.
[63] Fakhzan M, Muthalif AG. "Harvesting vibration energy using piezoelectric material: Modeling, simulation and experimental verifications," *Mechatronics*. 2013; 23(1), 61-6.
[64] Dietl J, Wickenheiser A, Garcia E. "A Timoshenko beam model for cantilevered piezoelectric energy harvesters," *Smart Materials and Structures*. 2010; 19(5), 055018.
[65] Meirovitch L. Fundamentals of vibrations: Waveland Press; 2010.
[66] Ajitsaria J, Choe S-Y, Shen D, Kim D. "Modeling and analysis of a bimorph piezoelectric cantilever beam for voltage generation," *Smart Materials and Structures*. 2007; 16(2), 447.
[67] Roundy S, Leland ES, Baker J, Carleton E, Reilly E, Lai E, et al. "Improving power output for vibration-based energy scavengers," *IEEE Pervasive computing*. 2005; 4(1), 28-36.
[68] Baker J, Roundy S, Wright P, editors. Alternative geometries for increasing power density in vibration energy scavenging for wireless sensor networks. 3rd international energy conversion engineering conference; 2005.
[69] Goldschmidtboeing F, Woias P. "Characterization of different beam shapes for piezoelectric energy harvesting," *Journal of micromechanics and microengineering*. 2008; 18(10), 104013.

[70] Benasciutti D, Moro L, Zelenika S, Brusa E. "Vibration energy scavenging via piezoelectric bimorphs of optimized shapes," *Microsystem technologies*. 2010; 16(5), 657-68.
[71] Rosa M, De Marqui Junior C. "Modeling and analysis of a piezoelectric energy harvester with varying cross-sectional area," *Shock and Vibration*. 2014; 2014.
[72] Salmani H, Rahimi G, Hosseini Kordkheili S. "An exact analytical solution to exponentially tapered piezoelectric energy harvester," *Shock and Vibration*. 2015; 2015.
[73] Siddiqui NA, Kim D-J, Overfelt RA, Prorok BC. "Electromechanical coupling effects in tapered piezoelectric bimorphs for vibration energy harvesting," *Microsystem Technologies*. 2017; 23(5), 1537-51.
[74] Paquin S, St-Amant Y. "Improving the performance of a piezoelectric energy harvester using a variable thickness beam," *Smart Materials and Structures*. 2010; 19(10), 105020.
[75] Xie X, Carpinteri A, Wang Q. "A theoretical model for a piezoelectric energy harvester with a tapered shape," *Engineering Structures*. 2017; 144, 19-25.
[76] Sahoo DK, Pandey AK. "Performance of non-uniform cantilever based piezoelectric energy harvester," *ISSS Journal of Micro and Smart Systems*. 2018; 7(1), 1-13.
[77] Defosseux M, Allain M, Basrour S. "Comparison of different beam shapes for piezoelectric vibration energy harvesting," *Proceedings of PowerMEMS*. 2010, 339-42.
[78] Park J, Lee S, Kwak BM. "Design optimization of piezoelectric energy harvester subject to tip excitation," *Journal of Mechanical Science and Technology*. 2012; 26(1), 137-43.
[79] Matova S, Renaud M, Jambunathan M, Goedbloed M, Van Schaijk R. "Effect of length/width ratio of tapered beams on the performance of piezoelectric energy harvesters," *Smart Materials and Structures*. 2013; 22(7), 075015.
[80] Gallina M, Benasciutti D, editors. Finite element analysis of optimized piezoelectric bimorphs for vibrational 'energy harvesting'. Proceedings of the International CAE Conference; 2013.
[81] Dietl JM, Garcia E. "Beam shape optimization for power harvesting," *Journal of Intelligent Material Systems and Structures*. 2010; 21(6), 633-46.
[82] Yokoyama T. "Free vibration characteristics of rotating Timoshenko beams," *International Journal of Mechanical Sciences*. 1988; 30(10), 743-55.
[83] Hajheidaria P, Ghayour M, Mirdamadi HR. "Flap-Lag Vibration Analysis of Rotating Tapered Solid Beams with Functionally Graded Characteristics," *Journal of Aerospace Engineering*. 2015; 29(1), 04015018.
[84] IEEE. IEEE Standard on Piezoelectricity. 1987.
[85] Reddy JN. An introduction to the finite element method: McGraw-hill New York; 1993.
[86] Shafer MW, Garcia E. "The power and efficiency limits of piezoelectric energy harvesting," *Journal of Vibration and Acoustics*. 2014; 136(2), 021007.
[87] Kim M, Dugundji J, Wardle BL. "Efficiency of piezoelectric mechanical vibration energy harvesting," *Smart Materials and Structures*. 2015; 24(5), 055006.

[88] Kim M, Hoegen M, Dugundji J, Wardle BL. "Modeling and experimental verification of proof mass effects on vibration energy harvester performance," *Smart Materials and Structures*. 2010; 19(4), 045023.
[89] Wei C, Jing X. "A comprehensive review on vibration energy harvesting: Modelling and realization," *Renewable and Sustainable Energy Reviews*. 2017; 74, 1-18.
[90] Shu Y-C, Lien I. "Efficiency of energy conversion for a piezoelectric power harvesting system," *Journal of micromechanics and microengineering*. 2006; 16(11), 2429.
[91] Jia Y, Seshia AA. "Power optimization by mass tuning for MEMS piezoelectric cantilever vibration energy harvesting," *Journal of Microelectromechanical Systems*. 2015; 25(1), 108-17.
[92] Stewart M, Weaver PM, Cain M. "Charge redistribution in piezoelectric energy harvesters," *Applied Physics Letters*. 2012; 100(7), 073901.
[93] Guizzetti M, Ferrari V, Marioli D, Zawada T, editors. Thickness optimization of a piezoelectric converter for energy harvesting. Proceedings of the COMSOL Conference; 2009.
[94] Palosaari J, Leinonen M, Juuti J, Jantunen H. "The effects of substrate layer thickness on piezoelectric vibration energy harvesting with a bimorph type cantilever," *Mechanical Systems and Signal Processing*. 2018; 106, 114-8.
[95] Du S, Jia Y, Chen S-T, Zhao C, Sun B, Arroyo E, et al. "A new electrode design method in piezoelectric vibration energy harvesters to maximize output power," *Sensors and Actuators A: Physical*. 2017; 263, 693-701.
[96] Du S, Jia Y, Seshia A, editors. Maximizing output power in a cantilevered piezoelectric vibration energy harvester by electrode design. Journal of Physics: Conference Series; 2015: IOP Publishing.
[97] Hajheidari P, Stiharu I, Bhatt R. Power output enhancement of piezoelectric energy harvesters using electrode coverage optimization. ICAST2019: 30th International Conference on Adaptive Structures and Technologies; 7-11 October; Montreal, QC, Canada2019. p. 165-6.
[98] Lin H, Wu P, Lien I, Shu Y. "Analysis of an array of piezoelectric energy harvesters connected in series," *Smart Materials and Structures*. 2013; 22(9), 094026.
[99] Soliman M, Abdel-Rahman E, El-Saadany E, Mansour R. "A wideband vibration-based energy harvester," *Journal of Micromechanics and Microengineering*. 2008; 18(11), 115021.
[100] Liu J-Q, Fang H-B, Xu Z-Y, Mao X-H, Shen X-C, Chen D, et al. "A MEMS-based piezoelectric power generator array for vibration energy harvesting," *Microelectronics Journal*. 2008; 39(5), 802-6.
[101] Nisanth A, Suja K, Seena V, editors. Design and Simulation of MEMS AlN Piezoelectric Vibration Energy Harvester Array for Improved Power Density. 2018 IEEE SENSORS; 2018: IEEE.
[102] Andosca R, McDonald TG, Genova V, Rosenberg S, Keating J, Benedixen C, et al. "Experimental and theoretical studies on MEMS piezoelectric vibrational energy harvesters with mass loading," *Sensors and Actuators A: Physical*. 2012; 178, 76-87.
[103] Kim JE, Kim YY. "Analysis of piezoelectric energy harvesters of a moderate aspect ratio with a distributed tip mass," *Journal of Vibration and Acoustics*. 2011; 133(4), 041010.

[104] Glynne-Jones P, Beeby SP, White NM. "Towards a piezoelectric vibration-powered microgenerator," *IEE Proceedings-Science, measurement and technology*. 2001; 148(2), 68-72.
[105] Mehraeen S, Jagannathan S, Corzine KA. "Energy harvesting from vibration with alternate scavenging circuitry and tapered cantilever beam," *IEEE Transactions on Industrial Electronics*. 2009; 57(3), 820-30.
[106] Liu H, Quan C, Tay CJ, Kobayashi T, Lee C. "A MEMS-based piezoelectric cantilever patterned with PZT thin film array for harvesting energy from low frequency vibrations," *Physics Procedia*. 2011; 19, 129-33.
[107] Ahmed SM, Eladawy MI, Salem MS, Ragai H, editors. Controlling the Frequency Response of a Cantilever-Based Energy Harvesters Using Split Piezoelectric Elements. 2018 International Japan-Africa Conference on Electronics, Communications and Computations (JAC-ECC); 2018: IEEE.
[108] Xiao Z, Yang Tq, Dong Y, Wang Xc. "Energy harvester array using piezoelectric circular diaphragm for broadband vibration," *Applied Physics Letters*. 2014; 104(22), 223904.
[109] Zhao X, Shang Z, Luo G, Deng L. "A vibration energy harvester using AlN piezoelectric cantilever array," *Microelectronic Engineering*. 2015; 142, 47-51.
[110] Kim JH, Ko HU. Zinc oxide-cellulose nanocomposite and preparation method thereof. Google Patents; 2017.
[111] Elvin NG, Elvin AA, Spector M. "A self-powered mechanical strain energy sensor," *Smart Materials and structures*. 2001; 10(2), 293.
[112] Suresh S, Mortensen A. Fundamentals of Functionally Graded Materials: Processing and Thermomechanical Behaviour of Graded Metals and Metal-ceramic Composites: IOM Communications Limited; 1998.
[113] Derayatifar M, Tahani M, Moeenfard H. "Nonlinear analysis of functionally graded piezoelectric energy harvesters," *Composite Structures*. 2017; 182, 199-208.
[114] Amini Y, Emdad H, Farid M. "Finite element modeling of functionally graded piezoelectric harvesters," *Composite Structures*. 2015; 129, 165-76.
[115] Amini Y, Fatehi P, Heshmati M, Parandvar H. "Time domain and frequency domain analysis of functionally graded piezoelectric harvesters subjected to random vibration: Finite element modeling," *Composite Structures*. 2016; 136, 384-93.
[116] Keshmiri A, Wu N, Wang Q. "A new nonlinearly tapered FGM piezoelectric energy harvester," *Engineering Structures*. 2018; 173, 52-60.
[117] Huang H, Zhu ZHH, Su S. "Optimized energy harvesting through piezoelectric functionally graded cantilever beams," *Smart Materials and Structures*. 2018.
[118] Timoshenko S, Young DH. Element of Strength of Materials: 5th Ed: Van Nostrand Reinhold; 1962.
[119] Matsumoto T, Tatsumi D, Tamai N, Takaki T. "Solution properties of celluloses from different biological origins in LiCl· DMAc," *Cellulose*. 2001; 8(4), 275-82.

[120] El Seoud OA, Marson GA, Ciacco GT, Frollini E. "An efficient, one-pot acylation of cellulose under homogeneous reaction conditions," *Macromolecular Chemistry and Physics*. 2000; 201(8), 882-9.
[121] Yun S, Chen Y, Nayak JN, Kim J. "Effect of solvent mixture on properties and performance of electro-active paper made with regenerated cellulose," *Sensors and Actuators B: Chemical*. 2008; 129(2), 652-8.

Appendix A. Position of the neutral axis

Consider the rectangular cross section of a beam as shown in Fig. A1. (a). The width of the substrate and the piezoelectric layers are denoted by b_s and b_p, respectively. Moreover, h_s and h_p show their uniform thickness across the cross section. The procedure of finding the position of the neutral axis of the composite structures consisting different types of material is described in the elementary strength of material texts [118]. Based on the procedure, transforming the cross section of the beam to a homogenous cross section with only one single Young's modulus (E) is required. In this regard, firstly the Young's moduli ratio n is defined and determined. In the transformed cross section, the width of the material with the lower Young's modulus is widened (nb_s) if the ratio is larger than one and narrowed if the ratio is smaller than one. Since in the case study considered the modulus of elasticity of the substrate is always larger than that of the piezoelectric one ($E_s > E_p$), widening state is occurring. Fig. A1 (b) represents the transformed cross section of the unimorph beam. Taking into account the Young's moduli, the position of the neutral axis can be defined using the following equation.

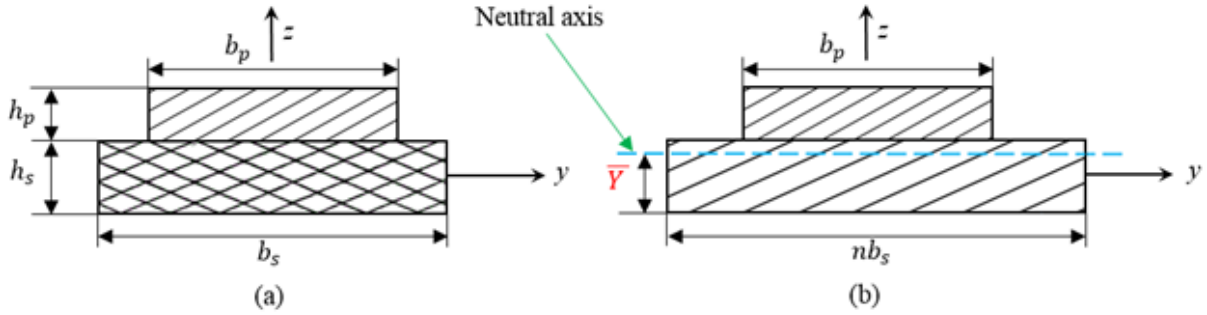

Figure A1 (a) Cross section of the unimorph beam (b) the transformed cross section.

$$\overline{Y} = \frac{\sum_{i=1}^{2} \overline{Y}_i A_i}{\sum_{i=1}^{2} A_i} = \frac{b_p h_p \left(h_s + \frac{h_p}{2}\right) + \frac{n h_s{}^2 b_s}{2}}{b_p h_p + n b_s h_s} \tag{A1}$$

Appendix B. Detailed calculations of total kinetic and potential energies

The total potential and kinetic energy expressions are given by

$$\begin{aligned} U = \frac{1}{2}\int \left[E_s\left(\acute{u}_0 + z\acute{\phi}_x\right)^2 + K_s G_s(\phi_x + \acute{w}_0)^2\right] dV_s \\ + \frac{1}{2}\int \left[E_p\left(\acute{u}_0 + z\acute{\phi}_x\right)^2 - d_{31}E_p E_{31}\left(\acute{u}_0 + z\acute{\phi}_x\right)\right. \\ \left. + K_s G_p(\phi_x + \acute{w}_0)^2\right] dV_p \end{aligned} \tag{B1}$$

$$\begin{aligned} T = \frac{1}{2}\int \rho[\dot{u}^2 + \dot{w}^2]dV \\ = \frac{1}{2}\int \rho_s\left[\left(\dot{u}_0 + z\dot{\phi}_x\right)^2 + (\dot{w}_0 + \dot{g})^2\right] dV_s \\ + \frac{1}{2}\int \rho_p\left[\left(\dot{u}_0 + z\dot{\phi}_x\right)^2 + (\dot{w}_0 + \dot{g})^2\right] dV_p \end{aligned} \tag{B2}$$

After more simplifying

$$\begin{aligned} U = \frac{1}{2}\int \left[E_s\left(\acute{u}_0{}^2 + z^2\acute{\phi}_x{}^2 + 2z\acute{u}_0\acute{\phi}_x\right) + K_s G_s\left(\phi_x{}^2 + \acute{w}_0{}^2 + 2\phi_x\acute{w}_0\right)\right] dV_s \\ + \frac{1}{2}\int \left[E_p\left(\acute{u}_0{}^2 + z^2\acute{\phi}_x{}^2 + 2z\acute{u}_0\acute{\phi}_x\right) - d_{31}E_p\left(-\frac{v(t)}{h_p}\right)\left(\acute{u}_0 + z\acute{\phi}_x\right)\right. \\ \left. + K_s G_p\left(\phi_x{}^2 + \acute{w}_0{}^2 + 2\phi_x\acute{w}_0\right)\right] dV_p \end{aligned} \tag{B3}$$

$$\begin{aligned} T = \frac{1}{2}\int \rho[\dot{u}^2 + \dot{w}^2]dV \\ = \frac{1}{2}\int \left[\left(\dot{u}_0{}^2 + z^2\dot{\phi}_x{}^2 + 2z\dot{u}_0\dot{\phi}_x\right) + \left(\dot{w}_0{}^2 + \dot{g}^2 + 2\dot{g}\dot{w}_0\right)\right] dV_s \\ + \frac{1}{2}\int \left[\left(\dot{u}_0{}^2 + z^2\dot{\phi}_x{}^2 + 2z\dot{u}_0\dot{\phi}_x\right) + \left(\dot{w}_0{}^2 + \dot{g}^2 + 2\dot{g}\dot{w}_0\right)\right] dV_p \end{aligned} \tag{B4}$$

Appendix C. Shape functions of the four-DOF (superconvergent element)

The three shape functions for this type of element are as follows:

C1. Lagrange linear shape functions

$$\chi_1^e = (1-\eta) \tag{C1}$$

$$\chi_2^e = \eta \tag{C2}$$

C2. Cubic shape functions

$$\psi_1^e = \frac{1}{1+\beta}[1+\beta(1-\eta)-(3-2\eta)\eta^2] \tag{C3}$$

$$\psi_2^e = \frac{-l_e}{1+\beta}\left[(1-\eta)^2\eta+\frac{\beta}{2}(1-\eta)\eta\right] \tag{C4}$$

$$\psi_3^e = \frac{1}{1+\beta}[(3-2\eta)\eta^2+\beta\eta] \tag{C5}$$

$$\psi_4^e = \frac{l_e}{1+\beta}\left[(1-\eta)\eta^2+\frac{\beta}{2}(1-\eta)\eta\right] \tag{C6}$$

C3. Quadratic shape functions

$$\varphi_1^e = \frac{6}{l_e(1+\beta)}(1-\eta)\eta \tag{C7}$$

$$\varphi_2^e = \frac{1}{1+\beta}[1+\beta-(4+\beta)\eta+3\eta^2] \tag{C8}$$

$$\varphi_3^e = \frac{-6}{l_e(1+\beta)}(1-\eta)\eta \tag{C9}$$

$$\varphi_4^e = \frac{1}{1+\beta}[(\beta-2)\eta+3\eta^2] \tag{C10}$$

where

$$\eta \triangleq \frac{x}{l_e} \tag{C11}$$

$$\beta \triangleq \frac{12(I_2^E + J_2^E)}{{l_e}^2(I_0^G + J_0^G)} \tag{B12}$$

where l_e is the length of a typical element of the beam. In the previous shape functions, if $\beta = 0$ (or in other words $J_0^G \to \infty$ and $I_0^G \to \infty$, i.e., the assumption of no-shear-deformation theory), shape functions corresponding to the Euler–Bernoulli beam are obtained and the interpolating functions are reduced to cubic and quadratic Hermitian polynomials.

Appendix D. Shape functions of eight-DOF

$$f_1 = 1 - 3\eta^2 + 2\eta^3 \tag{D1}$$

$$f_2 = \eta - 2\eta^2 + \eta^3 \tag{D2}$$

$$f_3 = 3\eta^2 - 2\eta^3 \tag{D3}$$

$$f_4 = -\eta^2 + \eta^3 \tag{D4}$$

Appendix E. Matrices of the piezoelectric beam in flapping mode

E1. Unimorph structure

$$\boldsymbol{M^e} = \int_0^{l_e} \left(I_0^\rho + J_0^\rho\right) {N_u}^T N_u dx + \int_0^{l_e} \left(I_0^\rho + J_0^\rho\right) {N_w}^T N_w dx + \int_0^{l_e} \left(I_2^\rho + J_2^\rho\right) {N_\phi}^T N_\phi dx$$
$$+ \int_0^{l_e} J_1^\rho {N_\phi}^T N_u dx + \int_0^{l_e} J_1^\rho {N_u}^T N_\phi dx \tag{E1}$$

$$\boldsymbol{K^e} = \int_0^{l_e} (I_0^E + J_0^E) {\acute{N}_u}^T \acute{N}_u dx + \int_0^{l_e} (I_2^E + J_2^E) {\acute{N}_\phi}^T \acute{N}_\phi dx + \int_0^{l_e} J_1^E {\acute{N}_\phi}^T \acute{N}_u dx$$
$$+ \int_0^{l_e} J_1^E {\acute{N}_u}^T \acute{N}_\phi dx + \int_0^{l_e} (I_0^G + J_0^G) {\acute{N}_w}^T \acute{N}_w dx + \int_0^{l_e} (I_0^G + J_0^G) {N_\phi}^T N_\phi dx \tag{E2}$$
$$+ \int_0^{l_e} (I_0^G + J_0^G) {N_\phi}^T \acute{N}_w dx + \int_0^{l_e} (I_0^G + J_0^G) {\acute{N}_w}^T N_\phi dx$$

$$\boldsymbol{f^e} = -\int_0^{l_e} \left(I_0^\rho + J_0^\rho\right) {N_w}^T \ddot{g} dx \tag{E3}$$

$$\boldsymbol{\theta^e} = -\int_0^{l_e} \frac{d_{31}}{h_p} J_1^E {\acute{N}_\phi}^T dx \quad and \quad \overline{C}_p = C_p \tag{E4}$$

E2. Bimorph structure in series state

$$\boldsymbol{M^e} = \int_0^{l_e} \left(I_0^\rho + 2J_0^\rho\right) {N_w}^T N_w dx + \int_0^{l_e} \left(I_2^\rho + 2J_2^\rho\right) {N_\phi}^T N_\phi dx \tag{E5}$$

$$\boldsymbol{K^e} = \int_0^{l_e} (I_2^E + 2J_2^E)\acute{N}_\phi{}^T \acute{N}_\phi dx + \int_0^{l_e} (I_0^G + 2J_0^G)\acute{N}_w{}^T \acute{N}_w dx + \int_0^{l_e} (I_0^G + 2J_0^G) N_\phi{}^T N_\phi dx + \int_0^{l_e} (I_0^G + 2J_0^G) N_\phi{}^T \acute{N}_w dx + \int_0^{l_e} (I_0^G + 2J_0^G)\acute{N}_w{}^T N_\phi dx \tag{E6}$$

$$\boldsymbol{f^e} = -\int_0^{l_e} \left(I_0^\rho + 2J_0^\rho\right) N_w{}^T \ddot{g} dx \tag{E7}$$

$$\boldsymbol{\theta^e} = -\int_0^{l_e} \frac{d_{31}}{h_p} J_1^E \acute{N}_\phi{}^T dx \quad and \quad \overline{C}_p = \frac{C_p}{2} \tag{E8}$$

E3. Bimorph structure in parallel state

$$\boldsymbol{M^e} = \int_0^{l_e} \left(I_0^\rho + 2J_0^\rho\right) N_w{}^T N_w dx + \int_0^{l_e} \left(I_2^\rho + 2J_2^\rho\right) N_\phi{}^T N_\phi dx \tag{E9}$$

$$\boldsymbol{K^e} = \int_0^{l_e} (I_2^E + 2J_2^E)\acute{N}_\phi{}^T \acute{N}_\phi dx + \int_0^{l_e} (I_0^G + 2J_0^G)\acute{N}_w{}^T \acute{N}_w dx + \int_0^{l_e} (I_0^G + 2J_0^G) N_\phi{}^T N_\phi dx + \int_0^{l_e} (I_0^G + 2J_0^G) N_\phi{}^T \acute{N}_w dx + \int_0^{l_e} (I_0^G + 2J_0^G)\acute{N}_w{}^T N_\phi dx \tag{E10}$$

$$\boldsymbol{f^e} = -\int_0^{l_e} \left(I_0^\rho + 2J_0^\rho\right) N_w{}^T \ddot{g} dx \tag{E11}$$

$$\boldsymbol{\theta^e} = -2\int_0^{l_e} \frac{d_{31}}{h_p} J_1^E \acute{N}_\phi{}^T dx \quad and \quad \overline{C}_p = 2C_p \tag{E12}$$

Appendix F. Fabrication process of paper-based piezoelectric materials

The material preparation of piezoelectric papers has been investigated in different studies. To prepare the structure different ingredients and procedures have been taken into consideration. The fabrication process differs based on the applied ingredients. Here, one of the common methods is considered and described in detail. The procedure comprises of a number of steps brought in the following. The main ingredients consist of cotton pulp, lithium chrloride (LiCl) and anhydrous DMAc (N,N -dimethyl acetamide) with different fractions. As the first step, the cotton pulp (MVE, DPw 4580) with the degree of polymerization, 4500 is torn in small pieces. As the next step one treatment named the pretreatment process should be performed to guarantee the dissolution of the cellulose samples in the solvent. As the pretreatment operation, the cellulose samples are conditioned by being immersed in a solution including water (1×), acetone (2×) and DMAc (2×) at room temperature [119]. After pretreatment, in order to remove the remnant water inside, the cotton pulp and lithium chloride (LiCl/Junsei Chemical) are heated in oven at the conditions 100℃ and low pressure for 30 minutes. After that, the smallest pieces of the cotton pulp are dissolved with LiCl/anhydrous DMAc (N,N -dimethyl acetamide) in proportion of cotton cellulose pulp/LiCl/DMAc to 2/8/90. The cellulose is dissolved in the solvent by heating at 155℃ with mechanical stirring according to the solvent exchange technique [120]. To reach a homogeneous solution, the mixture was stirred using magnetic bar stirrer as solvent exchange process until LiCl and the raw cotton pulp completely dissolved. The cellulose solution are spin coated on a silicon wafer or a piece of glass by a spin coater. The layer is approximately 20 μm in thickness. Then, it is treated in solvent mixture with a 50:50 (v/v) mixture of deionized (DI) water and Isopropyl alcohol (IPA), for 10 minutes to effectively eliminate Li+ ions as well as DMAc [121]. The cured film was rinsed in DI water. To align cellulose chains with uniaxial direction, the film is drawn at wet state by designed stretching system with different drawing ratio. The film is dried by exposing the film to infrared ray for approximately one hour. For the stretching process, different stretching ratios (SRs) are taken from including 1, 1.5, 1.6, 1.8, and 2. The stretching ratio is defined as the ratio between the original length of the cellulose before the stretching and the length of the stretched cellulose. To be able to measure the output voltage, the EAPap is fabricated by coating gold electrode on both sides of the cellulose film by a thermal evaporator. Typically, the thickness of the cellulose EAPap ranges from 15 μm to 30 μm. Finally, the poling procedure should be

applied to the structure to improve the piezoelectric properties. In fact, after the completion of fabrication process the orientation of the individual electric dipoles in a piezoelectric material is disordered which needs to be aligned for the material to exhibit strong electromechanical coupling. As the poling process the piezoelectric material is heated up above its Curie temperature and then placed in a strong electric field [53]. In order to remove the effects of moisture on the properties the EAPap sample can be coated by a thin laminating film on the top and bottom surfaces for packaging. Another potential option is the use of a piezoelectric nanomaterial such as ZnO which, after dispersion in a liquid phase and sonicated, it would be imbibed in the paper matrix. The nanoparticles will orient as dipoles [please add the reference sent along with the thesis] when the paper and nanoparticles are places in an electrostatic field. Stacks of such layers may improve the efficiency of the piezoelectric energy harvesters.